Novel Applications and Improvements to the Diffuse Correlation Spectroscopy Technique

Philip Binner

Submitted in fulfilment of the requirements for the
Degree of Doctor of Philosophy

School of Physics and Astronomy
College of Science and Engineering
University of Glasgow

Abstract

Diffuse correlation spectroscopy (DCS) is an optical technique that measures the temporal autocorrelation of scattered light. It is a well-known technique in the biomedical imaging community and is currently popular for live brain activation measurements based on blood flow rate. Although famous for blood flow measurements, its measurement parameter, the speckle decorrelation time, has been shown to linearly correlate with tissue stiffness. In this thesis, I apply DCS to two biomedical applications, from the remote sensing of neurodegeneration to cancerous tumour imaging.

For the remote sensing of neurodegeneration, we measure the speckle decorrelation time of ex vivo mouse brain samples afflicted by prion disease, a neurodegenerative disease similar to Alzheimer's, Parkinson's, and Huntington's disease. Using statistical significance tests and classifiers to determine healthy and diseased brain populations, we determine DCS to be sensitive to neurodegeneration based on brain stiffness changes.

For cancerous tumour imaging, we develop a novel DCS implementation that can capture relative stiffness differences of tissue in wide-field. We test our device on a hidden tumour proxy made by stiffening healthy brain tissue with a fixative. We obtain a ground truth of the fixed tissue by fluorescent tagging the fixed tissue regions, which correlates well with our DCS method.

In the final part of the thesis, improvements to our current DCS techniques are outlined. DCS in the context of sensing and imaging tissue, requires long acquisition times, and to speed the process of DCS up, we developed a machine learning (ML)-DCS model and experiment with speckle contrast imaging that can both image a tumour proxy at medically relevant times of 1 s.

Contents

List of Tables

List of Figures

List of Acronyms

Author Contributions

1. Ilya Starshynov, Alex Turpin, Philip Binner, and Daniele Faccio. "Statistical dependencies beyond linear correlations in light scattered by disordered media." Physical Review Research 4, no. 2 (2022): L022033.

2. Philip Binner, Ilya Starshynov, Aisling McFall, Gonzalo Tejeda, Valentin Kapitany, Colin Molloy, Andrew B. Tobin, and Daniele Faccio. "Remote Sensing of Neurodegeneration by Diffuse Correlation Spectroscopy." In Computational Optical Sensing and Imaging, pp. CW5B-6. Optica Publishing Group, 2023.

3. Steven S. Wong, Jack Radford, Philip Binner, Vytautas Gradauskas, Timothy G. Constandinou, Jinendra Ekanayake, and Daniele Faccio. "Multimodal Approaches for Real-time Mesoscopic Tissue Differentiation." In 2023 IEEE BioSensors Conference (BioSensors), pp. 1-4. IEEE, 2023.

4. Jack Radford, Matthew G. Smith, Philip Binner, Ilya Starshynov, Manlio Tassieri, and Daniele Faccio. "Machine Learning for Fast Statistical Sensing." In Computational Optical Sensing and Imaging, pp. CTu5B-2. Optica Publishing Group, 2023.

5. Vytatutas Graduaskas, Kevin Mitchell, Jack Radford, Ilya Starshynov, Samuel Nerenberg, Philip Binner, Ewan Wright, and Daniele Faccio. "Light Transport through Scattering Media." In Imaging Systems and Applications, pp. IF4D-1. Optica Publishing Group, 2024.

Acknowledgements

First and foremost, research of this nature would not be made possible without the sacrifice of animals. I would like to express my gratitude to the mice that died for the sake of human development herein and out of this thesis.

Secondly, I would like to thank my first and second supervisors, Prof Daniele Faccio and Prof Andrew B. Tobin and my unofficial supervisor, Dr Ilya Starshynov, who was deeply involved with all of my projects and with whom I very much enjoyed discussing everything inside and outside of physics.

Lastly, I would like to acknowledge both the past and present of the rest of the Extreme Light group, which I have been a part of in and out since 2018, as well as my friends and family, who have supported me through the PhD.

Preface

Cross-disciplinary research is very challenging but ultimately very rewarding. In doing it, one often needs to compromise between two fields of study but, on the other hand, builds new and meaningful connections with other researchers and obtains a more well-rounded view of their field. My PhD consisted of many cross-disciplinary projects involving biology and physics, which I approached from a physics background. As a subject that aims to describe and analyse the fundamentals of the universe, I believe physics is a broad tool that lends itself well to collaborative endeavours. In the thesis below, I have attempted to use and build on my knowledge of physics and apply it to biomedical imaging, a field that I have been interested in but did not formally study until taking this PhD.

Most, if not all, works that attempt to achieve originality and novelty require much experimentation, and the work I have outlined in the thesis below is no exception. I have attempted to write this thesis linearly, linking chapter to chapter for readability. However, in reality, research is often carried out in a very non-linear fashion, where one jumps from project to project as one tries out new ideas. In some cases, ideas do not work, and in other cases, ideas are tried out for one's own learning but do not necessarily constitute a worthy claim to the wider community. Because of that, many aspects of my PhD have not been documented in this thesis, as they simply do not fit its narrative anymore. Nonetheless, they are important steps to one's growth, and I feel they should be acknowledged somewhere. Therefore, in this preface, I would like to provide context and outline how the work was carried out.

Remote Assessment of Neurodegeneration

This project aimed to use scattered light to detect neurodegeneration and was led by my supervisors, Daniele Faccio and Andrew B. Tobin. It was one project that showcased a new building at my University, the Advanced Research Centre, which aimed to promote cross-disciplinary research. Andrew B. Tobin's group has exemplary publications in pharmacological and neurodegenerative research. Daniele Faccio's group centred around the fundamentals and applications of light, one new direction aimed at understanding the

brain.

The project was conceived when we heard that neurodegenerated brain samples tend to be 'mushier' than healthy brains. This prompted us to think of DCS, a popular optical technique for blood flow that is also sensitive to tissue dynamics, stiffness, and viscosity. This project was my introduction to biomedical imaging, and it came with many challenges, from constructing and optimising my first optical setup to preparing biological samples and devising methods to analyse experimental data. It was a very slow project because of these many overlapping themes. Mainly, it consisted of me experimenting with many types of tissue preparation and optical methods. For example, when we began the project, we were initially working with frozen brain samples, as it was a common procedure to freeze samples by our biology collaborators. Of course, in retrospect, freezing and defrosting a sample affects its structure, and we did not obtain meaningful results from using these samples. This project also showed us one limitation of DCS, its need for long acquisition times. To remedy this, we looked at a so-called multi-speckle method developed by Zakharov et al. [1]. We soon dropped this approach, as its benefits did not overcome its need for precise engineering, new analytical methods, and time requirements. Instead, we opted for the pixel-stacking approach introduced later in this thesis.

When we first began this project, we hoped to quickly translate our work to in vivo studies. However, the difference between neurodegenerated and healthy brains was not as clear as we had hoped. Ultimately, we needed to acquire data from many brain samples to perform statistical analysis and show a difference in DCS signal between neurodegenerated and healthy brains, which took many months as mice had to be bred for the experiment. When we eventually acquired enough data to perform statistical analysis, I also worked with statistical models, such as principal component analysis and t-distributed stochastic neighbour embedding. In the end, I opted for hypothesis tests on the raw data. One of the statistical models I used was a random effects model, which better reflected my experimental design than the models.

Tumour Imaging

This project began with a collaborator, Jinendra Ekanayake, a neurosurgeon and researcher who wanted a new remote method for intraoperative tumour imaging. It is common during surgery to manually test the brain's stiffness to distinguish tumours from healthy tissue i.e. by prodding the brain, which spurred us to create a DCS imaging device that could pick out relative features in a sample remotely. For this device to be medically relevant, we knew we would need to image something otherwise invisible to the naked eye. I began my work to use paraformaldehyde (PFA) as a tumour proxy soon after. Before

that, however, I mainly worked with TiO_2, a white powder commonly used in light scattering experiments. My preliminary experiments resided in embedding a mixture of TiO_2 and glycerol inside a sample, for which our DCS device was sensitive to. However, the similarity of this TiO_2 and glycerol mixture embedded in a sample to a tumour was tenuous. It came to me afterwards that PFA, a fixative used almost daily by our collaborators in Andrew B. Tobin's group, was a better alternative, as it could increase the stiffness of a sample without drastically altering its appearance, similar to how a tumour may act. Discussion on the PFA tumour proxy is continued in Chapter 5. With the above neurodegeneration sensing project knowledge, this project evolved much faster than the former. Currently, we are honing down on a suitable animal model to showcase our technique in a live imaging application.

Improvements to the DCS technique

Improvements to my work on DCS largely resulted from my network. I will discuss later using a ML model and otherwise laser speckle contrast techniques to improve the speed of DCS measurements. These projects developed through discussions with Jack Radford and Marija Vaskeviciute, two other PhD students at the time. I present the work of this project at the end of my thesis, but in reality, this began around a year into the PhD. We initially wanted to use this ML model to speed up the experimental process of the neurodegeneration sensing work. However, since we trained on simulated data and tested on noisy experimental data, we found that the ML model could not give an accurate DCS measurement and help distinguish between healthy and neurodegenerated brain samples. We then started gathering real data to train our model, which is currently a work in progress. After taking a break from working on this ML project and having instead developed DCS for tumour imaging, I found that our ML model worked very well when applied to our DCS imaging experiment. In this case, one does not necessarily need to obtain an accurate DCS measurement but rather obtain an image that can pick out relative differences in a sample. In parallel to using the ML-DCS model, we also worked on using laser speckle contrast techniques, as they could be applied to the very same DCS data we had obtained.

Declaration

In a few cases in this thesis, I have presented techniques and results made by others. I have attempted to state throughout the thesis what work is not my own, but I will also make a list below:

- Simulations of generating speckle patterns and involving the coupled dipole approximation were first made by Ilya Starshynov. My work involved adapting his code for dynamic media undergoing Brownian motion.
- Animals were taken care of by Aisling McFall, Gonzalo Tejeda, and Colin Molloy.
- Western blots performed to measure prion protein content in our neurodegenerated mouse models were performed by Aisling McFall. I have presented her results for extra context in my thesis.
- Giuseppe Ciccone or Matthew Walker performed all nanoindenter measurements involving the Chiaro.
- The machine learning model used to optimise my DCS experiments was initially made by Jack Radford for a similar application. I adapted the model for my DCS data structure and trained and tested that new model myself.
- The speckle contrast algorithm used in Chapter 6 was made by Marija Vaskeviciute. I implemented it on my DCS data.

The projects outlined in this thesis generally developed through group discussions, and I will largely use the plural pronoun to acknowledge and be inclusive of the contributions of others that cannot necessarily be tracked. That said, I declare that I carried out all other work contained in this thesis.

CHAPTER 1

Introduction

Biology and physics have had a long-standing symbiotic relationship, where biology research harnesses physics to explore the fundamentals of life. The microscope, for example, is a commonplace tool in all biomedical research laboratories, as are magnetic resonance imaging (MRI), positron emission tomography (PET), and computed tomography (CT) scanners in hospitals. These physics-based tools help us to gain insight and new perspectives into various health conditions.

Optical technologies are particularly promising tools that could benefit biomedical research. These tend to be cheap and simple in design, as I will show later in this thesis. I am particularly interested in using optics for brain applications. So little is known about the brain, and to this day, cancer and dementia are two health conditions that are widespread throughout the globe.

Intuitively, when we think of light, we may think simply of how light reflects off objects and enables us to see. However, much of the light that we see is not so much reflected but scattered off so many things before it reaches our eyes, and this scattering encodes a lot of information. For example, light scatters as it travels through clouds, and we can often tell a rain cloud by its darker shade. Or we can perceive different objects with different colours through scattering and absorption. In this thesis, I look at new biological applications of scattered light.

1.1 Thesis Overview

Chapter 2 defines the problem statement of this thesis, which are two worldwide health conditions: cancer and dementia. Cancer and dementia are both life-threatening diseases, but interestingly, both diseases incur stiffness changes in the brain that we may use to our advantage. Optical technologies sensitive to tissue stiffness are reviewed, where DCS appears to be a promising technique to develop for sensing and imaging the above two

diseases due to its popular usage in both animal and human applications and cheap and simple designs. Therefore, the rest of this thesis is dedicated to applying and advancing DCS.

Chapter3 focuses on the technical background of DCS, multiple light scattering, and the speckle pattern. Mathematical principles of the speckle pattern and how to generate a speckle pattern made by light scattering in a medium undergoing Brownian motion are discussed. Past and new elements of DCS are also covered in the format of short tutorials on how to perform DCS for sensing and imaging applications. This chapter aims to outline contextual physics for the remaining chapters.

Chapter 4 focuses on the first application of DCS, which is in the remote sensing of neurodegeneration. Here, we work with a neurodegenerative mouse model, which can be infected with prion disease at an accelerated rate. We use DCS to measure the temporal statistics of healthy and diseased mouse brains ex vivo. By cross-referencing our optical DCS measurements with other standard mechanical measurements and using statistical significance tests and classifiers, we justify DCS's power in diagnosing neurodegeneration.

We look at the second application of DCS in Chapter 5, which is in imaging brain tumours. This particular application of DCS would be helpful for intraoperative tumour imaging to aid surgeons in more complete tumour removal. This section covers a new implementation and application of DCS. We worked with a tumour proxy created by stiffening healthy tissue with a well-known biological fixative, PFA. The rest of this chapter shows as a proof of concept that DCS can be used for imaging.

Chapter 6 steps back from particular applications of DCS and instead aims to improve the current DCS technique, which for tissue measurements is hindered by long acquisition times. We outline two methods here. One of the methods substitutes DCS with a ML model that outperforms our current DCS method for short acquisition times. Instead of using DCS, the other method studies the contrast of the speckle pattern, which also improves on DCS at short acquisition times.

Lastly, Chapter 7 concludes the work carried out in this thesis and identifies areas in which that work could be expanded.

CHAPTER 2

A Literature Review of Light for the Measurement of Tissue Mechanical Properties

2.1 Worldwide Medical Conditions

Many people can live longer and healthier because of improved healthcare. However, this has also seen a substantial growth in age-related problems, notably dementia,[2]. Dementia here is an umbrella term that covers many neurodegenerative disorders. Many of us most likely know of dementia in more personal ways. For example, we may know someone who has been afflicted with a specific neurodegenerative disease: Alzheimer's disease, Huntington's disease, Parkinson's disease and many more. The last Alzheimer's report that focused on the global impact of dementia was written in 2015 and concluded that 50 million people worldwide lived with dementia. This number is predicted to rise to 130 million people by 2025, a vast proportion of these cases contributed by low- and middle-income countries. Not only does dementia impose on an individual and their family, but therapy for neurodegeneration also poses a substantial problem for the economy [3]. The causes of neurodegeneration are currently unknown, and research exists to understand and treat its underlying mechanisms. Dementia study is thus a very active and vital area of study.

Like dementia, cancer is also a growing condition for ageing populations and is the leading cause of death in many countries [4, 5]. Unlike neurodegeneration, however, the causes of cancer are now well known [6], and the condition is treatable with chemotherapy, radiotherapy or surgery, where life-threatening tumours are removed.

Tumour removal surgery is one of many challenging aspects of cancer treatment and is associated with many complications and risks [7, 8]. Here, in situ devices that could help

surgeons better envision the location of tumours and aid in complete tumour removal are desired. Nowadays, many cheap imaging methods and devices are available that could benefit cancer research in the above respect.

The above health conditions set the problem statement of the work conducted in this thesis. I aim to find new imaging and sensing methods that could benefit cancer and dementia research.

2.2 Imaging Modalities and Biomarkers for Dementia and Cancer

2.2.1 Dementia

Certain aspects of dementia research and treatment could benefit from new diagnostic tools. For example, a tool that could help in early neurodegeneration diagnosis could mean earlier and more effective treatment. Otherwise, cheaper and portable diagnostic tools would be well suited to research labs or smaller hospitals. Noninvasive tools, such as MRI, PET or CT scanners are very beneficial but often have limited availability due to their costs. In research settings, where expensive equipment is harder to come by, cheaper noninvasive alternatives are desired. For example, noninvasive tools can be used for longitudinal rather than postmortem studies, and reduce the number of animals required in a study.

There are three broad categories for neurodegeneration diagnosis: behavioural and symptomatic assessment; postmortem assessments, such as histology; and clinical assessments, such as MRI, PET, and CT scans. MRI, PET and CT equipment are generally costly and require extensive training, though they are the most robust methods for assessment. Such devices are standard in some hospitals, but patients will likely have to travel to select locations. They are, therefore, under constant use and in high demand. Furthermore, it is much rarer for a particular lab to own one. It is more common in research to use postmortem methods to quantify neurodegeneration, at least for work on neurodegenerative animal models. For example, histology and Western blotting analyses may be conducted to study the spreading of a neurodegenerative disease. Postmortem diagnostics are not ideal, as they prevent one from performing a longitudinal analysis of disease spreading and disease therapy. A Western blot, also known as immunoblot, and immunohistochemistry are standard postmortem techniques to assess neurodegeneration [9–14]. These are typically multi-step and lengthy processes that require training and many different experimental components, such as animal model-specific antibodies, centrifuges, microtomes,

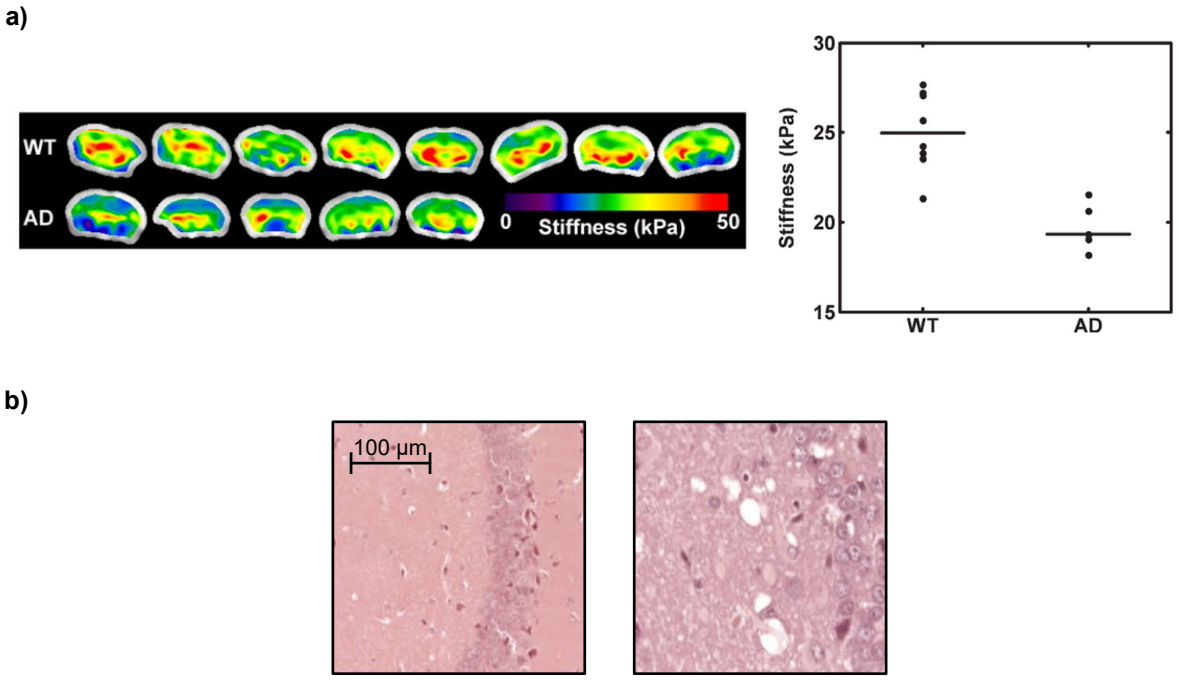

Figure 2.1: **Structural changes in the brain associated with neurodegeneration.** a) shows stiffness colour maps from MRE measurements on healthy wildtype mice and mice from an Alzheimer's disease model on the left. On the right are two box plots of stiffness measurements. A solid horizontal line represents the median value, and individual points represent the median stiffness of a single mouse brain. Both figures were taken from [15]. b) shows a haematoxylin and eosin stain of a healthy mouse brain (left) and that of a neurodegenerated brain affected by prion disease (right). This particular structural change is known as spongiosis. Figure adapted from [16].

and microscopes. Therefore, they are not ideal, and a novel postmortem method that is either simpler or quicker than these techniques would be valuable.

Otherwise, behavioural tests are qualitative analyses that may be used to complement the above methods. For example, they may screen patients before follow-up assessment with high-demand equipment. Behavioural tests, however, are primarily subjective and vary depending on the examiner. Neurodegeneration may be characterised by hallmarks such as a loss of cognitive ability and impairments to learning and memory [9], giving rise to various symptoms that behavioural tests can probe. These methods often include cognitively challenging exercises. For example, standard behavioural tests for mice are navigating a maze or undergoing memory tasks for food rewards [17, 18]. There are other behavioural methods, however, such as examining deficiencies in a mouse's ability to burrow [10], or fear conditioning, which tests a mouse's ability to associate pain or punishment with certain situations [9]. For example, a mouse affected by neurodegeneration will have a different fear response to electric shocks than a healthy mouse.

MRI or CT methods generally look at the brain's structure. Early examples here found

a reduction in hippocampus volume and brain density associated with neuronal loss [19–21] or modifications to the tissue structure, such as spongiosis [16, 22]. However, more recent experiments have studied mechanical properties of the brain, stating a reduction of stiffness in both animal models [15, 23–26] and in clinical tests on humans [23, 27–35] associated with neurodegeneration. These studies which map the elasticity or other tissue characteristics beyond imaging are more formally known as magnetic resonance elastography (MRE). Figure 2.1 shows examples of structural changes from a live MRE study and a postmortem histology study on two neurodegenerative mouse models, an Alzheimer's mouse model and a prion disease mouse model. Studies have also been conducted on mechanical changes associated with ageing, which have produced similar reductions in brain stiffness [36–38]. An optical technique that could also measure the mechanical properties of brains afflicted by dementia would be highly valuable due to its cost and portability.

2.2.2 Cancer

Cancerous tissue may differ from healthy tissue in many ways. One well-known example is the difference in mechanical properties between tumours and healthy tissue, where several studies report differences in stiffness between tumours and healthy tissue [39–48]. Figure 2.2 shows example MRI and MRE scans of a mouse tumour model, where a tumour is significantly softer than the normal-appearing brain matter.

Changes in the tumour microenvironment compared to healthy tissue have also been found [45, 49–52]. These could be variations in water content, pH, and oxygenation, to give a few examples. The above differences make it possible to discern tumours from healthy tissue through structural or functional imaging methods. Indeed, many imaging modalities may image tumours: CT, MRI, X-ray, PET, and single-photon emission computed tomography (SPECT) [53–56].

Due to their high resolution and sensitivity, MRI scans are considered the gold standard imaging method for many areas of the body, notably the brain. It is standard protocol to use an MRI machine before surgery to guide tumour removal; however, in the operating room, an MRI device is not viable due to its bulky nature and long exposure times. Moreover, mechanical rheology devices are also not viable due to being invasive and requiring lengthy scanning procedures. On the other hand, optical techniques can be very compact, and some can differentiate tumours from healthy tissue in situ. Raman spectroscopy, for example, is an optical method used in intraoperative settings. However, this is currently invasively done with needle probes and requires scanning, which could lead to long measurement times [57–59]. Some labelled optical methods exist for more noninvasive implementations, where a fluorescent dye is first administered into the body for an image

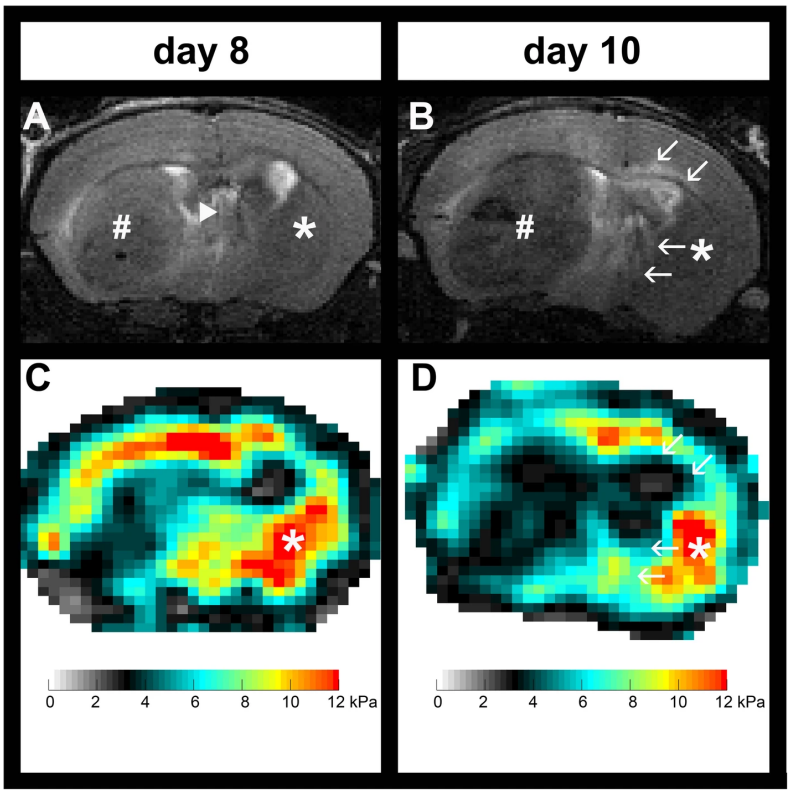

Figure 2.2: **Mouse brain glioblastoma MRE example.** a) shows an MRI scan of a mouse brain with a glioblastoma indicated by a #. Normal-appearing brain matter is denoted by a *, and a white arrow points out a deformation in the brain as its mid-line is shifted right. The image was taken eight days post-tumour implantation. b) shows another scan repeated after two more days, where the tumour has grown. c) and d) show the corresponding MRE scans, where the tumour region is significantly softer than the surrounding tissue. Figure taken from [46].

to be built. This is a form of functional imaging whereby the fluorescence signal arises from changes in cell metabolism [51, 60].

Label-free optical methods do not require the sample to be stained, for example with a fluorescent dye, before imaging. Many dyes can be toxic to the body, so label-free methods are sought after since they require no alteration of and are non-destructive to the body. Recently, a hand-held multi-spectral device has been used to capture the autofluorescence of the brain and perform tumour segmentation [61, 62]. However, this setup requires a scanning approach, where an imaging device would be more intuitive for a surgeon to understand. Thus, there are many options for intraoperative tumour imaging. However, each comes with a drawback, which calls for the development of novel techniques in this field.

2.3 Label-Free Optical Technologies with Sensitivity to Tissue Stiffness

In the last section, we saw that a common element between cancer and neurodegeneration was that they came with stiffness changes associated with their progression. Rheology is an area of research that studies the deformation and flow of materials and parameterises materials based on parameters like stiffness, viscosity, viscoelasticity, stress, and strain [63]. Common devices used for rheology include the MRI scanner, shear rheometer, and nanoindentation devices, such as the atomic force microscope (AFM). Mechanical tools such as shear rheometers and nanoindentation devices were the first to be developed. These are contact tools that test the response of a sample based on a mechanical perturbation or load. For a shear rheometer, a rotatable probe contacts the surface of a sample. The sample deforms as the probe rotates, and the probe's angular position and torque can be used to determine its shear modulus. If the probe is rotated at an angular frequency ω, then the shear storage G' and loss G'' moduli can be found. These two measurements are often likened to stiffness and viscosity in the rheology community. The dynamic modulus is often used, which is a combination of the above two moduli, defined as $G^* = G' + iG''$ and referred to as viscoelasticity. Otherwise, nanoindentation devices measure a material's Young's modulus, denoted by E instead of G, as in $E = E' + iE''$. In isotropic cases, E and G are linearly related by $E = 2G(1 + \nu)$, where ν is Poisson's ratio and describes the sample's ratio or transverse over axial strain of a sample. Shear devices generally have millimetre-sized probes and are used for homogeneous and large samples, whereas nanoindentation devices have micrometre-sized probes and are used for heterogeneous or small samples. However, the above shear and nanoindentation devices cannot be used non-invasively. MRE has been a rapidly developing technology that can measure G' and G'' in these cases. For example, we have already seen that MRE has been used to assess neurodegeneration.

Changes in stiffness associated with neurodegeneration and cancer are interesting findings regarding making novel diagnostic tools for dementia. It is common to probe viscoelasticity mechanically using an atomic force microscope, but a contact probe is not ideal for in vivo situations. However, many optical methods are now sensitive to tissue mechanical properties, which may indeed be well suited for neurodegeneration and cancer diagnostic applications. These techniques can be label-free, made of cheap components, and range from minimally to noninvasive implementations. Therefore, the rest of this chapter will be dedicated to such techniques.

2.3.1 Diffuse Correlation Spectroscopy

DCS [64–68] uses scattered coherent light to probe a dynamic material. When coherent light scatters through a medium, a complex interference pattern known as a speckle pattern is produced. If, for example, the scatterers inside the medium undergo random motion, such as Brownian motion, then the light that scatters through the medium undergoes random phase changes with respect to the motion of scatterers, resulting in a speckle pattern that changes over time. An autocorrelation function can be used to study the speckle pattern's intensity fluctuations over time. The autocorrelation of the speckle pattern yields a decaying exponential due to the memoryless, Markovian nature of the random scatterer motion and randomisation of the light's phase over time. Therefore, the speckle pattern may be characterised by its $1/e$ value, known as the speckle decorrelation time. This speckle decorrelation time is linked to the scattering medium's particle motions or mean-square displacement of particles [69].

The DCS technique has been around for over sixty years, dating back to near the advent of the laser, and has been called several names since. For simplicity, I will briefly summarise its various monikers here and refer to them wholly as DCS in the later parts of this thesis. The first implementation of DCS was known as dynamic light scattering (DLS), which specifically studied single scattering events and was first applied to colloidal solutions [70]. Then diffusing wave spectroscopy (DWS) was introduced by Pine and Maret et al. in the late 1980s, which expanded on DLS and studied multiple scattered events of light [65, 66, 71]. Later came DCS in the early 2000s [67], which technically does not differ from DWS but was popularised for blood flow measurements.

DCS was first coined by Cheung et al. [67], who used scattered light to noninvasively study variations in cerebral blood flow, haemoglobin concentration and blood oxygenation. This important finding showed that scattered light could be used to perform functional and non-invasive brain sensing. After that emerged several new methods that focused on blood flow [72–79]. Of note are the state-of-the-art studies conducted by Roarke Horstmeyer's group [78, 79] in 2021/22, who used DCS to measure brain activation based on blood flow rate as well as perform up to ~ 5 mm deep imaging of blood vessels. This was made possible with the incorporation of high frame rate single-photon avalanche diode (SPAD) cameras, where it was shown that the signal-to-noise ratio (SNR) of DCS measurements could be significantly improved [80, 81]. Here, SPADs improved upon the scanning required by single photodiode setups and the spatial resolution photodiode arrays and photomultiplier tubes, commonly in DCS measurements [67, 82–85].

Figure 2.3 shows a characteristic DCS setup for measuring blood flow in a human head in vivo. (a) summarises the setup, consisting of a laser, multimode fibres and SPAD array

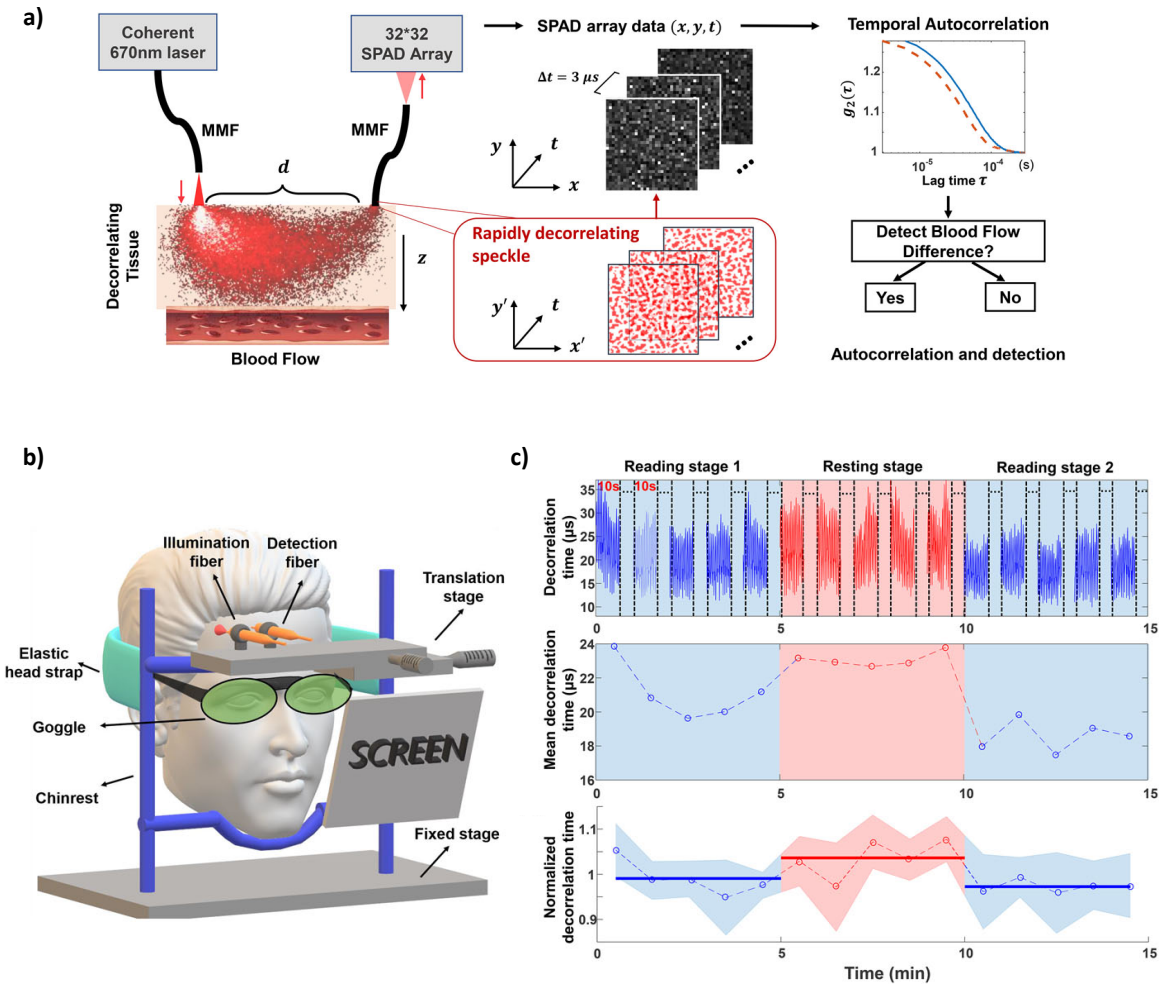

Figure 2.3: **A characteristic DCS setup.** This device was used by Liu et al. to measure brain activation in the prefrontal cortex from blood flow. Figure taken from [78]. a) A typical process for a DCS experiment. Light is delivered into the body through a multimode fibre, then scatters and is collected by another fibre and camera. The speckle temporal decorrelation of the light is then measured and will be short for fast-flowing blood and long for slower-moving blood. b) Liu et al.'s setup for imaging the prefrontal cortex during a reading exercise. c) Liu et al.'s results for the reading exercise. The speckle decorrelation is faster during the reading exercise when the prefrontal cortex is engaged and requires more blood than in periods of rest.

camera. It measures brain activation based on the speed of blood flow and decorrelation of the speckle pattern over time. Increasing the source-detector separation d allows one to select the light scattered deeper into the tissue and off the blood. (b) shows how the device is fitted onto a human head for prefrontal cortex measurements, and in (c), three separate plots show how the speckle decorrelation time changes during a reading exercise. This exercise engages the prefrontal cortex, causing a higher blood flow rate into that brain region. This particular example of DCS shows the current state-of-the-art of the technique, which is now being used in vivo and live applications.

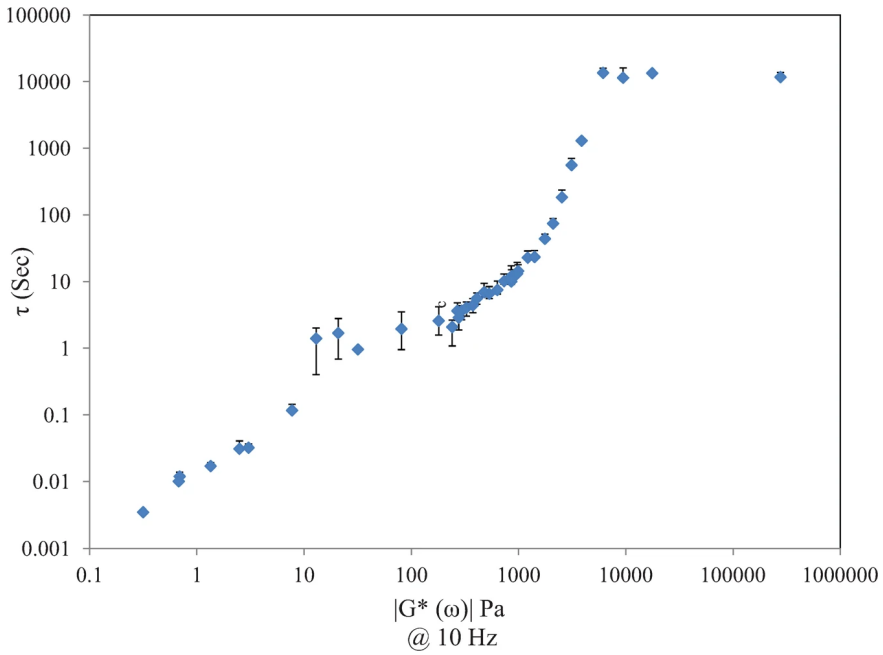

Figure 2.4: **Speckle decorrelation time vs the absolute value of the dynamic modulus.** Figure taken from [86]. The relationship is roughly linear for speckle decorrelation times from 0 to 100 s, indicating that τ_c may be used to measure stiffness in a contact-free manner.

Blood flow measurements represent the so-called fast regime of DCS measurements, whereby blood travels very quickly. However, other biological processes move at much slower timescales and may also be functional biomarkers. The works of Hajjarian and Nadkarni et al. are exciting recent developments relating to DCS in the slow regime, which they have termed laser speckle rheology [86–92]. These above articles have linked mechanical rheometer shear modulus measurements to speckle decorrelation time measured by DCS, creating an optical and contactless rheology method. Figure 2.4 shows a plot of speckle decorrelation time τ_c against shear rheometer measurements of the dynamic modulus $|G^*|$. Here, $|G^*| = |G' + G''|$ is often likened to the viscoelasticity of a material and is a combination of the storage modulus G' ('stiffness') and loss modulus modulus G'' ('viscosity'). The relationship between τ_c and $|G^*|$ is effectively linear. Similar work on optical rheology has also been done in the past [93, 94].

DCS remains a popular technology for its cheap components and general ease of application. It has many ties with biology that can be roughly split into two fields: the fast regime of DCS measurements, which relate to blood flow, and the slow regime of DCS measurements, which relate to tissue mechanical properties, like stiffness. Both fields have great potential for development into functional imaging or sensing diagnostic tools for disease. However, I am more interested in the slow regime for my thesis, as this may be connected to neurodegenerative diseases and tumour segmentation.

2.3.2 Laser Speckle Contrast Imaging and Speckle Contrast Optical Spectroscopy

Laser speckle contrast imaging (LSCI) and speckle contrast optical spectroscopy (SCOS) share the same underlying principles, where SCOS is an evolution of LSCI to less superficial layers of biological tissue. Like DCS, LSCI and SCOS are also applied to dynamic media and are well-suited for biological imaging. The differences between LSCI and SCOS are small and lie in their applications: LSCI is typically performed for wide-field imaging and has been use extensively for blood flow imaging [95–101]. On the other hand, SCOS tends towards deeper applications using optical fibres [102–104] and focuses more on tissue dynamics over blood dynamics [105]. The processing of data is however largely the same for both methods.

LSCI and SCOS are promising optical techniques because they are tailored for cheaper equipment. Both techniques study the 'blurring' effect seen in a speckle that occurs when the sample medium is dynamic. If the speckle intensity fluctuates quickly, the speckle contrast will be close to zero but will rise to one for a slowly changing speckle or no motion in the medium. Thus, both techniques may be used to segment heterogeneous media, media of varying dynamics. LSCI and SCOS do not necessarily need to resolve the speckle temporally, so they can be performed with cheaper complementary metal–oxide–semiconductor (CMOS) cameras rather than SPADs or photomultiplier tubes (PMTs). It should be noted here that the differences between LSCI and SCOS to DCS are very subtle. They all measure the dynamics of a speckle pattern, although their data is different. DCS data tends to have much higher temporal resolution, where high frame rate cameras are often used to capture small fluctuations in a speckle pattern's intensity. On the other hand, LSCI and SCOS data is taken by slow frame rate but high spatial resolution cameras, which instead capture the 'blurring' of a speckle pattern. Since these techniques share similarities to DCS, it is also worth investigating them. In Chapter 6, I employ LSCI for tumour imaging.

Some studies looked at relationships between speckle contrast and stiffness using LSCI. However, the samples in all these studies were driven by an external source, for example an ultrasound transducer [106, 107]. For LSCI to be more medically relevant, such as in intraoperative tumour imaging scenarios, it would be more desirable if it was non-driven. Recently, Liu et al. [105] used SCOS to determine the response between source-detector separation and speckle contrast. In doing so, they found that SCOS is sensitive not only to blood flow but to slow tissue dynamics, such as intracellular motility, and that this did not require an external driving source. This promising finding perhaps points towards a particular application of SCOS to probe tissue stiffness, much like how DCS and laser

speckle rheology do. However, the supporting literature for stiffness sensitivity is currently not as substantial for LSCI and SCOS as it is for DCS and laser speckle rheology.

2.3.3 Brillouin Microscopy

Brillouin microscopy is a label-free, contactless, and non-destructive optical elastography technique. It measures the interaction of coherent light with thermally induced acoustic waves, or phonons, in a sample media. Brillouin microscopy is similar to Raman spectroscopy. Where Brillouin microscopy operates on the bulk medium, Raman spectroscopy operates at the molecular level and instead studies the interaction of light with vibrational modes of the scattering medium [108, 109]. As light traverses the scattering medium, it may scatter elastically or inelastically. Rayleigh scattered light, encounters no frequency shift, but inelastically scattered light may incur negative and positive frequency shifts upon scattering. The negative and positive frequency-shifted light are usually called Brillouin Stokes or Brillouin anti-Stokes scattered light, respectively. The magnitude of the frequency shift is related to the rigidity of the medium, whereas the line width of Brillouin peaks is associated with the medium's viscosity [110, 111]. Figure 2.5 illustrates the Brillouin frequency shift for a heterogeneous medium.

Brillouin microscopy requires more sophisticated equipment than DCS, LSCI, or SCOS. Specifically, Brillouin microscopy requires a narrow-band frequency laser and a high-resolution spectrometer to measure minuscule spectrum shifts in output light, typically ranging from 1-20 GHz [110]. Because it measures frequency shifts, the only way to obtain an image with the technique is by raster-scanning, which generally requires long acquisition times. However, effort has been made to reduce acquisitions [112], even down to the sub-second regime [113], making the technique more medically relevant.

The advent of stimulated Brillouin scattering came as a solution to enhance the weak Brillouin signal. Here, two counter-propagating pump and probe beams are focused on the sample medium, whereby the probe laser is slightly detuned in frequency. The probe and pump beams stimulate an acoustic wave. A stimulated Brillouin spectrum is found by scanning the pump-probe frequency detuning over the Brillouin frequency shift. Stimulated Brillouin microscopy has been shown to have a better spectral resolution and less background originating from the Rayleigh scattered light [110, 111, 114, 115]. Generally, the pump laser here is high-power, which can damage fragile samples. However, there are non-destructive exceptions that use a pulsed probe laser, which is known as impulsive stimulated Brillouin microscopy [116]. Otherwise, another drawback of stimulated Brillouin microscopy is that it currently requires access to the sample from both sides for the counter-propagating probe and pump lasers. Thus, it is not viable for in vivo experiments

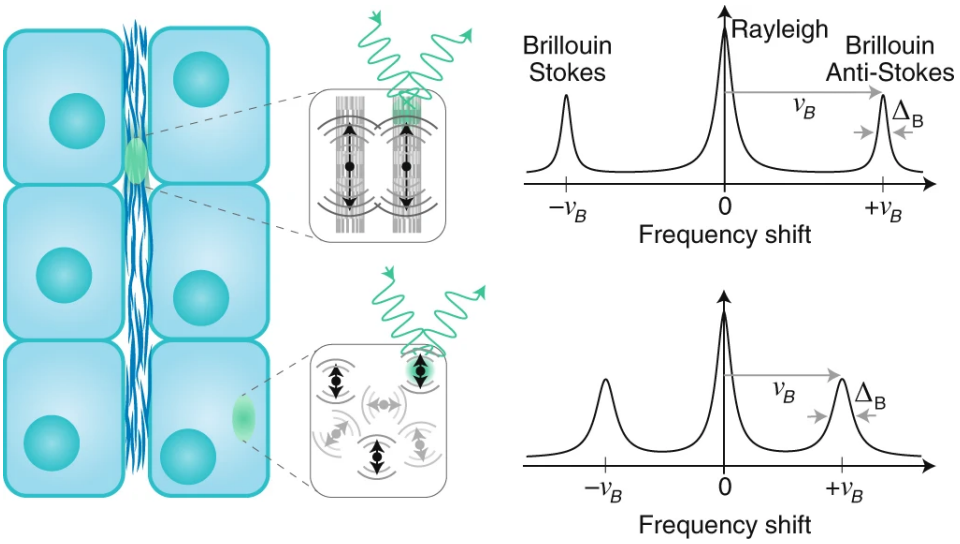

Figure 2.5: **Brillouin microscopy example.** An illustrative example of a heterogeneous sample made of collagen fibres sandwiched between two layers of liquid-like cytosol is shown on the left. Insets display the density and motion of scatterers and light interaction with them. On the right are two regimes of Brillouin frequency shifts. Light that inelastically scatters off solid (more stationary) parts of the sample experiences a large Brillouin frequency shift, whereas light that inelastically scatters off liquid (more dynamic) parts of the sample experiences a small shift. Figure taken from [110].

[114].

Brillouin microscopy was initially used for the study of condensed matter [117, 118] but is now being used broadly in biomedical imaging of bone and connective tissue [119–123], cardiovascular disease [124], cancer [112, 125–127], and neurodegeneration [128, 129]. Although it has a broad range of uses in biological imaging, Brillouin microscopy is generally restricted to cellular-level analyses instead of wide-field applications. Because of this, it may not be as valuable for in vivo applications on animals and humans as it would be better suited for microscopic sensing and imaging techniques.

2.3.4 Optical Coherence Elastography

Optical coherence elastography (OCE) [130–134] is a special application of the optical coherence tomography (OCT) technique for mechanical property measurements of tissue. OCT is an interferometric approach used to perform depth-resolved measurements of a sample. In OCE, however, a sample medium is mechanically perturbed or loaded with an ultrasound transducer or with a compression plate, and then the response of the medium is imaged with an OCT setup. In post-processing, mechanical models can be applied to the optical image to quantify tissue properties, like stiffness [133]. OCE is similar to the

older technique of ultrasound elastography, where the main distinctions between the two methods is better spatial and axial resolution for the former but better penetration depth for the latter [133].

Figure 2.6(a) shows a typical OCT setup. Low temporal coherence light is passed through a reference and sample arm of a Michelson interferometer. Here, a broadband light source light maximises OCE's depth resolution [135]. Due to the sample's heterogeneity in refractive index and scattering, light reflected off of it incurs phase differences with respect to the light passed through the reference arm. By moving the mirror in the reference arm from left to right, one can resolve the coherence of light at various depths through the sample. Lastly, a 3D image of the tissue can be obtained by scanning the sample arm over the area of the sample. Figure 2.6(b) shows three different OCE configurations. The first configuration on the left uses a compression plate to deform the sample. The second (middle) and third (right) configurations load the sample remotely. In the second configuration, harmonic OCE, the tissue resonates with the loading frequency due to boundaries in the sample. The load is pulsed in the third configuration, known as transient OCE. The loading transmits a shear wave across the sample's surface in both cases. The Young's modulus of the sample can be extracted from the shear wave speed, estimated from spatial cross-correlations of subsequent speckle pattern frames measured by the OCT device [132–134]. Figure 2.6(c) shows the results of an OCE study by Kennedy et al. conducted on excised cancerous breast tissue. The elastogram made through OCE helps to segment a tumour by giving information on its mechanical properties.

OCE is a quasi-invasive technique. Though no mechanical contact is made to the surface with ultrasound loading, the sample medium must still be perturbed so that OCE may test its response. In terms of optics, setups for OCT are more complicated than for DCS or LSCI. In OCE, an interferometer with a scanning arm is used to obtain depth measurements of a sample. Because of the need for mechanical loading and interferometric optical measurement, the alignment of OCE can be difficult, which makes it generally applicable for use as a tabletop piece of equipment but otherwise awkward as a hand-held device.

OCE is used often for tumour analysis [133, 134, 136, 137]. This is done on excised tumours rather than in situ and in vivo. OCE has not been applied extensively to neurodegeneration. One recent study [138] found stiffness changes associated with Alzheimer's and wildtype mouse models' wake and sleep cycles. Brain OCE measurements are challenging, however. In the above study [139], portions of mouse skulls were first replaced with a transparent window before OCE measurement could be performed. This is one method to perform deep imaging with OCE. Otherwise, needle probes are needed to obtain signals beyond a few millimetres [132, 140, 141]. Thus, the technique is invasive for deep appli-

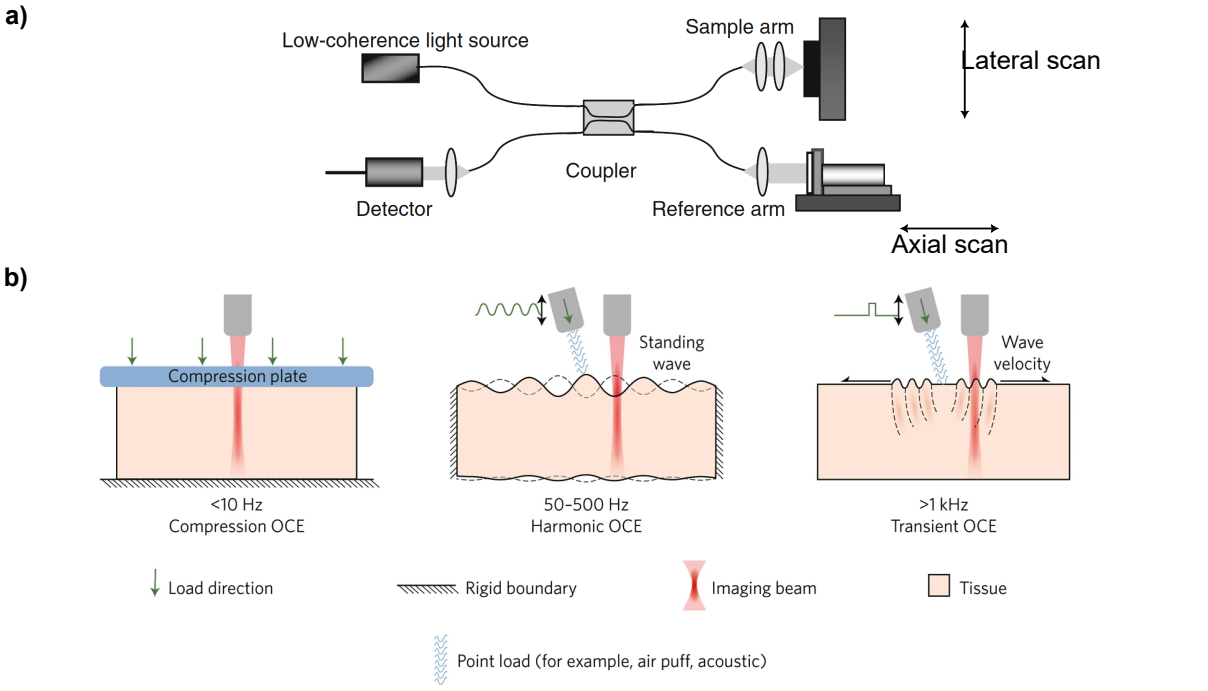

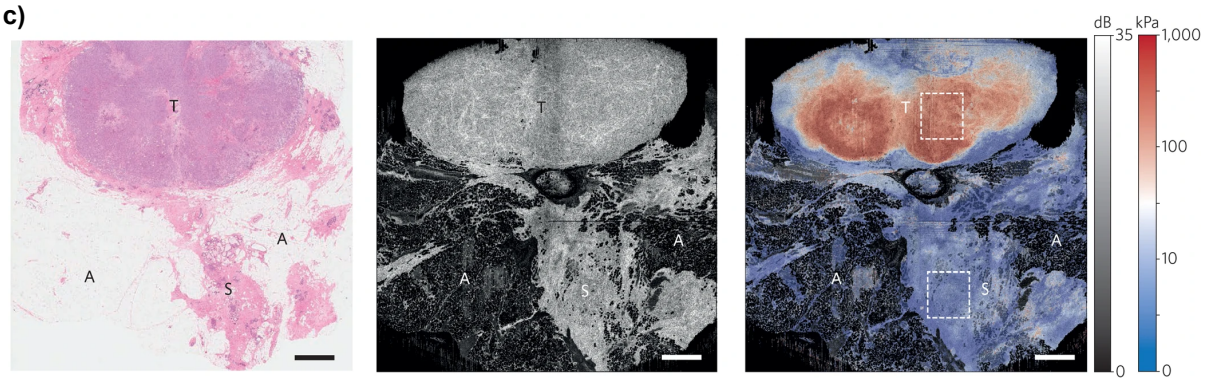

Figure 2.6: **An OCE example.** a) A standard OCT setup. Light is split into a sample and reference beam. The reference arm can move axially, which enables a depth measurement of the sample. The sample arm may be moved laterally, which enables a wide-field image of the sample through raster scanning. Light from both arms is combined at the detector. Figure taken from [135]. b) Three different OCE configurations, which from left to right use a compression plate, a harmonic ultrasound wave, and a transient ultrasound wave to load the sample. c) Example results from an ex vivo compression OCT study on cancerous breast tissue. From left to right, there is a histological stain, an OCT image, and an OCE elastogram of the breast tissue. A tumour is denoted by T and is higher in Young's modulus. Two types of connective tissue, adipose tissue and mature stroma, are denoted by A and S, respectively. Scale bars correspond to 2 mm. Figures (b&c) taken from [134].

cations, which limits its scalability as an in vivo assessment tool, for example, one that can perform assessments through the skin. Thus, OCE, like Brillouin microscopy, appears more suited to ex vivo studies at the micro-scale and depths up to 1-2 mm.

2.3.5 Optical Tweezers

Optical tweezers [142, 143] recently won the Nobel prize and are another optical technology sensitive to tissue stiffness [144–148]. This is achieved by tracking the mean-squared displacement of a particle suspended in an optical trap and undergoing Brownian motion. In doing this, pN forces exerted by the suspended particle can be measured. Optical tweezers are worth noting in this literature review because they may be used for mechanical property measurements. However, they cannot be used on bulk media, as the optical trap may only suspend micron-sized objects. They are ideal for microrheology measurements.

2.4 Conclusion

Neurodegeneration and cancer research are two areas that may benefit from further development of optical technologies. Noninvasive, contact-free, and cheap optical technologies are ideal here, and optical technologies that can perform deep sensing or imaging are also beneficial. Changes in tissue mechanical properties are known to be correlated with the progression of various diseases, and optical technologies sensitive to stiffness are promising. DCS, in particular, stands out as an exciting technology to develop since it has many promising qualities for noninvasive and in vivo sensing and imaging applications. It has cheap components, simple experimental layouts, and current usage in in vivo applications, to name a few. LSCI and SCOS are similarly exciting but with less background literature on tissue mechanical properties than DCS. OCE, Brillouin microscopy, and optical trapping seem to have more limited applications than the above techniques. A broad range of literature on these techniques are about ex vivo samples, for example, individual cells or excised sampled. Therefore, I have chosen primarily to work with DCS for the upcoming thesis.

The upcoming chapters will focus around DCS in the context of neurodegeneration and cancer assessment. In the next chapter, mathematical preliminaries and how to perform DCS will be discussed. Chapter 4 will detail work implementing DCS for sensing neurodegeneration-based stiffness changed in brain samples of a neurodegenerative mouse model. Chapter 5 discusses DCS for imaging a tumour proxy on mouse brain tissue. Chapter 6 delves into DCS' acquisition time, one of its major limitations, and possible

methods to overcome it with ML and other speckle-based imaging techniques. The final chapter will discuss the prospects of the experiments undertaken in this thesis.

CHAPTER 3

Diffuse Correlation Spectroscopy: Technical Background

Introduction

In the previous chapter, DCS, among other optical techniques, was discussed in a general manner. DCS was found to be a promising optical technique that is already being used for even human applications. Since I am applying DCS to various biological applications in this thesis, I would like to provide a more technical overview of the DCS technique in this chapter. This will be a primer for the proceeding content, where DCS is applied to different biological applications. Some of the work in this chapter will be novel, but it still constitutes the technical background for the proceeding material.

3.1 Multiple Light Scattering and the Speckle Pattern

DCS is a scattered light technique. One must have a broad picture of how light propagates through a medium to understand how it works. In many applications of DCS, the medium in question is random, meaning that the distribution of its particles is random. Furthermore, the medium in question also tends to be dynamic, randomly moving over time. Both aspects are true in this thesis, so I will attempt to describe multiple light scattering in a dynamic random medium.

3.1.1 First-Order Statistics of the Speckle Pattern

The first-order statistics of light describe its properties at a single point in space or time [149]. A speckle pattern is a specific type of interference pattern generated by the scattering of light from a random medium. Phasor sums may aptly describe light scattering in the

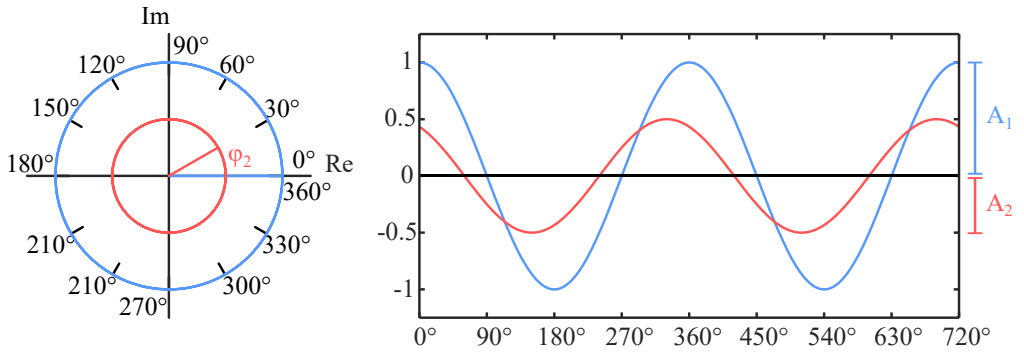

Figure 3.1: **A sine wave and corresponding phasor diagram**. On the right panel are two sinusoidal waves (made with Equation 3.1) with amplitudes $A_1 = 1, A_2 = 0.5$ and phases $\phi_1 = 0°, \phi_2 = 30°$ (blue and red respectively). A phasor diagram (left) tracks the amplitudes and phases of both waves in the complex plane.

medium. A phasor, A, is a signal of a fixed frequency that varies in amplitude and phase. It may be described by the following formula,

$$A = ae^{i\phi}, \tag{3.1}$$

for amplitude A and phase ϕ. An example simple sinusoidal wave is illustrated in Figure 3.1 with a corresponding phasor diagram. In this diagram, ϕ conventionally rotates anti-clockwise as the sin wave moves to the right.

As light scatters through a medium, it takes multiple different paths and encounters many scattering events. The generation of a single speckle feature may be thought of as a combination of these different paths and scattering events. This can be represented by a resultant phasor that is the linear addition of many independent phasors,

$$A = \frac{1}{\sqrt{N}} \sum_{n=1}^{N} a_n e^{i\phi_n}, \tag{3.2}$$

for an n^{th} component phasor $\mathbf{a}_n$ and N number of phasor components. The resultant phasor A is complex, and when split into its real $\mathcal{R}$ and imaginary $\mathcal{I}$ components, it may be understood as,

$$\begin{aligned} \mathcal{R} = \mathrm{Re}\{\mathrm{A}\} &= \frac{1}{\sqrt{N}} \sum_{n=1}^{N} a_n \cos(\phi_n), \\ \mathcal{I} = \mathrm{Im}\{\mathrm{A}\} &= \frac{1}{\sqrt{N}} \sum_{n=1}^{N} a_n \sin(\phi_n), \end{aligned} \tag{3.3}$$

which have expectation values of zero and variances of,

$$\begin{aligned} E[\mathcal{R}] = E[\mathcal{I}] = 0, \\ \sigma_{\mathcal{R}}^2 = E[\mathcal{R}^2], \\ \sigma_{\mathcal{I}}^2 = E[\mathcal{I}^2], \end{aligned} \tag{3.4}$$

where $\sigma_{\mathcal{R}}^2 = \sigma_{\mathcal{I}}^2$.

The joint probability density function (PDF) of the speckle is a function of its real and imaginary parts and can be expressed in terms of its amplitude and phase,

$$\begin{aligned} p_{\mathcal{R},\mathcal{I}}(\mathcal{R},\mathcal{I}) &= \frac{1}{2\pi\sigma^2}\exp\Big[-\frac{\mathcal{R}^2+\mathcal{I}^2}{2\sigma^2}\Big], \\ p_{A,\phi}(A,\phi) &= P_{\mathcal{R},\mathcal{I}}(\mathcal{R},\mathcal{I})\left\|\begin{array}{cc} \partial\mathcal{R}/\partial A & \partial\mathcal{R}/\partial\phi \\ \partial\mathcal{I}/\partial A & \partial\mathcal{I}/\partial\phi \end{array}\right\|, \\ p_{A,\phi}(A,\phi) &= \frac{A}{2\pi\sigma^2}\exp\Big[-\frac{A^2}{2\sigma^2}\Big], \end{aligned} \tag{3.5}$$

for $A = \sqrt{\mathcal{R}^2+\mathcal{I}^2} = \sqrt{(A\cos\phi)^2+(A\sin\phi)^2} \geq 0$ and $[-\pi \leq \phi < \pi]$. Here, the central limit theorem is used, which states that as $N \to \infty$, the sum of N independent phasors becomes asymptotically Gaussian. The joint PDF may be split in terms of the marginal probabilities of A and ϕ like below,

$$\begin{aligned} p_A(A) &= \int_{\pi}^{\pi} P_{A,\phi}(A,\phi)d\phi = \frac{A}{\sigma^2}\exp\Big[-\frac{A^2}{2\sigma^2}\Big], \\ p_\phi(\phi) &= \int_0^{\infty}\frac{A}{2\pi\sigma^2}\exp\Big[-\frac{A^2}{2\sigma^2}\Big]dA = \frac{1}{2\pi}. \end{aligned} \tag{3.6}$$

Thus, for a large number of component phasors, or scattering events, the amplitude and intensity of the speckle follows a Rayleigh distribution, and its phase is uniformly distributed between $(-\pi,\pi)$. Moreover, A and ϕ are statistically independent, i.e., $p_{A,\phi}(A,\phi) = p_A(A)p_\phi(\phi)$. If a speckle obeys these two conditions, then it is referred to as a fully developed speckle.

In practice, one usually measures the intensity of a speckle pattern. For polarised light, the intensity $I = |A|^2$. A fully developed speckle may then be described by the following PDF, which is found from Equation 3.6 using the property that mean intensity $\langle I\rangle = 2\sigma^2$,

$$p_I(I) = \frac{1}{\langle I\rangle}\exp\frac{-I}{\langle I\rangle}. \tag{3.7}$$

However, in the case of multiple light scattering in a random medium, it is more accurate to describe the output light as unpolarised, as each scattering event will polarise the light

in some axis. Therefore, a speckle pattern generated by multiple light scattering will be a combination of different polarisations of light, and we can say that the detected intensity I_s is a sum of independent intensities $I_1 + I_2$. For simplicity, we use two different polarisations, which are assumed to be fully developed speckles according to,

$$\begin{aligned} P_1(I_1) &= \frac{1}{\langle I_1 \rangle} \exp\left[\frac{-I_1}{\langle I_1 \rangle}\right] \\ P_2(I_2) &= \frac{1}{\langle I_2 \rangle} \exp\left[\frac{-I_2}{\langle I_2 \rangle}\right]. \end{aligned} \tag{3.8}$$

To obtain the PDF of I_s, we can take the inverse Fourier transform of the product of characteristic functions for I_1 and I_2. Specifically, according to the convolution theorem, the characteristic function of I_s, M_s is the product of characteristic functions of I_1 and I_2 (M_1 and M_2 respectively),

$$M_s = M_1 M_2 = \frac{1}{1 - i\omega\langle I_1 \rangle} \frac{1}{1 - i\omega\langle I_2 \rangle}. \tag{3.9}$$

On inverse Fourier transforming M_s, we can obtain,

$$\begin{aligned} P_s(I_s) &= \frac{1}{\langle I_1 \rangle \langle I_2 \rangle} \left[\exp\left(\frac{-I_s}{\langle I_1 \rangle}\right) - \exp\left(\frac{-I_s}{\langle I_2 \rangle}\right) \right], \text{ for } \langle I_1 \rangle > \langle I_2 \rangle \\ P_s(I_s) &= \frac{I_s}{\langle I \rangle^2} \exp\left(\frac{-I_s}{\langle I \rangle}\right), \text{ when } \langle I_1 \rangle = \langle I_2 \rangle = \langle I \rangle, \end{aligned} \tag{3.10}$$

showing that for unpolarised light the speckle intensity will always be non-zero.

Of note is also the speckle contrast, which is the ratio of the speckle's standard deviation over its mean,

$$K = \frac{\sigma_I}{\langle I \rangle}. \tag{3.11}$$

For a fully developed speckle, $K = 1$ [150]. Here, the mean of the speckle is equal to its standard deviation, which makes the speckle pattern visually look like a random arrangement of high-contrast dark and bright spots. Again for unpolarised light, the speckle contrast will decrease due to the summation of independent speckles and may be described by the below equation,

$$K_s = \frac{\sigma_s}{I_s} = \frac{\sqrt{\langle I_1^2 \rangle + \langle I_2^2 \rangle}}{\langle I_1 \rangle + \langle I_2 \rangle}. \tag{3.12}$$

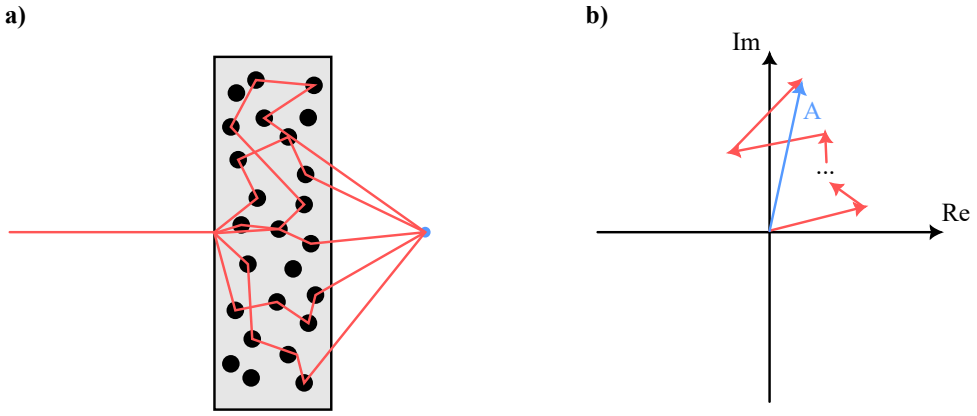

Figure 3.2: **Phasor Diagrams**. a) an illustration of light scattering in a random medium. Light takes multiple paths shown in red and is collected at a single point in blue. b) an illustration of a random phasor sum. Individual independent phasors (red) are added to create a resultant phasor (blue). The figure is adapted from [150].

3.1.2 Generation of a speckle pattern

Suppose laser light is incident on a scattering medium as in Figure 3.2(a) whose scatterers have negligible absorption. Light may take multiple different paths through the medium and for the sake of this demonstration recombine at a single point highlighted in blue. Here, each scattering event randomises the phase and amplitude of the light [151] and on multiple scattering events, the output signal at this point in space-time is represented as a phasor sum of N scattering events. In Figure 3.2(b), I draw an example phasor diagram that illustrates this addition of multiple phasor components, which is what is perceived in the blue spot in (a). In this sense, multiple light scattering may be thought of as a random walk over the complex plane. Lastly, interference is described by path differences between the phasors or consecutive scattering events. Constructive interference is maximal for phase differences of 0° and minimal for path differences of 180°. Thus, a speckle captured by a camera would see a very granular pattern of randomly spaced bright and dark spots.

3.1.3 Dynamic Speckle

The previous description of the speckle as a random phasor sum holds for a single speckle in space and time. However, DCS studies the temporal decorrelation of a speckle pattern and we, therefore, also require a mathematical description of how a time-varying speckle can be made. With this in place, it is then possible to simulate speckle series and test DCS methods on synthetic data. In our case, we model a dynamic medium undergoing Brownian motion and simulate light scattering within that medium using the coupled dipole

approximation (CDA) [152–155]. CDA is a good model choice here as it may generate a speckle pattern in relation to how the scattering medium is defined. For example, if we model the scatterers in the medium to move over time, then the speckle pattern generated by CDA will also move over time.

A scattering medium with scatterer coordinates $\mathbf{r}$ that undergoes Brownian motion, may be described by the following equation,

$$\mathbf{r}_{i,j,k} = \mathbf{r}_{i-1,j-1,k-1} + \sqrt{2D\Delta t}w_{i,j,k}, \tag{3.13}$$

where D is a diffusion constant, Δt is a time step smaller than the characteristic timescale of the Brownian motion, and $w_{i,j,k}$ is a pseudorandom number [156].

In essence, CDA models each scatterer in a bulk medium as a dipole that radiates its own electric field on excitation by an incident field. Whilst the phasor approach in the previous section is independent of the scattering medium, the CDA approach physically models light scattering with respect to scattering medium parameters. Using the CDA, the output speckle generated by illuminating a random and dynamic volume of scatterers with a plane wave may be calculated. I restrict the study to simple scattering media for simulations later used in this thesis. For example, the polarisability of the scatterers, which describes how electric dipoles in a sample medium align when subjected to an external field, can be arbitrary. Here, I am only interested in temporal correlations in scattered light, so for simplicity, the only conditions I set on the scattering medium are that it be dynamic, defined above in Equation 3.13, and its scatterers randomly distributed.

To model light scattering in a dynamic medium using CDA, we will need to consider the light incident on a scattering medium, the distribution of scatterers, and the interaction of all scatterer dipole pairs. First, we consider a monochromatic laser source and that the polarisability of the scatterers is constant. The choice of scatterer polarisability is arbitrary. It describes how a dipole's moment of a scatterer is influenced by an external field. For simplicity, we set the polarisability to a constant. We then specify that the laser excites the scatterers at their resonance frequency $\omega = \omega_0$. For example, we do not consider Brillouin shifts in the frequency of scattered light. The following equation then describes the polarisability, which under the above assumptions depends on the resonant light's wavenumber, k_0,

$$\alpha(\omega)\big|_{\omega\to\omega_0} \sim -\frac{2\pi\mathcal{L}}{k_0^3(\omega-\omega_0+i\mathcal{L}/2)} = -\frac{4\pi}{ik_0^3}. \tag{3.14}$$

Here, $\mathcal{L}$ is the laser linewidth.

As a side note, the scattering cross-section and mean free path may be derived from the

above. The scattering cross-section is the probability that a scattering event may occur between the light and scattering medium and is dependent again on the light's wavenumber and polarisability,

$$\sigma(\omega) = \frac{k_0^4 |\alpha(\omega)|^2}{4\pi} = \frac{4\pi}{k_0^2}. \tag{3.15}$$

The mean free path is the mean distance light travels before its intensity is attenuated by $1/e$. It will be dependent on the density of scatterers ρ_s and σ and may be defined as,

$$\ell = \frac{1}{\rho_s \sigma} = \frac{V k_0^2}{4\pi N_s}, \tag{3.16}$$

Here, V is the volume of the scattering medium, and N_s is the number of scatterers. The optical depth is then the ratio L/ℓ, for the scattering medium thickness L. It may be thought of as the number of mean free paths that light takes to pass through the material.

We may consider the incident light as a vertically polarised plane wave moving from left to right along x,

$$E_0(x) = \exp\left[-ik_0 x\right]. \tag{3.17}$$

Next, we can define an expression for the field at a scatterer m. The theory of CDA states that this field E_m will be a sum of the incident field and the field generated by all its neighbours,

$$E_m = E_0(r_m) + \alpha(\omega) k_0^2 \sum_{n=1, n\neq m}^{N_s} G_0(k_0 |\mathbf{r}_n - \mathbf{r}_m|) E_n. \tag{3.18}$$

Here, we make use of the free-space Green's function, which describes the field that each scatterer m creates over all space,

$$G_0(\mathbf{r}_0, \mathbf{r}) = -\frac{\exp\left[ik_0 |\mathbf{r}_0 - \mathbf{r}|\right]}{4\pi |\mathbf{r}_0 - \mathbf{r}|}. \tag{3.19}$$

The field E_m at each scatterer is as a combination of the field that the incident wave creates at its position $E_0(\mathbf{r}_m)$ and the fields contributed to it by all other scatterers.

For a vector or unknown fields, $\epsilon = E_1, ..., E_n, ..., E_{N_s}$, the above formula can be set in matrix notation and computationally solved for ϵ by inverting G_0. In matrix format, this may be written,

$$-\epsilon_0 = \alpha(\omega) k_0^2 (\mathcal{G}_0 - \mathbb{I})\epsilon, \tag{3.20}$$

where $\mathcal{G}_{0,jk} = G_0(k_0 |\mathbf{r}_j - \mathbf{r}_k|)$. Once ϵ has been calculated, the field at any point in space

can be recreated through,

$$E(\mathbf{r}) = E_0(\mathbf{r}) + \alpha(\omega)k_0^2 \sum_{k=1}^{N_s} G_0(k_0|\mathbf{r} - \mathbf{r}_k|)E_k, \tag{3.21}$$

from which the speckle intensity can be found by $|E(\mathbf{r})|^2$.

The above treatment is purely to simulate how a dynamic speckle is made by light scattering off a scattering medium undergoing Brownian motion. I include it here to give a mathematical picture of how light scatters through a dynamic medium, but it is more formally used later in Chapter 6 to create synthetic dynamic speckle data, which are used to train a deep convolutional neural network and improve the speed of DCS measurements. The above description is a simplified version of light scattering. In reality, many biological media are heterogeneous and birefringent. In those cases, which are beyond the scope of the simulations used in this thesis, one may want to consider the polarisability or other properties of the scatterers. Python modules like Macromax [157, 158] are better suited in those cases.

3.2 Setups for Diffuse Correlation Spectroscopy

DCS setups are simple in nature. Their requirements are typically not hard to meet by today's technological standards. For example, to perform a DCS experiment, the main prerequisites are a laser source with a long coherence length (e.g. 10 m) and a scientific camera. Otherwise, the camera's exposure time is another experimental parameter, but the needed exposure time completely depends on the application. DCS is currently popular for blood flow measurements, in which case a fast-frame-rate camera, such as a SPAD camera, must be used to capture fast changes in speckle intensity emanating from a sample. In other cases, such as my own, where one is more interested in slower dynamics, scientific CMOS cameras are cheaper and often have excellent spatial resolution.

Figure 3.3 illustrates two types of DCS sensing setups. A typical DCS setup is portrayed in (a), where a laser source is focused into a small spot on the surface of the sample scattering medium. Two speckles patterns are generated, which traverse outwards over space and can be detected with a camera: one in transmission and one in reflection, Raster scanning over the sample can produce an image.

Figure 3.3(b) shows a simplified version of our DCS imaging apparatus. Suppose a sample is heterogeneous and has some features of differing dynamics or differing stiffness. I use a smiley face to represent this heterogeneity in the aforementioned figure. Information about these features can be obtained from the reflected speckle by flood-illuminating the

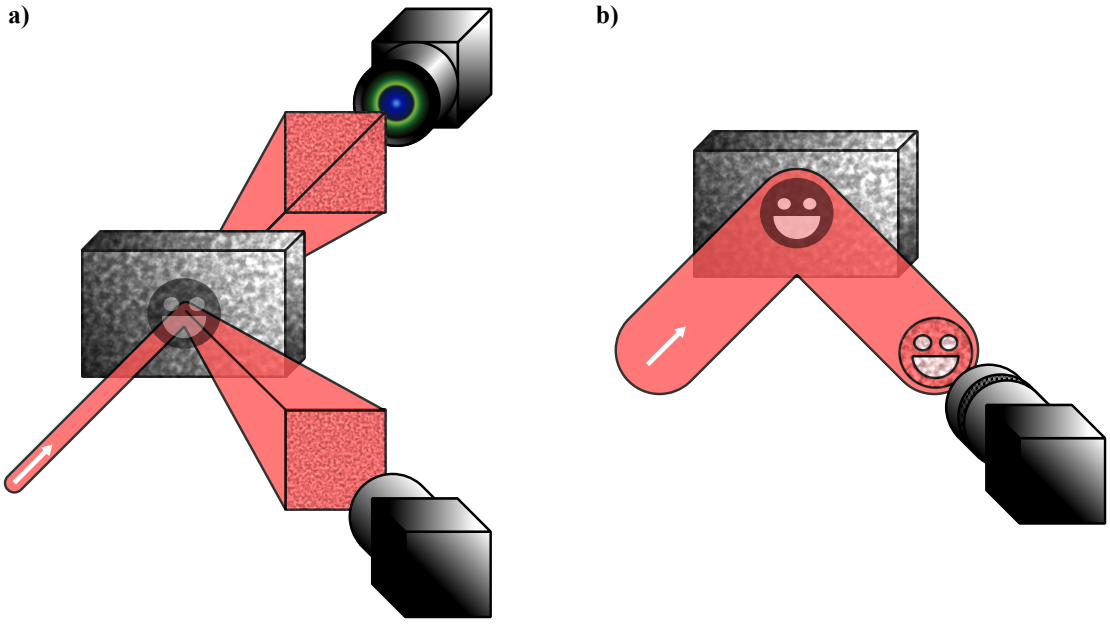

Figure 3.3: **Example DCS Setups.** a) A far-field DCS setup. Two configurations are shown: A laser is focused onto a small spot on the sample and a speckle can be captured either in transmission or reflection. The sample's features, such as the smiley face, can be imaged by raster scanning. b) An imaging DCS setup in reflection. A feature in the medium is flood-illuminated and its surface speckle is imaged with a camera objective.

sample with laser light and imaging its surface with a lens or camera objective. This setup is very similar to LSCI approaches, however, I have not seen it used for DCS in the past.

3.3 The g_2 Autocorrelation Function and the Speckle Decorrelation Time

DCS is a computational technique that relies on speckle dynamics and the g_2 autocorrelation function, which analyses the temporal component of the speckle. The g_2 function is quite widespread in optics and imaging and is often used in coincidence experiments in quantum imaging [159–161]. DCS, however, is a classical application of the g_2 function and is used to analyse the pixel intensity time series of a speckle pattern. In this case, the relaxation time of the speckle, otherwise known as the speckle decorrelation time and given the symbol τ_c, is studied by computing an autocorrelation of the speckle's pixel intensity time series. This relaxation time is related to the mean square displacement of the particles in the scattering medium [69]. Put simply, minuscule movements of scatterers are able to be detected macroscopically in the speckle pattern using the g_2 function.

3.3.1 The g_2 Autocorrelation Function

In this next part, I demonstrate how DCS measurements would usually be done. To create an example speckle pattern series, I use a Thorlabs 120 GRIT diffuser and a red 633 nm laser (RPMC RO633) under a transmission scheme. This is akin to the setup in Figure 3.3(a).

The laser light scatters through the diffuser. Since the diffuser is rigid and static, its speckle is also static. Therefore, I translate the diffuser along one direction to simulate a dynamic speckle. This was done at a speed of 10 μms^{-1} for a 1 mm diameter laser spot. For these sensing measurements, the speckle size is usually set to 1 speckle per pixel so that each pixel consists of an independent speckle mode [78, 80]. An example speckle pattern series for this diffuser measurement is shown in Figure 3.4(a).

Each pixel's intensity fluctuates over time and is denoted $I(t)$. Now consider a copy of a pixel time series lagged by τ represented by $I(t+\tau)$. These two time series are portrayed in Fig. 3.4(b). The original and lagged time series are the core elements needed for the g_2 function, which is written,

$$g_2(\tau) = \frac{\langle I(t)I(t+\tau)\rangle}{\langle I(t)\rangle^2}. \tag{3.22}$$

Here, angle brackets denote mean over time. In summary, the g_2 calculates the overlap between an intensity time series and a lagged version of itself. The mean intensity of the times series squared then normalises it.

The naive way of calculating the g_2 function is to iterate through τ and perform element-wise multiplication between the original time series and its lagged copy and normalise that product by the square of the mean intensity time series. However, this is very inefficient for long time series due to its iterative process, in which case, more efficient computation of the g_2 function may be coded as a fast Fourier transform (FFT) through the Wiener-Khinchin (autocorrelation) theorem [149, 162]. Here, the g_2 autocorrelation function and the speckle's spectral density, $\mathcal{F}\{I(t)\}$, form a Fourier transform pair.

$$\begin{aligned} g_2(\tau) &= \frac{\frac{1}{T}\int_0^T I(t)I(t+\tau)dt}{\left[\frac{1}{T}\int_0^T I(t)dt\right]^2} \\ &= \frac{\mathcal{F}^{-1}\Big\{|\mathcal{F}\{I(t)\}|^2\Big\}}{\frac{1}{T}\left[\int_0^T I(t)dt\right]^2}. \end{aligned} \tag{3.23}$$

Now, rather than performing a dot product on each iteration, we express the numerator's integral as the more efficient computation of taking the inverse Fourier transform of the squared frequency spectrum.

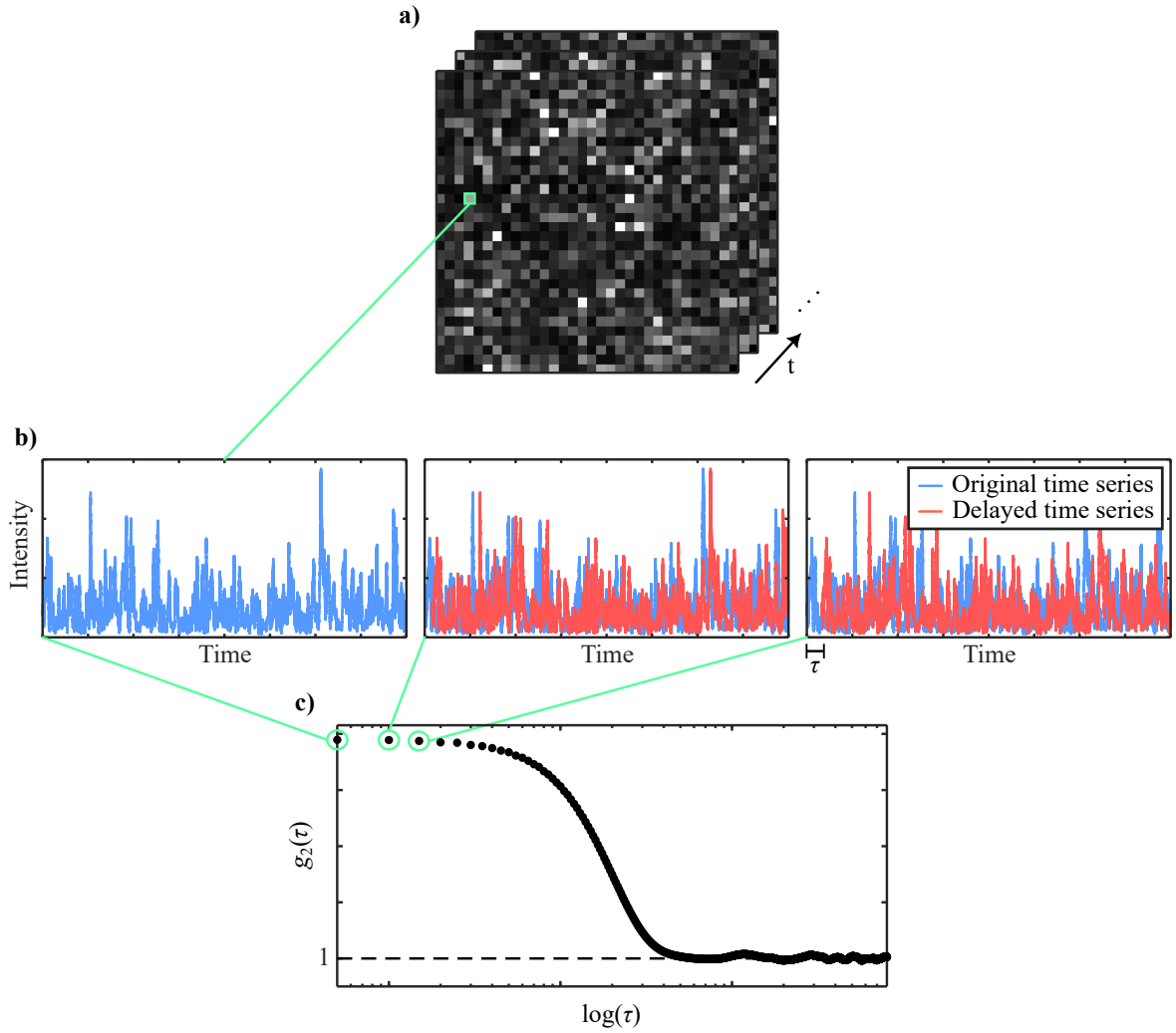

Figure 3.4: **Calculating the $g_2(\tau)$ trace.** a) A speckle pattern with a speckle size of 1 speckle per pixel. b) Three plots depicting $I(t)$ in blue and $I(t+\tau)$ in red for different time lags. A green arrow from (a) to (b) indicates this time series is from a single pixel of the speckle. c) The resulting g_2 curve is calculated by performing an autocorrelation of the blue and red time series for increasing τ. Green arrows from (b) indicate what value of τ produces what point in the g_2 curve.

Performing the g_2 computation on the above time series yields the g_2 curve depicted in Fig. 3.4(c). The curve decays exponentially until fully uncorrelated at $g_2(\infty) = 1$. To show this, assume that we have a stationary intensity time series. Since the time series is stationary, the mean of the time series should not change over time and $\langle I(t)\rangle$ and $\langle I(t+\tau)\rangle$ will be equal. Since the time series in question contains intensity measurements, its values will also always ≥ 0. Then, if we assume that $I(t)$ and $I(t+\tau)$ are uncorrelated for large τ, then they are also statistically independent [163]. In this case, the top part of the g_2 function is reduced according to $\langle I(t)I(t+\tau)\rangle = \langle I(t)\rangle\langle I(t+\tau)\rangle$. Therefore, for

uncorrelated signals and large time lags, the g_2 function is also reduced according to,

$$g_2(\tau >> \tau_c) = \frac{\langle I(t)\rangle^2}{\langle I(t)\rangle^2} = 1. \tag{3.24}$$

3.3.2 Methods for Finding the Speckle Decorrelation Time, τ_c

As previously discussed in Chapter 2, τ_c is correlated with tissue stiffness. It is therefore imperative for DCS tissue measurements that τ_c is accurately estimated. In this chapter, we have introduced two different DCS setups: a sensing setup and an imaging setup, where there are compromises in computational speed depending on which DCS format is chosen. In the sensing DCS format, one measures a speckle pattern in the far field and may fit an exponential curve to a mean g_2 curve from the speckle pattern. This has been shown to improve the SNR of the g_2 curve and the accuracy of the τ_c estimation [80, 81]. This fitting approach, however, is very slow for the imaging DCS format as one needs to find the τ_c for each pixel. Instead, a faster approach at the cost of accuracy would be to find the closest corresponding frame to the $1/e$ value of each g_2 curve by an indexing method. Of course, for the above g_2 curve, which decays to 1 instead of 0, we determine τ_c at the $(g_2(0) - 1)/e)$ value.

Figure 3.5 illustrates the two methods for finding τ_c. The above g_2 curve from Figure 3.4 is shown again in (a). The quickest way to find τ_c is to use an indexing approach, which is shown in (b). Here, one can implement the below finding algorithm to estimate τ_c,

$$\tau_c = \underset{\tau}{\operatorname{argmin}} \Big| g_2(\tau) - \Big[1 + \frac{(g_2(0) - 1)}{e}\Big] \Big|. \tag{3.25}$$

I label this the 'indexing' approach since it uses an argmin function to find the closest time point that coincides with τ_c. This approach is fast, but the accuracy in its output τ_c depends on the sampling rate of the intensity time series since it finds the closest time point to the $1/e$ value. This approach would be well suited to real-time DCS applications given a high frame rate camera is used. I use this approach for the imaging application discussed in Chapter 5.

Other than the indexing approach detailed above, a fitting approach may be used to determine τ_c, which is slower but gives some advantages over the indexing approach depending on the intended application of the DCS experiment. Firstly, the fitting approach may determine τ_c with more accuracy since it is less constrained by the sampling rate of the time series. But, another more subtle effect of the fitting approach is that it provides information on the type of media being probed. In this case, different fits have been used to determine the type of particle motion in a medium. Specifically, a diffusive medium,

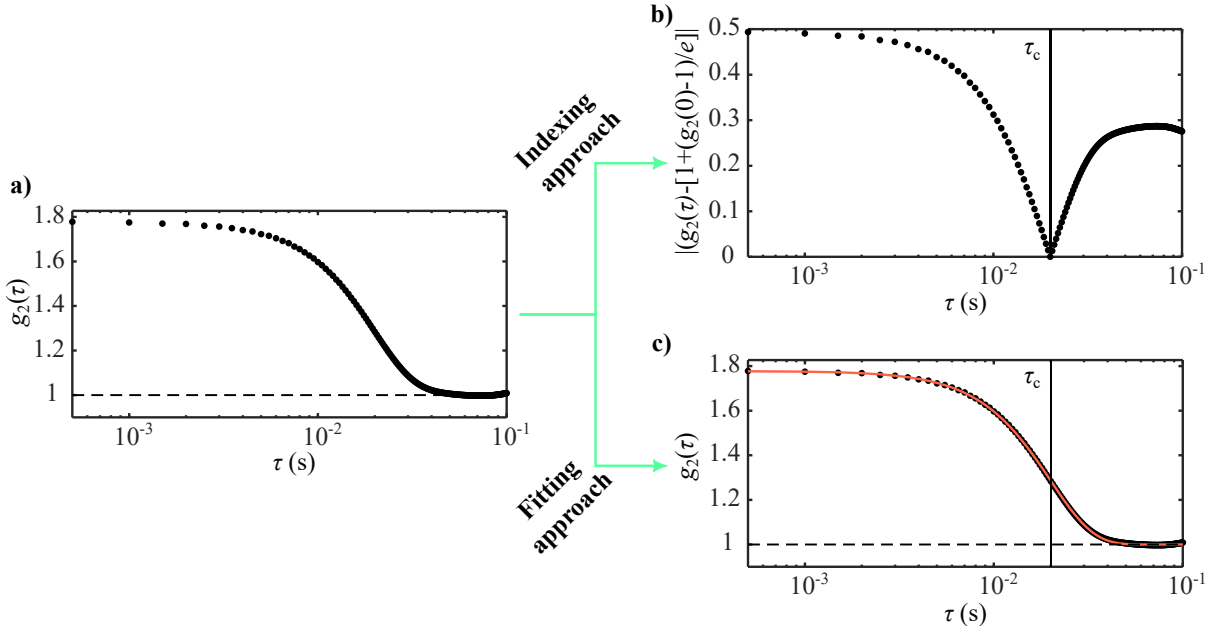

Figure 3.5: **A Flow Diagram of Methods for finding τ_c.** A g_2 curve is shown in (a). Green arrows point towards the two different τ_c finding methods. b) shows the 'indexing' approach, which transforms the g_2 curve with an abs function and then uses an argmin function to determine the minimum of the transformed g_2 curve and thus also the τ_c value. c) shows the g_2 curve and fit (red solid line). Vertical lines in both (b) and (c) show were each approach respectively estimated τ_c.

whose scatterers undergo Brownian motion, may be described by the following decaying exponential fit,

$$g_2(\tau) = 1 + \beta\left[\left(\frac{\tau}{\tau_c}\right)\right]. \tag{3.26}$$

Additionally, a ballistic medium, which undergoes random flow (movement predominantly in one direction) may be described by,

$$g_2(\tau) = 1 + \beta\left[\left(\frac{\tau}{\tau_c}\right)^2\right], \tag{3.27}$$

which differs from the above diffusive medium fit by a power term equal to 2. In both cases, the power term originates from the mean-squared displacement of scatterers [74, 80, 82].

β is a coherence term and is equal to $g_2(0) - 1$. It is linked to the speckle contrast like

so,

$$\begin{aligned} K &= \frac{\sigma}{\langle I(t)\rangle} \\ &= \frac{\sqrt{\langle I(t)^2\rangle - \langle I(t)\rangle^2}}{\langle I(t)\rangle} \\ &= \sqrt{\frac{\langle I(t)^2\rangle}{\langle I(t)\rangle^2} - 1} \\ &= \sqrt{g_2(0) - 1} \\ &= \sqrt{\beta}. \end{aligned} \tag{3.28}$$

A better fit can be obtained by maximising β, which can be achieved, for example, by increasing the acquisition time of the experiment or the number of samples fed into the g_2 function [164]. The g_2 fit above is shown in Figure 3.5(c). In this example, where a diffuser was translated along a single direction, the ballistic medium g_2 fit was used, indicative of a random flow medium, such as blood flow [80].

In other cases, the g_2 curve is not well fitted with the above diffusive and ballistic medium fits. For example, biological media are often heterogeneous and composed of scatterers that move according to different time scales and their g_2 curve is better fit by an exponential with multiple decorrelation time components. For example, the below multi-exponential fit may be more applicable,

$$g_2(\tau) = 1 + \beta\big[\rho_1|\exp(-\tau/\tau_1)| + \rho_2|\exp(-\tau/\tau_2)| + (1 - \rho_1 - \rho_2)\big]. \tag{3.29}$$

Here, ρ_1 and ρ_2 represent the fraction of slow and fast moving scatterers respectively. The fit splits τ_c into both a fast τ_1, a slow τ_2 component, and also incorporates a static $(1 - \rho_1 - \rho_2)$ component. A good example of this fit being used in practice is [105], who probe blood flow with τ_1 but intracellular motility with τ_2. More generally, however, τ_1 could be used to account for experimental noise such as apparatus vibration. In these cases, the magnitude of ρ_1 and ρ_2 give indication into the significance of the τ_1 and τ_2 parameters. In Chapter 4 we used the above multi-exponential fit for assessing neurodegeneration in mouse brain samples.

3.4 Pixel Stacking: A Method to Reduce Acquisition Time Constraints of Diffuse Correlation Spectroscopy

I previously mentioned that the g_2 curve should decay to one when fully decorrelated. This is not true in some cases, however. We have seen experimentally that when the

acquisition time of the measurement is similar to the τ_c in question, then the g_2 trace's floor instead sits below one instead of at one, $g_2(\infty) < 1$. This has been linked to statistical undersampling of enough independent speckle modes [164, 165]. For example, the mean intensity (the denominator of Equation 3.22) has not been calculated over enough speckle modes. When the acquisition time is short, it can be more difficult to accurately determine τ_c, because one needs to account for the offset between the g_2 trace's floor and $g_2(\infty) = 1$. For example, using the fitting approach to find τ_c, a new 'offset' term must be provided in the fit, which is not always robust, especially when the tail of the g_2 trace is noisy. An offset term must also be provided for the indexing approach. For example, this term could be an average of the values in the g_2 trace's tail, but this is also not robust as it relies on the user now being able to accurately estimate the g_2 trace's floor to determine τ_c.

As different points in space have the same statistics, concatenating different pixel intensity time series can effectively increase the experiment's acquisition time. I will call this the 'pixel stacking' approach from here on out. Figures 3.6(a-b) provide an illustration of how the pixel stacking approach is implemented. Here, random pixels of the speckle pattern series are concatenated. In this example, I concatenate ten pixels atop one another. The resulting speckle pattern series, therefore, is ten times longer but has ten times fewer pixels. A single stacked pixel intensity time series is shown in (b) in red. In blue is a non-stacked intensity time series, which was acquired for 40 s.

(c-d) show the results of the pixel stacking procedure. In (c) are two mean g_2 traces, one of which is found by autocorrelation of the stacked time series in red and the other by autocorrelation of the original time series in blue. The g_2 curve calculated using the stacked time series has a floor at $g_2(\tau) = 1$, whereas the other curve dips below ~ 0.8. (d) plots τ_c against acquisition time for both the stacked and non-stacked schemes. Both schemes eventually flatten out at $\tau_c \sim 0.1$. A grey box represents a 5% deviation from this threshold τ_c. We have found empirically that as a general rule, to obtain τ_c that falls within a 5% deviation of the threshold τ_c, then one should set their acquisition time to roughly $100\tau_c$ for the non-stacked scheme or $10\tau_c$ for the pixel stacking scheme.

3.5 Effect of Multiple Speckles in a Single Pixel on g_2

It will be interesting to see how the speckle size influences the estimation of τ_c. For example, how would τ_c be affected if multiple speckles are sampled within one pixel? Here, different intensity time series would be mixed in that single pixel. We continue with the example 120 grit diffuser real data to test this hypothesis. In this configuration, we have a speckle pattern series of size 32×32 pixels, where each pixel's τ_c is around 0.1 s. We compare two measurement schemes: the first measurement scheme is the general approach

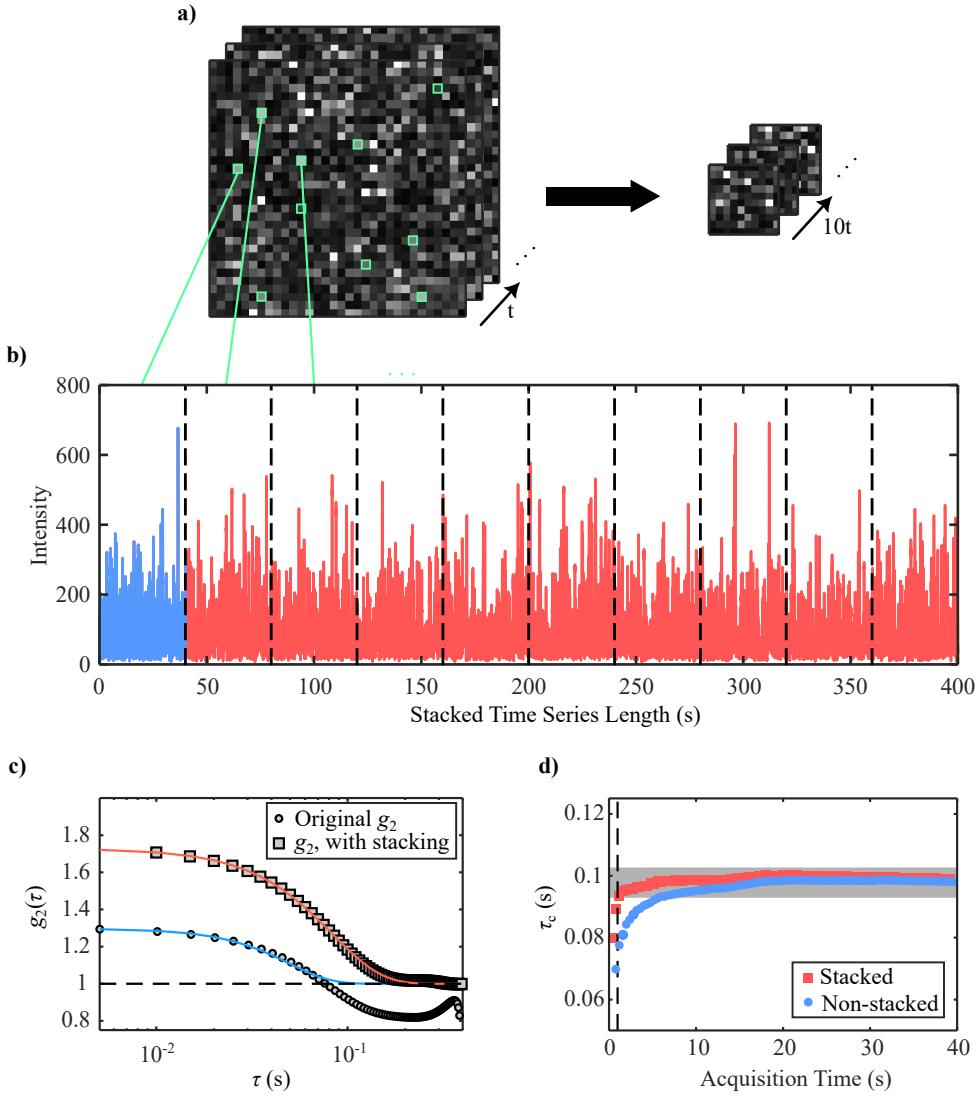

Figure 3.6: **Pixel Stacking for the DCS Sensing.** a) A flow diagram depicting the original speckle pattern series being transformed to a smaller pixel dimensions but longer time series stacked speckle. b) An example stacked intensity time series, where the time series in blue represents the length of a single pixel time series and a in red the stacked time series. Dashed vertical lines represent boundaries between the stacks. Green squares on (a) highlight random pixels chosen for stacking and green lines point to their respective time series in (b). c) Two example g_2 curves: circular makers for the g_2 operation on the original speckle and square markers for the stacked speckle. Here, g_2 curve computed from the original speckle dips below $g_2(\tau) = 1$ and has some noise in its tail. Since the fitting algorithm determines full decorrelation at $g_2(\tau) = 1$, the estimated τ_c is biased to shorter values. d) τ_c vs acquisition time plots for the stacked and non-stacked cases. A vertical dashed line indicates an acquisition time of $10\tau_c$, and a horizontal grey border illustrates a five per cent error of the threshold τ_c (determined when the non-stacked curve flattens out). Here, we see that the stacked (red) curve sits within the five per cent error margin for an acquisition time of $10\tau_c$ as opposed to the non-stacked (blue) curve, which required an acquisition time equivalent to $100\tau_c$.

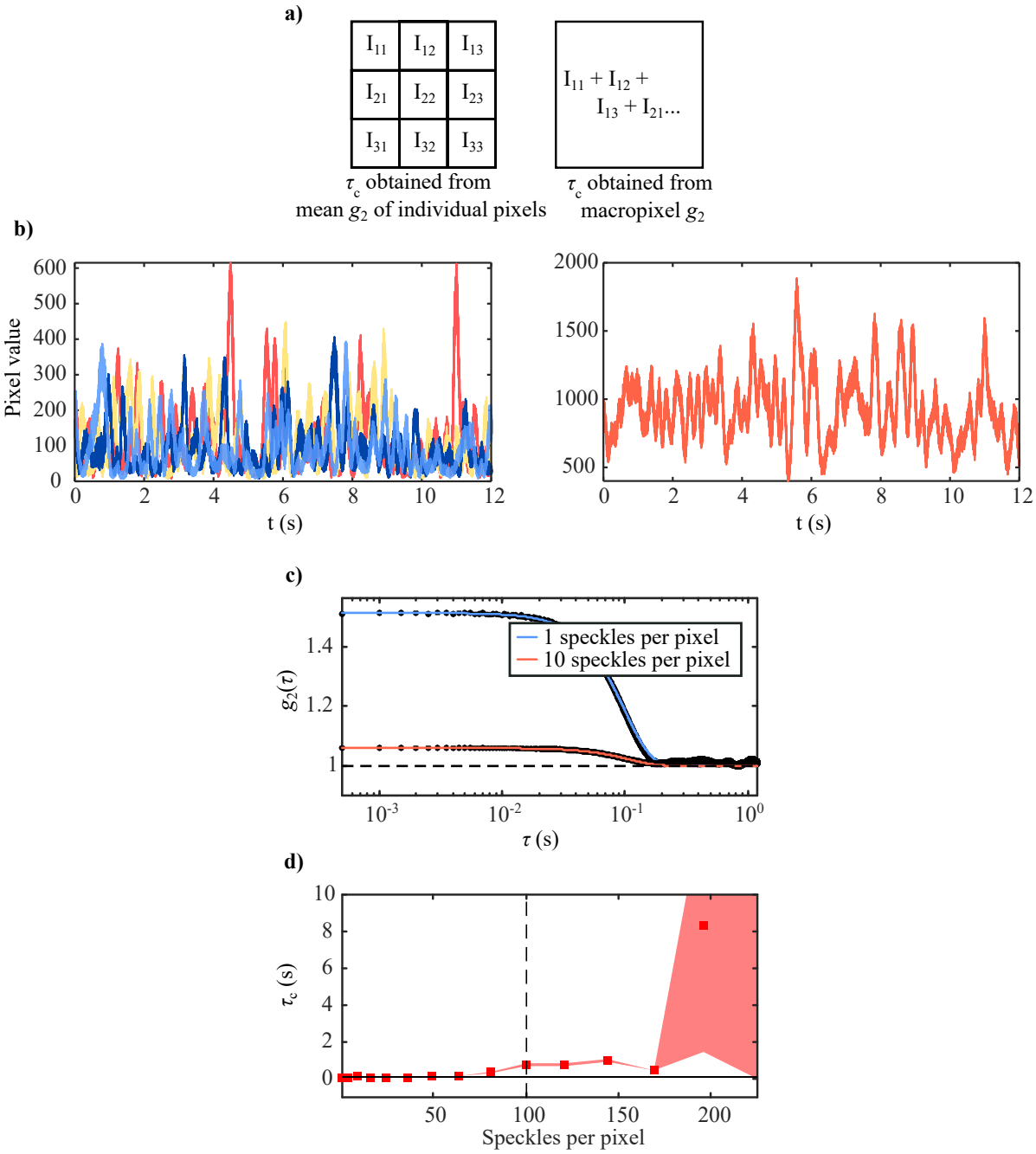

Figure 3.7: **τ_c analysis for speckles smaller than a pixel.** a) Two measurement schemes are shown: On the left, there is an array of nine pixels, each with an intensity time series that decorrelates to give $\tau_c \sim 0.1$ s. On the right is a macropixel, which is a sum of all the intensity time series of the nine-pixel array on the left. b) Intensity time series for the individual pixels of the first measurement scheme (left) and a single summed intensity time series of the macropixel in the second measurement scheme (right). c) Example g_2 curves of the second measurement scheme in (a). With more speckles contained in a single pixel, the contrast is decreased, and the exponential is more difficult to fit. d) A plot of τ_c vs speckle size for the macropixel scheme. A solid black horizontal line shows the true τ_c value. A vertical dashed reference line is placed at $x = 100$ speckles per pixel and highlights where the curve begins to deviate from the true τ_c value. Red patches represent 95% confidence intervals of the g_2 fit.

to g_2 measurements, where one speckle is sampled per pixel. The second measurement scheme simulates a situation where there are many independent speckles contained within one pixel. To simulate the second scheme, we create a macropixel by summing many independent pixel time series together. The speckle size is thus one over the number of individual pixels in the macropixel. In the below example, we sample up to 200 speckles in a single pixel. These two measurement schemes are illustrated in Figure 3.7(a), and their respective intensity time series are shown in (b). g_2 curves for the macropixel scheme for two different speckle sizes are shown in (c). Here, we see visually that the g_2 curve of macropixel (size 10 speckles per pixel) decays on the same time scale as the 1 speckle per pixel trace but suffers from lower contrast, i.e., $\beta_{9\text{ pixels}} < \beta_{1\text{ pixel}}$. If the contrast becomes too poor, fitting an exponential to the data becomes difficult.

Results comparing τ_c against the speckle size are shown in Figure 3.7(d). The macropixel's τ_c agrees well with the true τ_c (determined at 1 speckle per pixel), and the DCS measurement is forgiving when setting the speckle size. DCS's ability to fit the g_2 curve becomes less robust with decreasing speckle size, and the τ_c estimation becomes less accurate.

3.6 Effect of a Multiple τ_c Components in a Single Speckle

In this section, we study how the g_2 may look if there are two differing τ_c components in a single speckle. In DCS experiments, one can change their camera frame rate, which may give them sensitivity to dynamics at different timescales. Here, we see how the camera frame rate effects the sensitivity of the DCS to time series with short and long τ_c.

In Figure 3.8(a), I have shown three different time series: a fast decorrelating series in red, a slow decorrelating series in blue and a combination of both series in green made simply by adding the above series together. Applying the g_2 function to the above series, we get the g_2 curves shown in Figure 3.8(b). The fast decorrelating series has $\tau_1 \sim 1$ s, and the slow series has $\tau_2 \sim 10$ s. However, the g_2 from the combined series features a double exponential decay, where each exponential bump aligns with the previous fast and slow g_2 curves. Imagine now that we have a slow-frame-rate camera whose frame rate is not quick enough to resolve the g_2 decorrelation curve of the fast component. Figure 3.8(c) models this case. Here, the g_2 curve of the slow decorrelating component is still found but with reduced contrast. Here, we have shown evidence through modelling that the slow decorrelating speckle component can still be resolved using a slow frame rate camera in the presence of a fast decorrelating speckle component.

To confirm that this treatment of simply adding two different speckle series is justified, we

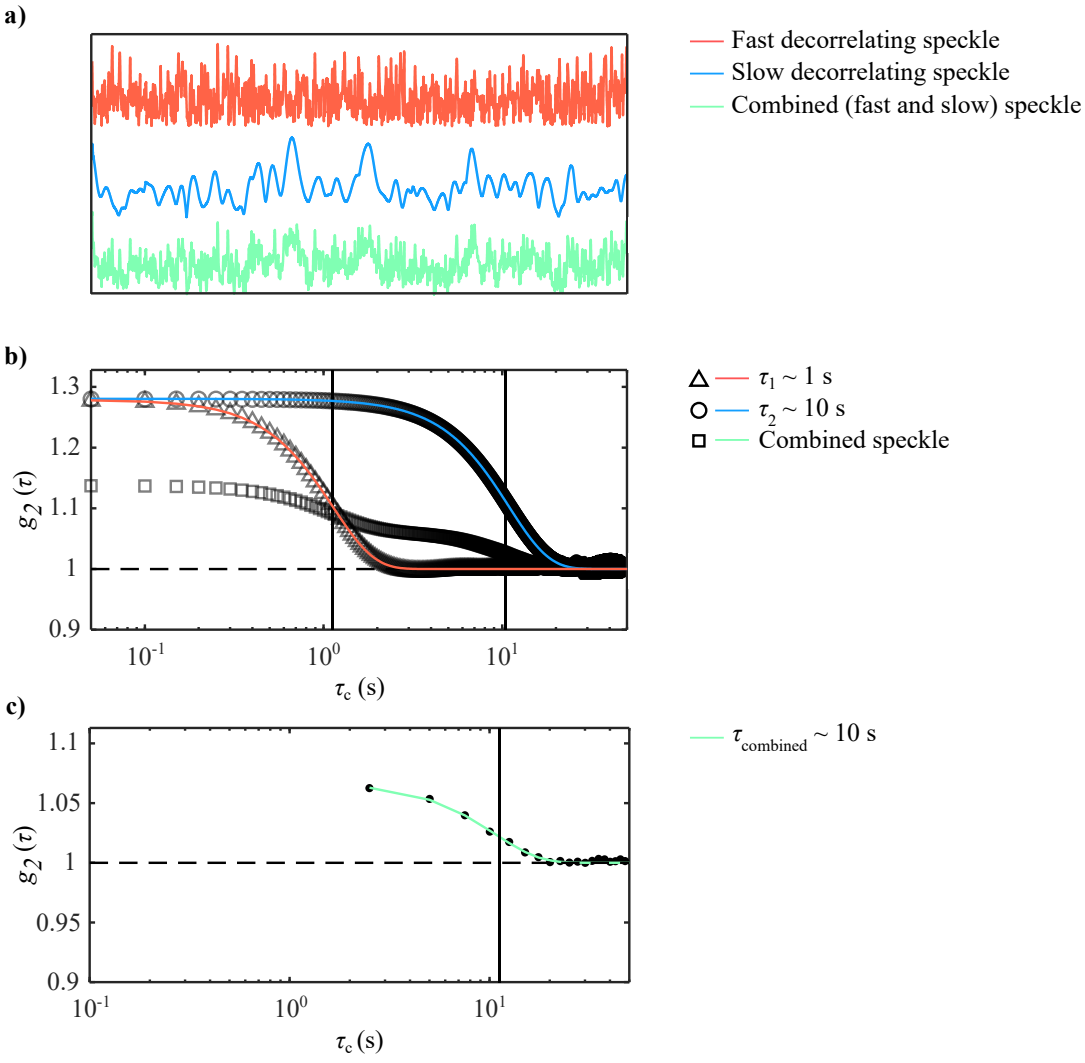

Figure 3.8: **Picking dynamics at different time scales using camera frame rate.** a) Three time series are shown. Red is a fast decorrelating time series, blue is a slower decorrelating time series, and green is a combined time series made by summing the two former time series. b) The corresponding g_2 curves for the above time series are shown. The g_2 curve of the combined time series features a double exponential decay. c) A g_2 curve calculated from the combined time series. The time series was binned every ten frames to simulate a slower camera frame rate of 200 fps. In doing so, the slow τ_2 is found.

see if the same signal is evident in real mouse brain data. This brain data is characteristic of the data later used in Chapter 4. In Figure 3.9(a), I show a g_2 curve of a mouse brain slice acquired at 2000 fps. A double exponential is also evident here. Figure 3.9(b) shows the spectra obtained from 2000 and 400 fps time series brain data. By acquiring at a lower frame rate, high-frequency components are attenuated. Thus, we have shown that multiple speckle decorrelation time components can be seen in real data, corroborating our above modelling scheme. This outcome suggests that one may be able to filter out fast dynamics in the g_2 by acquiring at a slower camera frame rate.

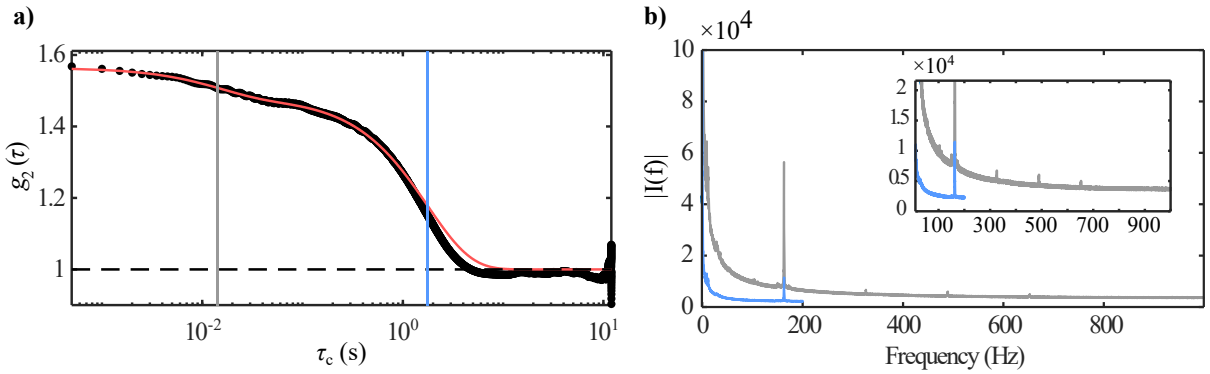

Figure 3.9: **Double exponential seen in g_2 of real data.** a) An example g_2 curve from the data set of the mouse neurodegeneration sensing project. The g_2 curve was calculated for 2000 fps time series data and features a double exponential. Grey and blue vertical lines signify the fast and slow decorrelation time components. b) Mean spectra of 2000 fps (grey) and 400 fps (blue) time series. High-frequency components are attenuated when the frame rate of the acquisition is decreased. The inset shows a zoomed-in version of the spectra.

3.7 Introducing a Surface Imaging Format for Diffuse Correlation Spectroscopy

In past studies, DCS has been primarily used for deep sensing applications, which look at blood flow changes in the body [78–81]. Otherwise, DCS has been used for rheology under the name of laser speckle rheology, primarily by Seemanti Nadkarni's group [86–92], who have related τ_c to a medium's complex modulus $|G|$ through shear rheology and optical measurements. In their case, images made up of τ_c or $|G|$ are made using a raster scanning approach rather than a single acquisition. Here, we present a novel approach that images the speckle pattern from a sample's surface and computes a pixel-wise τ_c.

Using now the setup depicted in Figure 3.3(b), we apply this technique to lamb brain samples and imaged the speckle reflected from its cerebellum over a two-minute period. A mean intensity image taken by averaging all the frames of the speckle is shown in Figure 3.10(a) and its corresponding DCS image in (b). This DCS image is composed by finding the pixel-wise τ_c for each pixel of the speckle. One can see that it is well correlated with the mean intensity image. However, on close inspection of the sides of both images, the DCS image appears to be more uniform, hinting that the τ_c in the DCS image is not dependent on the intensity of the pixels in the mean intensity image. The interesting takeaway here is that the DCS image provides different or additional information than the intensity image. For example, the spider-like pattern of white matter is known to be greater in stiffness than the surrounding grey matter [166–168] and in our image also has larger τ_c than the grey matter. In Chapter 5, we will explore applications of this DCS

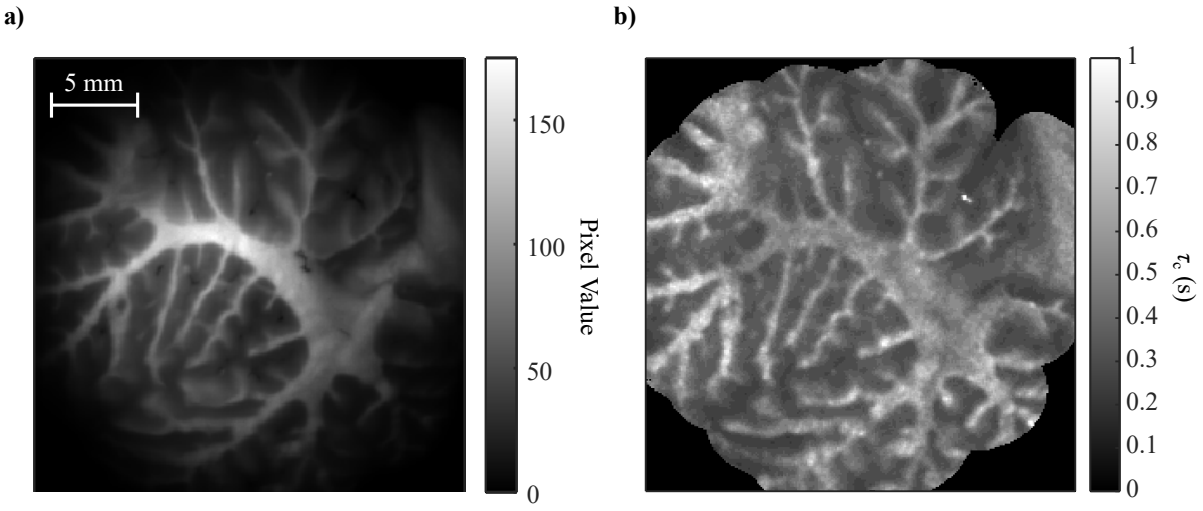

Figure 3.10: **An example DCS image.** a) A mean intensity image of a lamb brain cerebellum made by time averaging all the frames in a speckle pattern acquisition. b) The corresponding τ_c colour map of the brain cerebellum. The τ_c colour map is more uniform than the intensity image, indicating that the τ_c is not dependent on the intensity image but another aspect of the brain, such as its stiffness. Some pixels, e.g. at the corners of the image, did not return a τ_c and have been set to black to improve the image quality.

method for imaging tumours and bone.

3.8 Pixel Stacking for the DCS Imaging Approach

When performing the DCS imaging approach, the effect of short acquisition times on the measurement may not be as severe as that of the sensing approach. This is because one may only care about observing relative differences in τ_c in their sample, as opposed to obtaining an accurate τ_c of the sample. To illustrate this idea, I have drawn three DCS images in Figure 3.11: a two-minute acquisition in (a), a five-second acquisition in (b) and a one-second acquisition in (c). The two-minute acquisition clearly has the best contrast and resolution; however, the details of the white matter can still be visually differentiated from the grey matter in the five-second acquisition. However, in the one-second acquisition, the white matter can no longer be told apart from the grey matter.

In some cases, such as live imaging, it may be preferable to have a short an acquisition time as possible. Methods to speed up the acquisition, such as the pixel stacking procedure, are valuable in these cases. Speeding up the acquisition of DCS under the imaging scheme is trickier than the sensing approach. In the sensing approach, all the speckle modes have similar dynamics; each pixel has a similar τ_c. However, for the imaging approach, each pixel maps to a different region of the sample and a different τ_c. Thus, one should not stack pixels mapping to different sample regions and instead stack nearest neighbour pixel

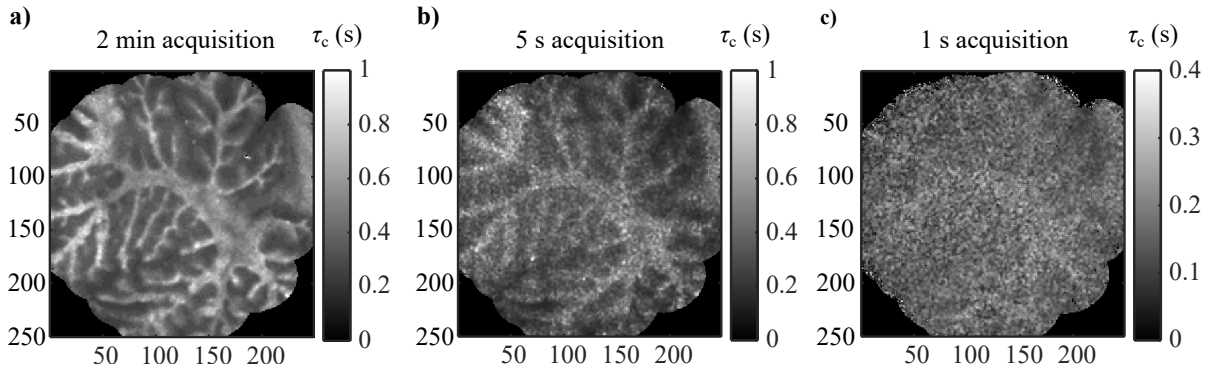

Figure 3.11: **DCS images at various acquisition times.** a) A lamb brain cerebellum DCS image from a two-minute speckle series acquisition. b) A DCS image for a 5 s acquisition. c) A DCS image for a 1 s acquisition. The cerebellum is no longer resolved here.

time series.

There are two ways to implement the nearest neighbour pixel stacking procedure. In both approaches, the time series of a pixel is concatenated with the time series of its neighbouring pixels to effectively extend the acquisition time. However, in the first method, the time series of adjacent pixels are concatenated sequentially after the selected pixel's series, whereas, in the second method, the adjacent pixels' series are first copied and concatenated onto it. Consequently, the first method reduces the spatial resolution, while the second method preserves it. To preserve the spatial resolution, copies of pixel time series need to be made, which consequently increases the size of the speckle series and thus the computational time of the g_2. From here on out, the second method will be referred to as the conserved pixel stacking approach. For the second method, the resulting speckle series is larger than the original and is more computationally demanding to process with the g_2 function, so it is not always ideal to use. For example, for a 3×3 pixel neighbourhood, the number of frames in the new speckle will be nine times more than the original speckle, but the pixel dimensions will also be conserved.

The comparison of these two methods is outlined in Figure 3.12. A speckle of the lamb brain cerebellum is shown in (a), and a stacked intensity time series of a single pixel is shown in (b). (c-d) represent results from the two-pixel stacking schemes for speckles acquired for one second in duration. The image dimensions are reduced in (c) but are conserved in (d). The distinction between grey and white matter can be made in (c), although the resolution of the image makes it harder to do so. Otherwise, in (d), the DCS image is noisy, but the contrast between white and grey matter is greatly improved from the previous non-stacked DCS image shown in Figure 3.11(c).

Lastly, one artefact arises from using the pixel stacking approach, which can be seen in

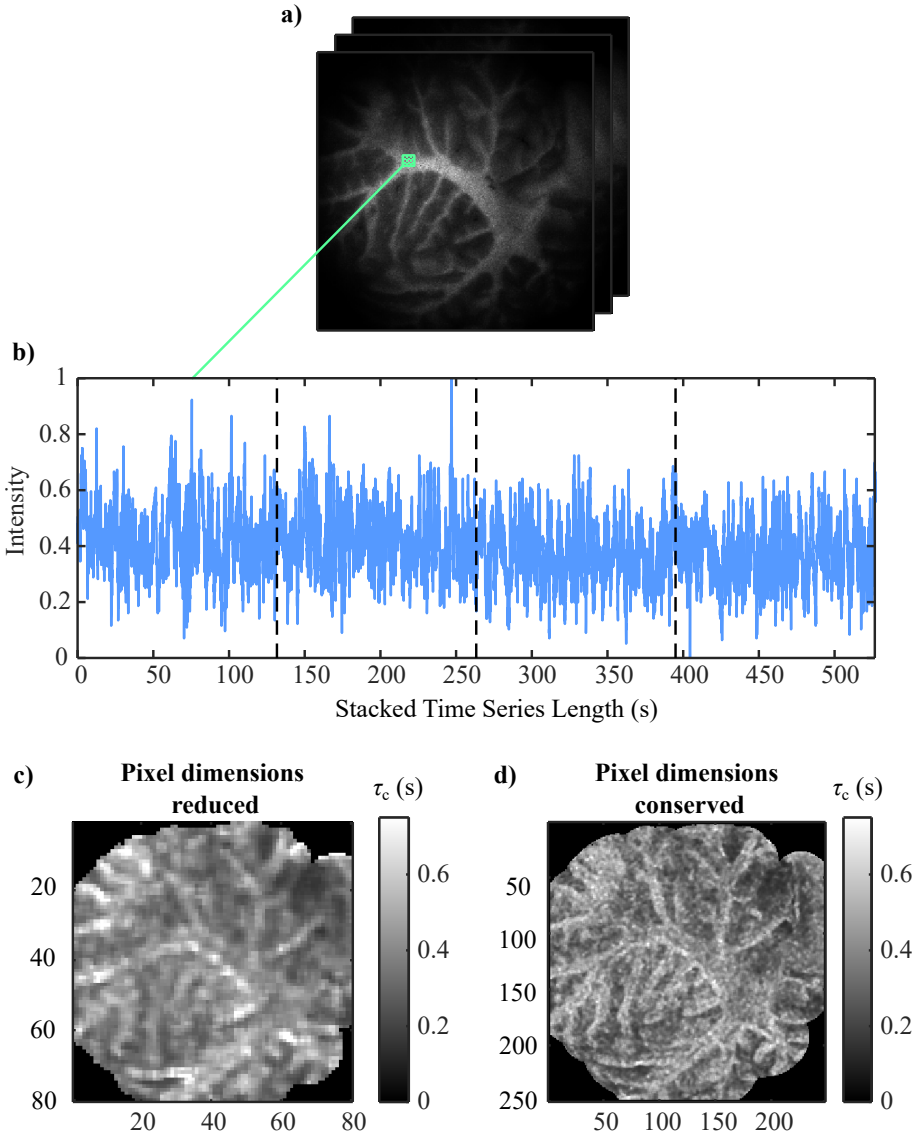

Figure 3.12: **The DCS imaging approach with pixel stacking.** a) A speckle pattern series of the lamb brain cerebellum. b) A stacked intensity time series made by stacking nearest neighbour pixels shown in the the green ROI. Dashed vertical lines represent ordinates where a new stack begins. The stacked time series is cropped in the x-axis at four stacks. c) A macropixel DCS image made from nearest neighbour pixel stacking regions of 3×3 pixels. The DCS image dimensions are smaller than the original speckle series dimensions here. d) Another DCS image; this time, the x-y dimensions are the same size as the original speckle images. This approach is more computationally demanding. For both (c-d) the acquisition time was 1 s in duration.

the borders between the white and grey matter. In this case, the pixel stacking method combines time series with different mean intensities (e.g. a darker pixel with a lighter pixel). This is evident in the stacked intensity time series, as an abrupt change in intensity that every time the pixels are stacked. The g_2 perceives this boundary artefact as a long decorrelating component and estimates a higher τ_c value. A seemingly obvious solution to

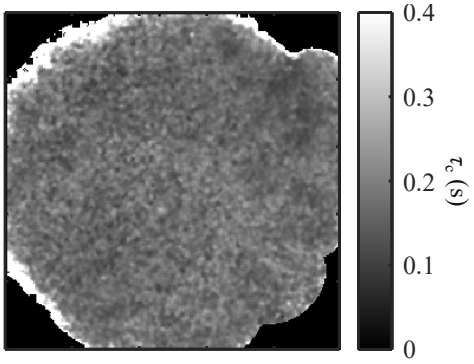

Figure 3.13: **The effect of normalising time series before applying pixel stacking.** Time series were first centred and standardised before being nearest neighbour concatenated. The resulting DCS image now has no contrast between the white and grey matter regions of the brain.

match the mean intensities of white and grey matter pixel regions would be to standardise the time series before applying the stacking procedure. However, this removes the benefits of the pixel stacking procedure in the first place, as shown in Figure 3.13. This is perhaps because normalising averages out the differences in the dynamics of each time series. Thus, this artefact is persistent and cannot be removed by standardisation/normalising the pixels prior to stacking.

3.9 Mechanorheology: Mechanical Ground Truth Measurements for DCS

To finish this technical background chapter, we need to change track slightly away from DCS. My work in this thesis mainly involves developing an optical technique for inferring mechanical characteristics of tissue, such as stiffness. As such, mechanobiology measurements were also required for the above DCS sensing and imaging schemes. Measurements performed with a nanoindenter (Optics11 Life Chiaro) by Giuseppe Ciccone and Matthew Walker formed the basis of corresponding ground truth measurements to the DCS measurements.

Our collaborators have published a thorough tutorial and discussion of the workings of the nanoindenter [169]. I also use snapshots from their work to explain how the nanoindenter is operated here in my Figure 3.14. Simply put, a nanoindenter is a cheaper and less complicated alternative to an AFM and may achieve down to sub-nN resolution as opposed to an AFM's sub-pN resolution. It has been proven effective in a number of applications where the use of an AFM is unnecessary, for example, on macroscale samples [170–176].

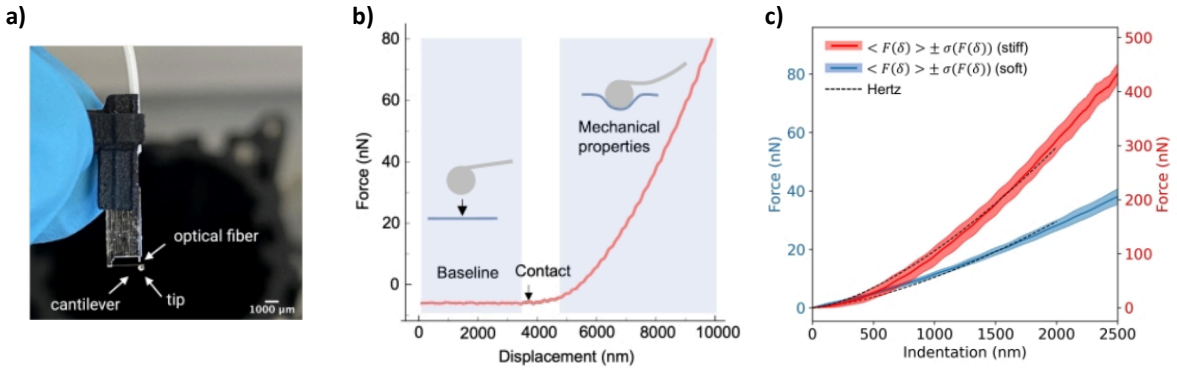

Figure 3.14: **The Chiaro nanoindenter.** a) A photograph showing a nanoindenter probe, cantilever and optical fibre. This probe may be indented into samples, and their stiffness measured with respect to the bending of the cantilever. b) A force-displacement curve for a successful nanoindentation measurement. Two insets show the probe position (out-of-contact and in-contact with the sample) corresponding to different regions of the force-displacement curve. c) Two example force-indentation curves for a stiff and a soft material. A Hertz contact mechanics model is also fitted to both curves. Solid red and blue lines represent mean values and shaded regions represent one standard deviation. Figures taken from [169].

The fundamental component of a nanoindenter is a probe resting on a cantilever that is linked to an interferometer by an optical fibre. An example nanoindenter probe for the Chiaro is shown in Figure 3.14(a). The probe is moved at a constant speed and indented into a sample, causing the cantilever to bend, and the degree at which the cantilever bends is measured optically by means of an optical fibre and an interferometer. Under this operation, the nanoindenter retrieves force-distance or force-indentation curves for a sample, and to further obtain a sample's Young's modulus, E, a contact mechanics model may be fit to force-indentation curve, such as the Hertz contact model typically used for viscoelastic materials [177] defined below as

$$F = \frac{4}{3}\frac{E}{(1-\nu^2)}\delta^{\frac{3}{2}}R^{\frac{1}{2}}. \tag{3.30}$$

Here, F is the force applied to the sample, δ is the indentation, R is the probe radius and ν is the Poisson ratio, which describes how a material expands or contracts during loading. For soft materials, $\nu \sim 0.5$ [178, 179]. Otherwise, if the ν is not known, then the Hertz model is reduced to

$$F = \frac{4}{3}E_{\text{effective}}\delta^{\frac{3}{2}}R^{\frac{1}{2}}. \tag{3.31}$$

An example force-distance curve is shown in Figure 3.14(b). As shown in the insets of (b), a measurement will start with the probe out-of-contact with the sample and, once in contact, begin to measure the medium's linear response to the indenting probe. Two force-indentation curves for stiff and soft materials along with a Hertz contact model fit are

shown in (c). These fits may be applied using commercial software made by Optics11 Life or open-source software described in [169] to find E. Under more sophisticated analyses, such as dynamic mechanical analysis (DMA) [180], one could also obtain a sample's loss and viscous moduli by oscillating the probe on the sample's surface over various frequencies. However, for simplicity, we kept to E measurements in the work in this thesis.

In other cases, shear rheometers have been used to calibrate similar optical setups [86–91]. In our case, however, I dealt with many heterogeneous samples, such as brain slices later discussed, for which the smaller probes of the nanoindenter were more appropriate than those of a shear rheometer, which are typically millimetres in radius.

3.10 Conclusion

In this chapter, we reviewed the technical background of DCS, from how it is usually done in practice to some newer techniques that have been developed throughout my PhD. In the coming chapters, we will look at two new biomedical applications of DCS, from sensing neurodegeneration to imaging tumours in brain tissue. Then, in the final chapter, we will also look at speed improvements to the DCS technique, which improves upon the aforementioned pixel stacking approach with ML to incorporate other speckle techniques such as LSCI.

CHAPTER 4

Assessment of Neurodegeneration with Diffuse Correlation Spectroscopy

4.1 Introduction

In this chapter, we look at the first new application of DCS proposed in this PhD thesis: the remote assessment of neurodegeneration. This study aimed to determine if DCS could be an optical tool for neurodegeneration diagnosis since neurodegeneration induces stiffness changes in the brain. The scope of this study has two implications for the future:

1. DCS could aid in pharmacological studies and be used as another diagnostic protocol for disease progression
2. DCS could later be developed as a diagnostic tool for humans

Of course, the latter implication is a far-future goal and will require the development of the DCS technique to sense beyond blood flow and into the human brain tissue. Although some novel studies look at the transport of light deep into the human head [181, 182]. Thus, the former implication is more realistic in the near future. For example, such a technique could be used to track disease progression in mice in parallel to testing novel drug experiments on mice. The latter technique is a later goal, however, DCS is currently being used for human blood flow applications and thus shows promise in being translated to this neurodegeneration assessment application.

4.1.1 Prion Disease: An Analogue to Alzheimer's Disease

Prion disease is a neurodegenerative disease. To give more context, people may have heard of mad cow disease of Creutzfeldt-Jakob disease, which are specific strains of prion disease. My second supervisor, Andrew B. Tobin and his team have worked extensively

with murine prion disease models [9, 10, 183]. In general, prion disease may be considered an analogue to Alzheimer's disease, as both diseases result in learning and memory deficits and progressive and terminal neurodegeneration.

Prion disease is derived from the brain's misfolding of healthy prion proteins. A misfolded protein acts as a 'seed' that causes a chain reaction and misfolds other neighbouring healthy proteins. In time these misfolded proteins aggregate and cause learning and memory deficits. Although prion disease also comes with other hallmarks, such as neuroinflammation, neuronal loss, and lastly, progressive and terminal neurodegeneration, much like Alzheimer's disease. In the case of Alzheimer's disease, the seeds associated with disease progression are the amyloid beta and tau aggregates [9, 10, 16, 22, 183]. Therefore, these diseases are often described as spreading in a 'prion-like' manner. Prion-like diseases are more generally referred to as proteinopathies, which also include other neurodegenerative diseases like Parkinson's and Huntington's disease [184–188]. Therefore, prion disease largely represents other neurodegenerative diseases, and since our collaborators have been working broadly with them already and have access to prion mouse models, we use them in our DCS experiments.

Mouse Models and Preparation of Brain Samples

In our study, we aim to detect brain stiffness changes using DCS. We used two different mouse models, known as the wildtype (WT) and the tg37 hemizygous mouse strains. The difference between the two mouse strains is that the tg37 hemizygous mice express three times the cellular prion protein content than the WT mice, such that prion disease progression is accelerated. Out of the two mouse strains, three mouse populations were then used: 1) a non-diseased wildtype group (labelled as control-WT), 2) a non-diseased control tg37 group (labelled as control-tg37) and 3) a prion-diseased tg37 group (labelled as prion-tg37). Only the prion-tg37 mice were affected with prion disease and the other two populations were used as control groups.

Disease homogenates are what are used to infect the mice models. In prion disease research, the disease homogenate consists of brain matter with the misfolded prion protein. We obtained our disease homogenate from Rocky Mountain Laboratories. At 3-4 weeks of age, prion-tg37 mice were inoculated with 1% Rocky Mountain Laboratory prion-infected brain homogenate via intracerebral injection. To ensure that the control-tg37 mice were treated the same way, they were instead inoculated with normal brain homogenate, which does not consist of any misfolded prion proteins. Prion-tg37 mice were examined daily for indicators of prion disease as previously described in [10], and animals were culled from 11-13 weeks post-inoculation when they developed clinical signs of a terminal disease. Overall, 48 mice were used, consisting of 10 control-WT, 21 control-tg37, and 17 prion-

tg37. All animal work was performed under a project license in agreement with U.K. Home Office Regulations.

4.1.2 Hydrogel Slabs of Tunable Stiffness

In addition to mouse brain samples, we also studied synthetic hydrogel samples. Hydrogels are often used in mechanobiology to simulate various forms of biological media. Moreover, their Young's modulus is well-studied, and there are well-known recipes to tune their stiffness [189]. Measuring hydrogels with DCS was a calibration step in our study. To confirm that DCS is sensitive to stiffness changes induced by neurodegeneration, we first had to confirm the linear relationship between τ_c and E for our apparatus.

Past laser speckle rheology experiments by Hajjarian et al. [86–92] have been performed, which study τ_c in terms of shear modulus. However, we must also perform this calibration exercise between DCS τ_c and the hydrogels' Young's modulus since DCS is sensitive to measurement parameters such as laser wavelength and illumination spot size.

4.1.3 Nanoindentation Measurements of Brain Samples

Nanoindentation measurements performed with the Chiaro device described in Chapter 3.9 formed a basis of mechanical stiffness measurements of the brain for later comparison with the optical τ_c measurements. Only the control-tg37 and control-WT were assessed for these mechanical measurements. We did not assess the prion-tg37 mechanically, as this would have required harsh cleaning of the probe with sodium hydroxide (NaOH) to denature the misfolded prion protein and permanently damaged the Chiaro probes and/or Chiaro nanoindenter itself.

These mechanical brain measurements were performed under the standardised protocol in [169]. In more detail, we used a spherical contact of radius 3 μm, a cantilever of spring constant 0.022 N/m and obtained force-distance curves by indenting the sample at a speed of 2 μm/s over a range of 12 μm. This resulted in an indentation depth of 6 μm since the probe began indentation out-of-contact with the sample. Before fitting, the Hertz contact mechanics model to the force-distance curves to obtain stiffness, we filtered out scans that did not have a clear out-of-contact region followed by an in-contact region from the analysis. This filtering step was done by eye since the number of scans was not substantially large. 3 control-WT and 5 control-tg37 brains were measured mechanically, and we aimed for around 15 measurements of the hippocampus for each brain sample. Due to filtering, the number of usable measurements averaged out to 10 measurements per sample.

4.1.4 Optical Density Measurements

The optical density (OD) of a material describes how strongly light is attenuated when it passes through a medium. Scattering in a material may increase its OD and decrease its τ_c. If there are changes in a sample's τ_c, it is therefore also possible for there to be changes in its OD. It is defined as

$$\mathrm{OD} = \log_{10} \frac{I_{\mathrm{in}}}{I_{\mathrm{out}}}, \tag{4.1}$$

where I_{in} and I_{out} are the transmitted and input intensities, respectively. We measured the OD of brain slices and hydrogels using a power meter (Thorlabs PM400 with S120C head) and the aforementioned 633 nm laser. Measuring a sample's OD is substantially faster than performing DCS on it, so we also check for changes in OD between diseased and healthy brains.

4.1.5 Hypothesis Tests for Statistical Significance

Our analysis later used hypothesis tests (t-tests) to search for a statistically significant difference between prion-diseased and healthy brain slice DCS measurements. Statistical tests such as t-tests, analysis of variance (ANOVA) and random effects models are commonplace in biological studies. Below I give an overview of their background.

Imagine that there are two groups that have mean arbitrary measurements μ_1 and μ_2. Then a statistical test will make two postulates:

1. The **null hypothesis** H_0 is that there is no difference between the two groups' means
2. The **alternate hypothesis** H_1 states that there is a difference between both group means.

Unpaired t-tests constitute the simplest method of comparing the means of two groups that have small sample sizes. In our analysis, we use Welch's t-test. A standard t-test will assume that both groups will have equal variances, but Welch's t-test assumes unequal variances, which is well suited for two groups of unequal sample size [190]. Welch's t-test calculates the T-statistic, t, using the below equation,

$$t = \frac{\mu_1 - \mu_2}{\sqrt{\frac{\sigma^2_{\mu_1}}{N_1} - \frac{\sigma^2_{\mu_2}}{N_2}}}, \text{ where } \mu_1 > \mu_2. \tag{4.2}$$

Here, σ represents the standard deviation and N the sample size of each group. The group's true means and variances are unknown but are estimated from the T-distribution,

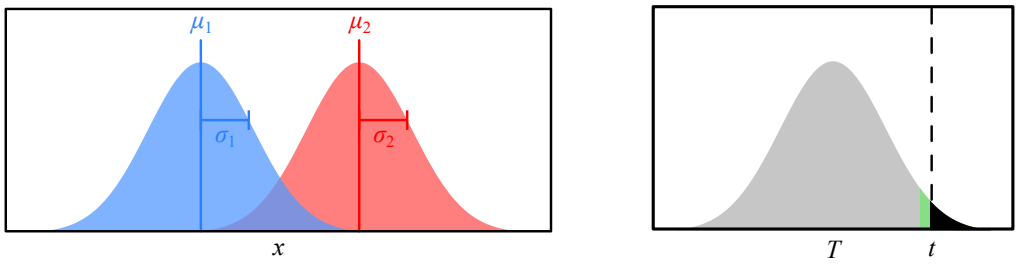

Figure 4.1: **Finding the p-value.** On the left are two PDFs. Their means and standard deviation annotated. The null hypothesis assumes that $\mu_2 = \mu_1$, whereas the alternate hypothesis states that their means are different. On the right is the T-distribution. The p-value is the area under the curve highlighted in black to the right of T. For a statistically significant difference between the red and blue populations, this shaded black area must be less than the shaded green area, i.e., p-value $\leq \alpha$.

defined below as

$$\frac{\Gamma(\frac{df+1}{2})}{\sqrt{df\pi}\Gamma(\frac{df}{2})}\left(1+\frac{t}{df}\right)^{(-\frac{df+1}{2})}. \tag{4.3}$$

Here, Γ is the gamma function, and $df = n - 1$ are the degrees of freedom. Probability values, or p-values, are then calculated and act as a measure of statistical significance. From the T-distribution, a p-value is obtained through

$$\text{p–value} = P(|T| \geq t|H_0). \tag{4.4}$$

Given that the null hypothesis is true, that $\mu_2 = \mu_1$, the p-value is the probability of observing an unknown test statistic T greater than or equal to t. Statistical significance is found through an arbitrary significance level α. In many cases, such as in biological studies, an α of 0.05 is statistically significant. α represents a fraction of the distribution, and $\alpha = 0.05$ means that 5% of the probability distribution rests on the right of alpha. t is thus defined with respect to what value α is set to. If a test statistic occurs on the right of t, then this would mean that, given that the null hypothesis is true, there is less than a 5% probability that the two sample distributions have the same mean. Therefore, the two groups are unlikely to be the same based on the measurement parameter used. More simply put, a p-value less than or equal to α rejects the null hypothesis and translates to a statistically significant finding [191]. Figure 4.1 illustrates how the p-value is obtained for two distributions.

In our experiment, we are particularly interested in finding a statistical difference between healthy and prion-diseased mouse brains based on the DCS measurements. Here, we look for p-values less than 0.05 between the healthy and diseased brain τ_c measurements. For this, we considered different types of statistical tests, from Welch's t-tests, ANOVA and

Tukey's t-test, and a random effects model. The choice of statistical test depends on the situation, such as the number of groups being studied or the design of the experiment.

One-Way Analysis of Variance

One-way ANOVA is an analysis that compares the means of multiple groups of measurements. For a three-group example (groups A, B and C), its null hypothesis states,

$$\mu_A = \mu_B = \mu_C. \tag{4.5}$$

The alternate hypothesis states instead that at least one of these group means is different. ANOVA tests are often paired with post-hoc tests, such as Tukey's test, which studies the difference in means between all pairs of groups.

One-way ANOVA represents a linear additive equation. Each observation Y_{ij}, for a group i and individual measurements j, may be written

$$Y_{ij} = \mu + \alpha_i + \epsilon_{ij}. \tag{4.6}$$

Here, μ is the overall mean of observations across all groups, α_i is a deviation from group i to the overall mean μ, and ϵ_{ij} is a nested error term that represents variability in a single group [192].

ANOVA is used to find if at least one of the groups being considered has a different mean by analysing variance between groups with respect to variance within groups. Once ANOVA has been performed on the measurements, a Tukey-Kramer t-test, which, like Welch's test, does not assume equal group variances, is applied to all mean group observations through SciPy's tukey_hsd function to determine which particular group is different. Here, the Tukey-Kramer test uses the following studentised range statistic, or q-statistic, q, which is specifically used for multiple comparison tests [192]. It is defined as

$$q = \frac{\mu_1 - \mu_2}{\sqrt{\text{MSE}(\frac{1}{n_1} + \frac{1}{n_2})}}, \text{ where } m_1 > m_2. \tag{4.7}$$

MSE is the mean-squared error and n_1 and n_2 are the sample sizes of the two populations being considered. q is calculated using the pooled variance of all groups, which makes it more robust than Welch's test for multiple comparisons, which only compares two groups. Then, the Tukey-Kramer test uses the studentized range distribution or Q-distribution to compare means from multiple populations [191, 193, 194]. The p-value is similarly obtained here as for the above Welch's test. Lastly, the Tukey-Kramer test can be repeated for each pair considered in the ANOVA to obtain a p-value for each pair.

Random Effects Models

In some cases, random effects models better represent the experimental design compared to an ANOVA and a post hoc Tukey's test, as they can account for hierarchy and dependency between observations [195].

Random effects models break down measurements of an experiment into fixed effects and random effects. Fixed effects are constants between individual measurements. For example, say we want to compare the grades of two different schools, each with several classrooms of students. One of those classrooms represents a fixed effect. Random effects incorporate some variability within those fixed effects. For example, students' grades may be normally distributed in one classroom. However, the distributions of students' grades between the classrooms may have different means, so it is not strictly fair to combine both classrooms into a single distribution before comparing each school's grades. Therefore, the grades of the students would have a fixed effect, and the class they belong to would have a random effect.

The following equation may represent a random effects model,

$$Y_{ijk} = \mu + \alpha_i + \beta_{j(i)} + \epsilon_{k(ij)}. \tag{4.8}$$

α here represents a fixed effect, and $\beta_{j,(i)}$ is a random effect term that represents a further deviation from the fixed effect, i.e. it is nested in the fixed effect. Parentheses and dimensions $\{i, j, k\}$ indicate nesting. $\epsilon_{k(ij)}$ represents the error and has an additional dimension k since errors are nested within each measurement.

After the random effects model is formulated, t-tests can be applied to the fixed effects to search for statistically significant differences between the groups. Random effects models may be applied in Python using the statsmodels module and the mixedlm function. Random effects models tend to be more statistically 'correct' but are not broadly adopted in biological studies. I include both analyses using ANOVA Tukey's test as well as the random effects model later in my thesis for completeness. Specifically, in our experiment, we obtain multiple biological and technical replicates of data, and the random effects model can correct for dependencies within the technical data replicates.

4.1.6 Western Blots: A Chemical Ground Truth of Disease Progression

Western blots, also known as protein immunoblots, are a common postmortem technique for determining the expression of specific proteins in a sample. As discussed previously

in Section 2.2.1, they are often used to determine the presence of neurodegeneration from the expression of particular proteins associated with neurodegeneration. In our case, we look at the misfolded prion protein expression and use Western blots as a ground truth measurement of neurodegeneration in the brain sample populations.

Western blots are a multi-step process, detailed in Figure 4.2. Taking the brain as an example, the following steps are performed [196]:

1. The brain will be extracted from an animal, and its contents will be broken down into their protein constituents to form a lysate.
2. The lysate is then diluted, and its protein content is separated by electrophoresis based on its molecular weight, a technique known as SDS-PAGE.
3. Separated proteins are then transferred to an absorbent membrane.
4. The proteins on the membrane are then stained, which allows for visualisation and quantification of the protein.
5. Following staining, blocking and then primary and secondary antibody incubation is necessary to study the expression of specific proteins. Blocking is done prior to antibody incubation and prevents non-specific binding of the primary and secondary antibodies to the membrane.
6. Fluorescence imaging is lastly performed to study the protein expression.

Loading controls are used to assess if the Western blot transfer was correctly done. A successful transfer will have a loading control expression that is uniform in each of the Western blot's columns. Evaluation of the loading control is imperative for following analysis that compares expression amongst the different columns in the Western blot [197]. A typical loading control is α-tubulin. It is a suitable loading control in the context of prion disease since its expression is not modified by the progression of prion disease.

In the context of prion disease, brain tissue is dissolved in proteinase-k to find the misfolded prion expression, as opposed to the misfolded and cellular (healthy) prion protein expression. After being dissolved in proteinase-k, the brain is left with the misfolded prion protein, which can be stained and imaged.

Other than misfolded prion expression, the expression of glial fibrillary acidic protein (GFAP), a protein marker for astrocytes, may also be studied. GFAP expression is increased with the progression of neurodegeneration and is associated with neuroinflammation [10, 183, 198].

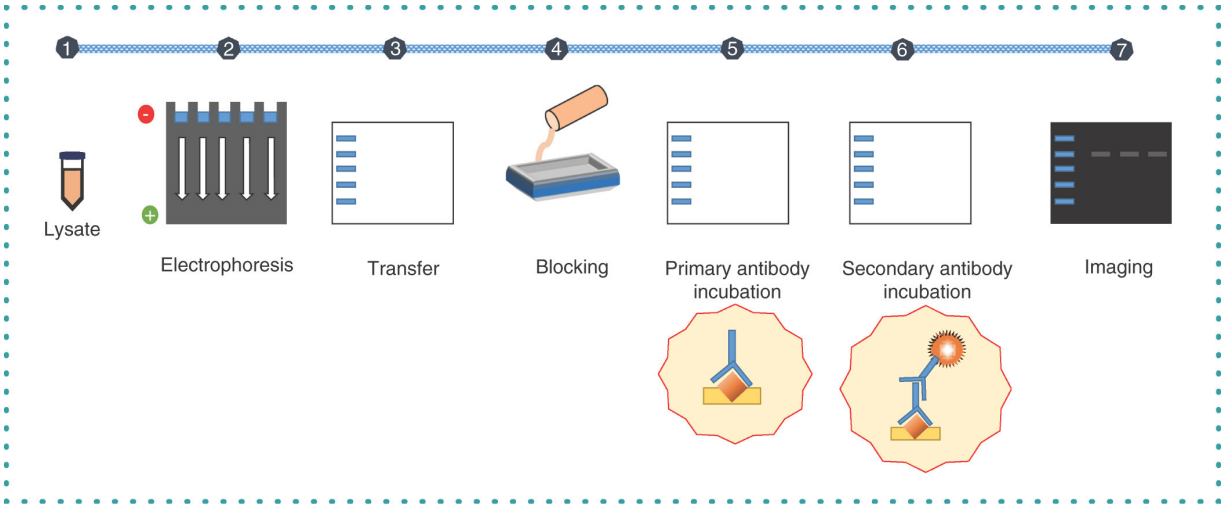

Figure 4.2: **The workflow of a typical Western blot.** Figure taken from [196].

4.1.7 Classification Tasks

The purpose of the previous hypothesis tests was to determine if there was a difference in diseases and healthy mouse brain populations. However, to determine how well DCS can differentiate brain samples on a case-by-case basis, i.e. to test its diagnostic capability, training a classifier is required. Here, we consider two classifiers: a Gaussian naïve Bayes' (GNB) and a support vector machine (SVM) classifier. It would be overkill to test any more classifiers, as there is already much overlap between each of the three populations. Below, I give a background of classification tasks.

Classification tasks fall under the overarching term of supervised learning. Here, a set of n feature vectors $\boldsymbol{x}_i$ are given a corresponding label y_i, for $0 < i \leq n$. For binary classification problems, there are two classes: the positive class for which $y_i = 1$ and the negative class for which $y_i = -1$. Observations from each class are then split into training and testing sets, which tune the classifier's hyperparameters. The test set comprises any data that the classifier does not see. It is important to split the dataset into training and testing sets so that the classifier does not have any bias towards the testing data.

When the sample size is small, it can be difficult to separate a test set from training and validation sets and test the classifier's efficacy. In these cases, certain validation strategies can gauge how well the classifier would work on unseen data. A simple strategy is the leave-one-out (LOO) cross-validation strategy. LOO cross-validation reserves one example from the training set to be used as a testing example and trains the classifier on the remaining features. By repeating this throughout all features, one can get obtain statistics for classified and misclassified features and tune their classifier for better performance.

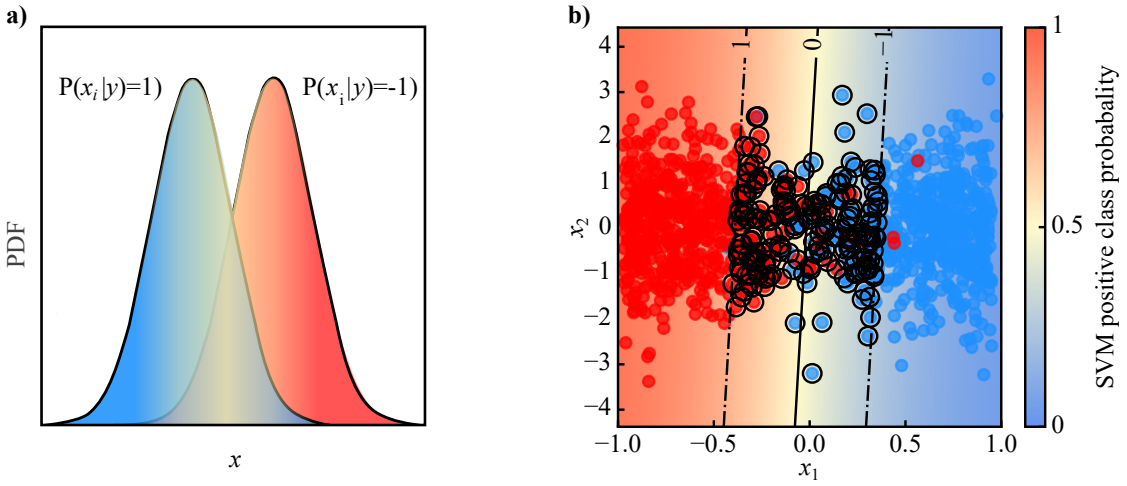

Figure 4.3: **Classifier examples.** a) A 1D example of a GNB classifier, whereby the blue curve represents the probability of the positive class and the red curve the probability of the negative class. The classifier outputs a class label 1 or -1 depending on which Guassian's amplitude is larger. b) A 2D example of a linear SVM classifier with soft margins on two overlapping data sets. Red and blue data points mark measurements with class 1 (red) and class 0 (blue). Data points circled in black are support vectors. Dash-dotted boundaries labelled 1 and -1 contain a margin of support vectors. The SVM aims to maximise this margin. A red-yellow-blue colour map in the background represents the probability of the positive class. The boundary labelled 0 represents the decision boundary of the SVM, which overlaps with the yellow in the background colour map.

Gaussian Naïve Bayes'

The GNB is a well-known and commonly used classifier [199, 200]. For $\boldsymbol{x}_i$ and y, it assumes that the likelihood of any input features is Gaussian,

$$P(x_i|y) = \frac{1}{\sqrt{2\pi\sigma_y^2}} \exp -\frac{(x_i - \mu_y)^2}{2\sigma_y^2}. \tag{4.9}$$

σ_y is the standard deviation and μ_y is the mean of the maximum likelihood. The notation $P(x_i|y)$ can be understood as the conditional probability of measuring x_i given that y has already been measured. It essentially gives a probability of whether x_i belongs to class y and thus can be used for classification tasks. Fig. 4.3(a) gives a visual example of how the GNB makes its decision. The blue and red PDFs are built using the above equation and the GNB classifier will output a classification -1 or 1 depending on which PDF is larger for a given x_i. $\boldsymbol{x}_i$ will be labelled according to the class distribution with the larger amplitude. A GNB is later made using GaussianNB from the scikit-learn Python module [199].

Support Vector Machines

A SVM is a supervised machine learning approach and can be used for classification problems. An SVM classifier aims to fit a hyperplane that separates classes from each other. One can think of the hyperplane as consisting of a decision boundary and two margins. The decision boundary is learned using a set of points known as support vectors, which lie in close proximity to it.

A linear SVM uses a linear decision function given by

$$D(\boldsymbol{x}) = \boldsymbol{w} \cdot \boldsymbol{\phi}(\boldsymbol{x}) + b. \tag{4.10}$$

Here, $\phi(x)$ is the hyperplane, which is a function of the support vectors x. $\boldsymbol{w}$ is a vector of weights perpendicular to the hyperplane and b is a scalar bias parameter. The decision function represents the hyperplane that separates the classes. If the decision function returns $D(\boldsymbol{x}) > 1$, then that feature vector will be classified as the positive class, and vice versa. The separating hyperplane rests as $D(\boldsymbol{x}) = 0$ [199, 201, 202].

An SVM classifier example is shown in Figure 4.3(b), which illustrates how it performs 2D binary classification. A SVM is later made using LinearSVC from the scikit-learn Python module [199].

Sensitivity and Specificity

For binary classification problems, one can form a confusion matrix, which is an intuitive tool for interpreting the performance of the classifier under cross-validation or testing. A binary classifier will have a two-by-two confusion matrix, which looks like,

$$\begin{bmatrix} TP & FN \\ FP & TN \end{bmatrix}. \tag{4.11}$$

Here, TP is the number of true positives and represents the number of samples from the positive class that the classifier identified as the positive class. FN represents the number of false negatives and is the number of samples from the positive class that were falsely identified as belonging to the negative class. Similarly, TN is the number of true negatives and represents samples from the negative class that were correctly identified as the negative class. Lastly, FP is the number of false positives and is the number of samples from the negative class that were mistakenly given a positive label by the classifier.

Two important characteristics of a classifier are sensitivity and specificity. These are popular performance metrics to see how a classifier would perform on samples not contained in its training set when used in conjunction with LOO cross-validation. The sensitivity,

which is also known as the recall, is the true positive rate and is defined as,

$$\text{sensitivity} = \frac{TP}{TP + FN}. \tag{4.12}$$

High sensitivity is always preferred and shows that a classifier is strong at detecting the presence of the positive class.

Specificity is known as the true negative rate and is defined as

$$\text{specificity} = \frac{TN}{TN + FP}. \tag{4.13}$$

Like sensitivity, high specificity is also always wanted. It is the ability of the classifier to detect the negative class.

For a generalisable classifier, finding a good trade-off between sensitivity and specificity is important. Take, for example, a test that detects the presence of a disease and has high sensitivity but low specificity. This would mean that instances classified as positive may have been misclassified from the negative class. Thus, a positive prediction is inconclusive as one cannot be sure of a disease instance. In the opposite case, where the test has a low sensitivity and high specificity, some disease instances are not caught by the test.

Receiver Operating Characteristic Curves

A useful visual aid in understanding sensitivity and specificity is the receiver operating characteristic (ROC) curve. It plots the sensitivity against specificity. To obtain values of sensitivity and specificity for the binary classification problem, a cutoff, as shown in Figure 4.4(a), is adjusted, and sensitivity and specificity may be found by calculating the area of each PDF up to the cutoff.

A ROC curve diagram is illustrated in Figure 4.4(b). An ideal ROC curve will look almost like a low-to-high step function and have high sensitivity for high 1-specificity. A poor classifier is a random classifier portrayed as a linear ROC curve. The area under curve (AUC) is a good measure of a classifier's performance and is equal to 1 for a perfect classifier. In contrast, a random classifier's ROC AUC is equal to 0.5, which represents a fifty-fifty guess or a coin toss.

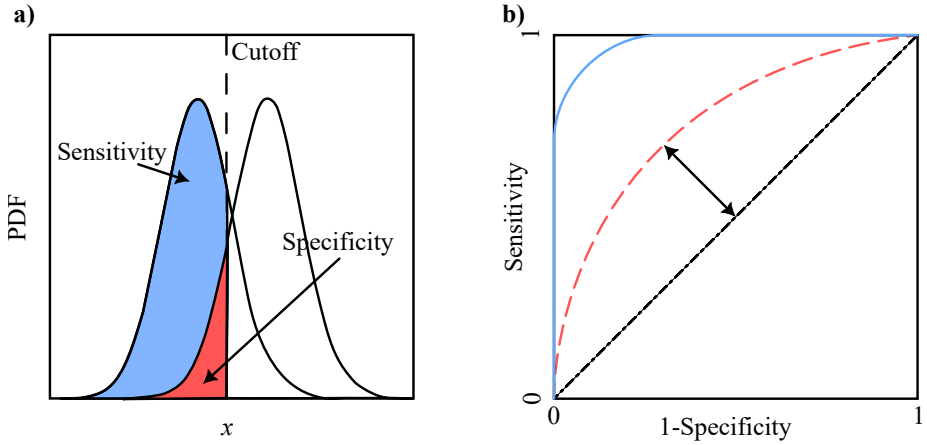

Figure 4.4: **ROC curve example.** a) Two PDFs with coloured regions indicating how sensitivity (blue) and specificity (red) are measured with respect to a cutoff, which travels along x. b) Three example ROC curves are shown: An ideal classifier (solid blue line), A good classifier (dashed red line) and a random classifier (dash-dotted black line).

4.2 Apparatus and Measurement

4.2.1 Apparatus

The specific DCS apparatus used for this chapter is presented in Figure 4.5. This is a transmission sensing configuration like Figure 3.3(a). A 1 mm brain slice sample rests in a glass-bottomed imaging petri dish on the sample plane. 633 nm light from a continuous wave (CW) laser (RPMC RO633) is focused into a 1 mm diameter spot on the bottom surface of the brain slice. A SPAD camera (PhotonForce PF32) captured the transmitted speckle pattern at 100 fps for 2 minutes per scan point. A translation stage was used to perform a five-point scan along the hippocampus of the brain slice. This scan was repeated three times for each brain sample. Thus, for each brain slice, there were fifteen measurements (five at different spatial points on the brain and three at different time points), which took around 30 minutes per brain. This 30-minute total acquisition time was a trade-off between obtaining a statistical average of DCS measurements and keeping the brain viable. The input and output laser light was cross-polarised to limit the amount of transmitted ballistic light on the SPAD camera. A 633 nm bandpass filter was also used for background light suppression. A reference camera with green light-emitting diode (LED) illumination imaged the bottom surface of the brain slice and helped to focus the laser onto the hippocampus. This reference camera and LED light source were set up in a dark-field microscopy configuration to improve contrast, as the brain slices were thick. The speckle size of the transmitted speckle was controlled by the distance of the imaging objective to the sample. The speckle size was calibrated to one speckle per pixel through a spatial

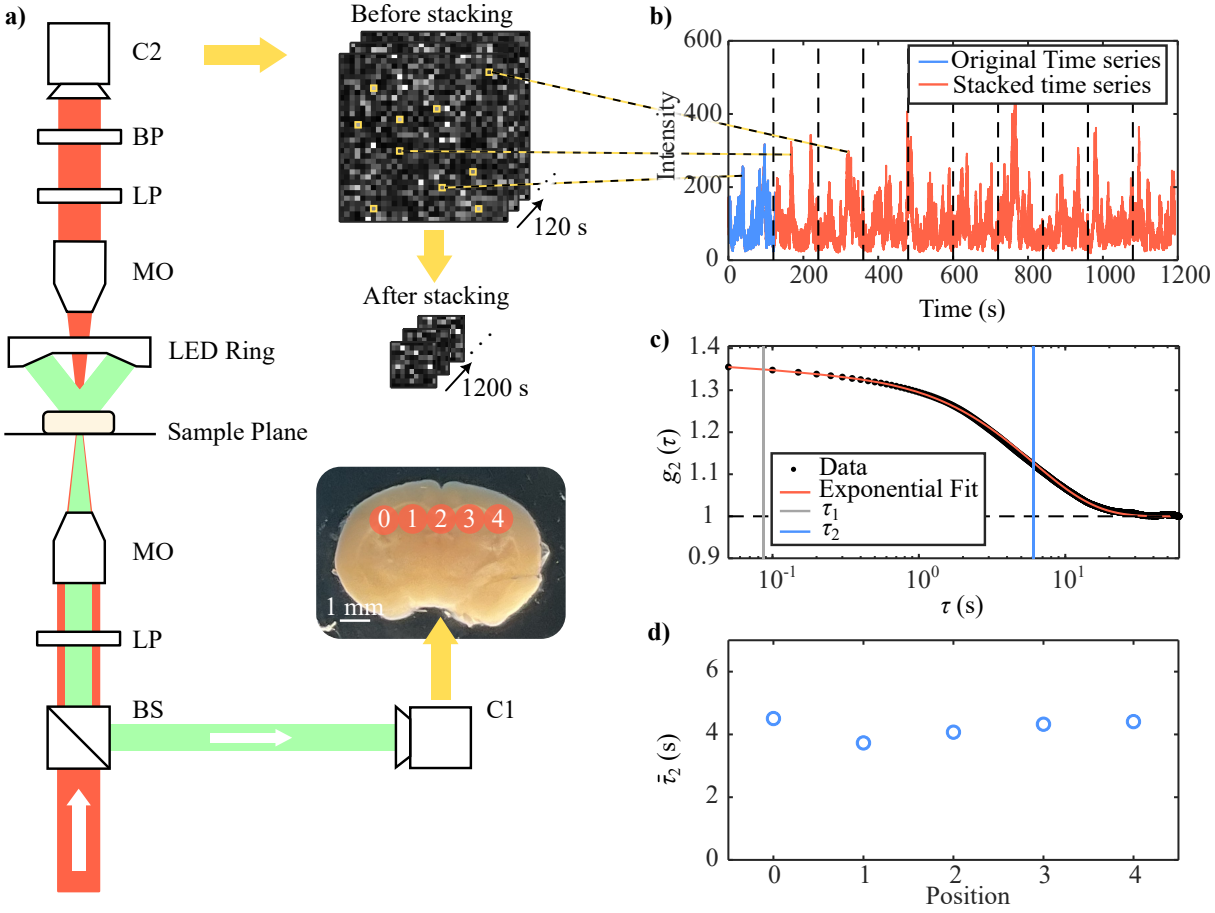

Figure 4.5: **Experimental layout and workflow.** a) The DCS setup. 633 CW nm light is passed through a linear polariser (LP) focused onto a 1 mm diameter spot on the mouse brain hippocampus with a microscope objective (MO). The transmitted light is cross-polarised, filtered with a 633 nm bandpass filter (BP) and imaged with a single-photon camera (C2). The bottom surface of the brain slice is also imaged for reference with a CMOS camera (C1) and green LED light source. An example white light image of a typical brain slice is shown as an inset, which shows a 5-point scan along the hippocampus of the brain slice. Another inset shows the optical speckle pattern measured by C2. The pixels of this speckle pattern are concatenated to effectively increase the acquisition time of the experiment. 10 random pixels in the speckle series are concatenated to make a lower-resolution speckle that is 10 times its original length. b) The time series of a single pixel is shown in blue, and the whole stacked time series in red. black dashed vertical lines are shown where time series have been concatenated. d) An intensity correlation (g_2) trace and corresponding multi-exposure fit. Vertical lines show the τ_1 and τ_2 values for this fit. d) $\bar{\tau}_2$ measurements for all positions scanned in a single brain sample. These measurements are later used for statistical analysis.

autocorrelation function [203], like in the works of [78, 80]. Since the PF32 SPAD camera did not have a high fill factor, a CMOS camera was first used to calibrate the speckle size

and was then replaced with the SPAD camera for DCS measurement[1]. As a last control step, before each DCS scan the temperature of the brain was checked with a temperature probe (Thorlabs TSP01) to make sure that the brain had acclimatised and any effects of temperature change on the DCS measurement was minimised.

4.2.2 DCS Analysis Workflow

Figure 4.5(b-d) describe the g_2 post-processing pipeline. Firstly, the intensity time series of pixels are randomly stacked (stacks of 10 pixels) using the method described in Setion 3.4 to create a longer speckle series effectively 10 times the length of the original time series. After this step, the mean g_2 trace of the speckle can be found for the remaining concatenated pixels with limited bias from short acquisition times. For fitting the mean g_2 trace, we found that the multi-exponential model used by Liu et al [105] and defined previously in Equation 3.29 worked the best for our data. The fast component of the multi-exponential fit was on the scale of milliseconds and, moreover, had a much smaller decay amplitude than the slow component, i.e., $\rho_1 << \rho_2$. Thus we deemed τ_1 to account for experimental noise. τ_2, on the other hand, was the dominant signal and was used for further statistical analysis. The five-point scan outputs five τ_c hippocampus measurements, which we apply hypothesis tests later.

4.3 Brain Slice Nanoindenter Measurements

Fig. 4.6 shows two box plots of E obtained from control-WT and control-tg37 nanoindenter measurements. The respective E measurements for the control-WT and the control-tg37 groups were 164.51 ± 19.24 and 206.70 ± 22.19 Pa. No statistically significant difference in E was observed between the two populations, suggesting that although the control-tg37 population was bred with three times the cellular prion protein content as the control-WT, there was no difference in their overall stiffness.

Nanoindentation measurements could not be performed on the diseased prion-tg37 population. For these measurements to occur, the nanoindenter required cleaning with NaOH to denature the misfolded prion protein, which would have permanently damaged the nanoindenter device.

[1]It is worth noting that the SPAD camera was not necessary for this experiment. We initially began experiments with it due to its high frame rate capability, and because the mouse experiments were performed over various runs (the mice had to be bred), no parts of the experiment could be changed between runs.

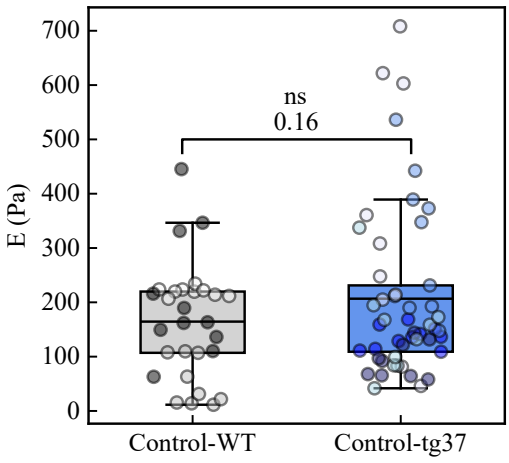

Figure 4.6: **Brain slice nanoindenter measurements.** Box plots of E for control-WT (sample size 29) and control-tg37 (sample size 49) populations measured with the nanoindenter. Overlaid are individual E measurements in different colours to indicate different brain samples. A Welch's t-test p-value is also annotated and shows no statistical significance between the control populations. Horizontal black solid lines in each box represent the population mean. Box boundaries indicate the inter-quartile range, and whiskers indicate the farthest data point lying within 1.5× the inter-quartile range.

4.4 Hydrogel DCS Measurements

1 mm thick polyacrylamide hydrogel samples were made according to the recipe detailed in [189]. Their E was tuned to the above brain nanoindenter measurements, $E = 200 \pm 30, 480 \pm 160, 710 \pm 240, 1100 \pm 340$ Pa. Lastly, to make the hydrogels light scattering for DCS measurements, TiO_2 at a final concentration of 5 mg/mL was added to the pre-polymer solutions. This concentration of TiO_2 was very low compared to the rest of the mixture and was assumed to have a negligible effect on its E. At this concentration, the mean OD of the hydrogels was measured to be 1.80 ± 0.01, which was similar to the mean OD of the mouse brains (1.87 ± 0.01).

Fig. 4.7 shows results for the above four hydrogel samples and their respective DCS τ_c measurements. There is a linear dependence between hydrogel E, which agrees with the work of [86]. The results indicate a linear relationship between τ_c and E. After this calibration step, the following experiment comparing τ_c of healthy and neurodegenerated samples is validated.

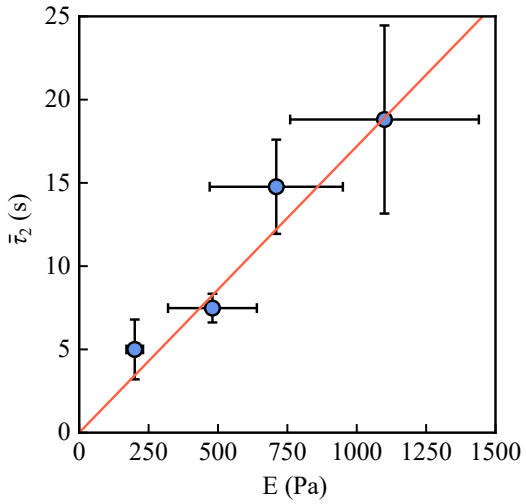

Figure 4.7: **DCS hydrogel measurements.** DCS τ_2 measurements (8 DCS measurements per sample) vs hydrogel E with a linear fit represented by a solid red line (r-squared=0.94, $\tau_2 = 0.017E$). Error bars represent standard deviation.

4.5 Confirmation of Neurodegeneration through Western Blot Analysis

To confirm the presence of the disease before analysing the DCS results, a subset of the mouse brain samples (11 prion-tg37 and 9 control-tg37) were also tested through Western blot analysis. The samples were digested in proteinase-K (PK) to determine the level of misfolded prion expression and non-digested otherwise to find the total prion protein (healthy/cellular and diseased/misfolded), GFAP, and α-tubulin expression. These Western blots were carried out by Aisling McFall and its results are presented in Fig. 4.8. In Fig. 4.8(a), a clear difference is seen between the prion-tg37 and control-tg37 misfolded prion expression columns. Regarding GFAP expression, prion-tg37 bands are also thicker than control-tg37 bands. Welch's t-test shows statistical significance between the control-tg37 and prion-tg37 populations for both misfolded prion (b) and GFAP expression (d), thus confirming that the prion-tg37 population is diseased. Due to no presence of misfolded prion expression in the control-tg37 population, these samples were confirmed as having no disease.

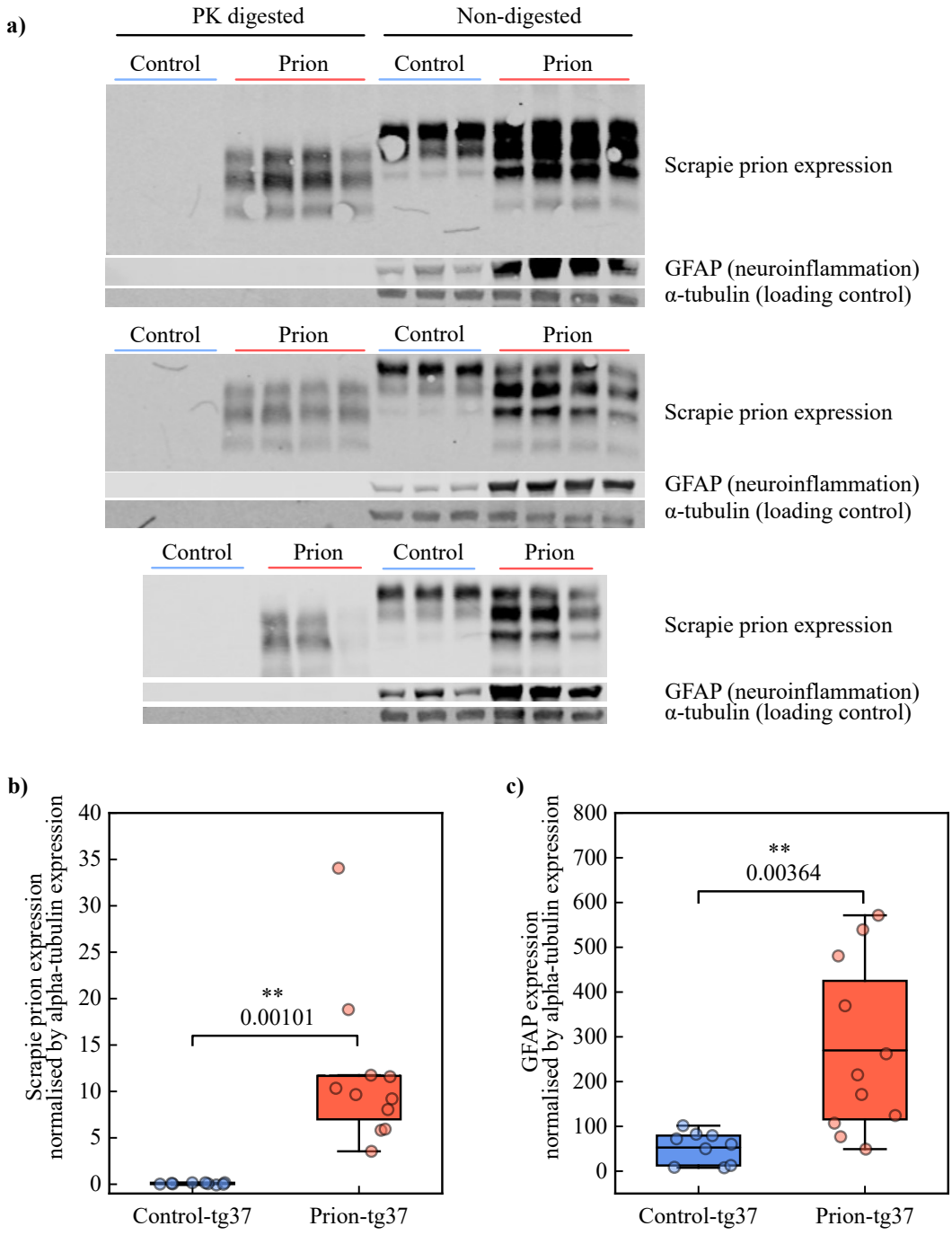

Figure 4.8: **Confirmation of neurodegeneration with Western blots.** a) Western blots showing misfolded prion and GFAP expression for prion-tg37 (11 samples) and control-tg37 (9 samples) brain slices. Blots of α-tubulin are also shown, which acts as a loading control. The misfolded prion expression can be worked out from the PK-digested columns, and from the non-digested columns, the GFAP and α-tubulin expression can be found. b) box plots of misfolded prion expression for control-tg37 and prion-tg37 samples. c) box plots of GFAP expression for control-tg37 and prion-tg37 samples. Both (b) and (c) have annotations of Welch's t-test p-values, and both show statistical significance. Horizontal black solid lines in each box represent the population mean. Box boundaries indicate the inter-quartile range and whiskers indicate the farthest data point lying within 1.5× the inter-quartile range. Aisling McFall produced western blots and data.

4.6 Statistical Differences between Healthy and Neurodegenerated Mouse Brain Samples

Statistical tests on ex vivo DCS measurements are the first step to developing DCS towards neurodegeneration assessment. Results for this are presented in Fig. 4.9. Fig. 4.9(a) shows colourmaps for τ_2 position and sample. Here, the mean τ_2 for each scan point has been used and labelled $\bar{\tau}_2$. Measurements for each population (control-WT, control-tg37, and prion-tg37) are shown in blocks together. However, these DCS measurements were performed blindly, with their true labels revealed after measurements. Considering each population's colour map, a pattern can be made out by eye where the τ_2 of the prion-tg37 is red-shifted compared to the control-WT and control-tg37 populations, i.e., the prion-tg37 measures on average shorter τ_2.

Statistical evaluation of disease progression was performed by means of ANOVA and post hoc Tukey's tests. Box plots with Tukey's test p-value annotations are depicted in Figure 4.9(b). ANOVA resulted in a p-value of 0.00093, indicating that at least one of the three populations differed. Tukey's test then found statistically significant differences between control-tg37 and prion-tg37, control-WT against prion-tg37, and control-tg37 and control-WT, but not between control-tg37 and control-WT. Simply put, a difference in population means was seen between the control and neurodegenerated populations but not between the two control populations. No difference was also observed for the E measurements between the two control populations. Now also considering the hydrogel calibration measurements that showed our device's τ_c was sensitive to stiffness, our results indicate that there is a difference in tissue stiffness between healthy and neurodegenerated brain slices probed remotely and optically by DCS, whereby neurodegenerated brain samples are statistically softer than healthy brain samples.

4.7 Random Effects Model Analysis

In our case many different τ_2 observations performed within the same brain slice are dependent because they were performed on the same sample. In this sense, different brain samples represent biological replicates and within those samples different measurements represent technical replicates. ANOVA and Tukey's analysis in the past section did not account for the nesting of technical replicates in the biological replicates, however, a random effects model can. In this section, we show that there is still a statistically significant difference between the control-tg37 and prion-tg37 populations even when substituting a random effects model for the ANOVA and Tukey's analysis.

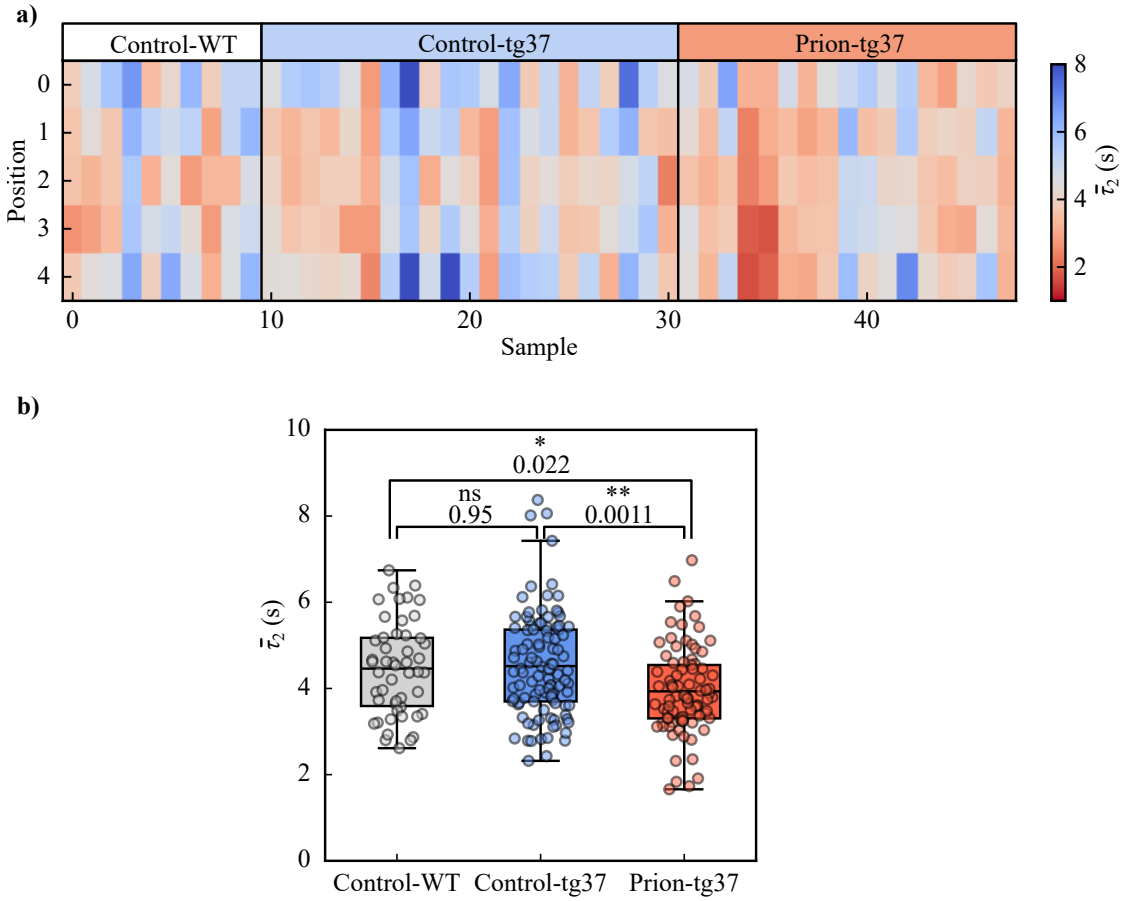

Figure 4.9: **Mouse brain DCS results.** a) Colour plots of $\bar{\tau}_2$ for control-WT, control-tg37 and prion-tg37 populations with sample and scan position axes ($\bar{\tau}_2$ is a mean DCS measurement for a single scan point). Solid black lines indicate boundaries between each population. b) $\bar{\tau}_2$ box plots of the control-WT, control-tg37 and prion-tg37 populations. Individual circles indicate different τ_c measurements (5 per brain sample). p-values from Tukey's tests are annotated above each respective box plot pair, and individual $\bar{\tau}_2$ are also overlaid. Horizontal black solid lines in each box represent the population mean. Box boundaries indicate the inter-quartile range and whiskers indicate the farthest data point lying within 1.5× the inter-quartile range.

Random effects analysis was performed using the *MixedLM* function from the Python Statsmodels module [204]. We make a nested random effects model that contains mouse brain slice positional τ_2 measurements, which are then nested in the brain sample. This mixed effect model design is illustrated in Fig. 4.10(a).

Results from the nested random effects model are shown in Fig. 4.10(b), where a p-value of just less than 0.05 is observed between the control-tg37 and prion-tg37 mouse populations. Therefore, with more stringent statistical analysis that accounts for hierarchy in the experiment, there is still statistical significance between the diseased and healthy populations in τ_2.

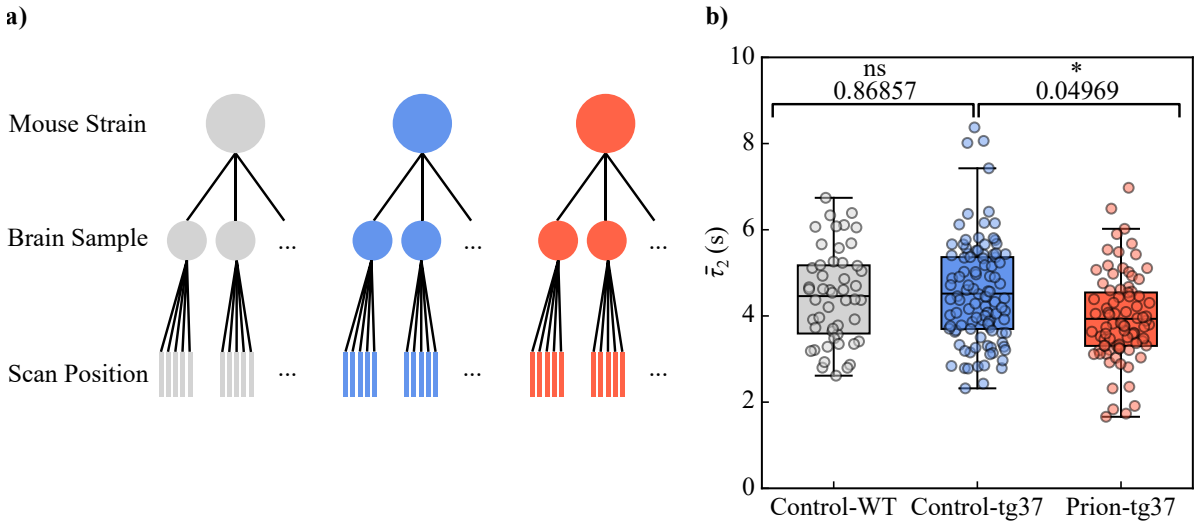

Figure 4.10: **Mouse brain DCS results with random effects model.** a) The random effects model architecture. τ_2 positional measurements nested in each brain slice, which then belong to either the control-WT, control-tg37 or prion-tg37 strain. b) Box plots for each mouse population with random effects model p-values annotated. There is still statistical significance between the diseased and healthy control populations. Individual circles indicate different τ_c measurements (5 per brain sample).

4.8 Mouse Brain Optical Density Measurements

Figure 4.11 shows box plots of OD for all three mouse populations. OD measurements presented are mean measurements manually taken around the hippocampus. Because these measurements were done with a different apparatus with less control to the above DCS measurements, we quote a mean OD value rather than an OD value for each scan point like in the DCS results. Annotated are ANOVA post hoc Tukey's test p-values, indicating no statistical significance between the mouse populations in terms of OD. This result suggests that the differences in the mouse populations that we observe are indeed due to stiffness changes.

4.9 Classification for Diagnostic Capability

Figure 4.12(a-b) show the the previous box plots with colour maps of the GNB and SVM classifier prion class probabilities. Figure 4.12(c) shows confusion matrices from both classifiers from which the sensitivity and specificity are calculated using Equations 4.12 and 4.13 to be 0.60 and 0.56 for the GNB classifier and 0.45 and 0.71 for the SVM classifier. AUC for the GNB and SVM classifiers are respectively 0.62 and 0.56 indicating that although the sensitivity of the SVM is worse than the GNB, it performs better. Neither classifiers perform well owing to a great overlap between the control-tg37 and

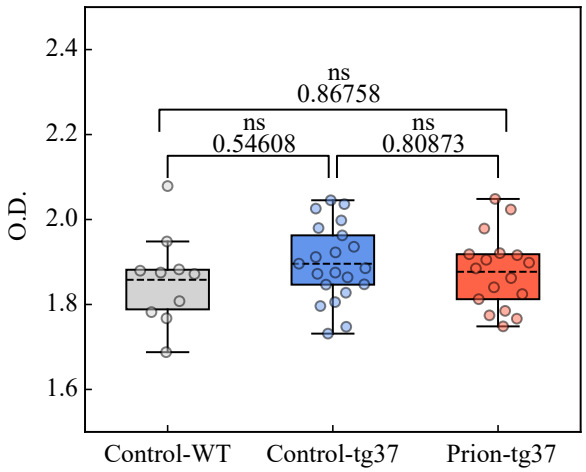

Figure 4.11: **Mouse brain optical density measurements.** No statistical significance is seen between each of the mouse populations, indicating that a change in the brain's optical density or transparency is not the cause of the change in the brain's τ_c. Individual circles indicate different averages of τ_c for a separate brain sample.

prion-tg37 populations and, as it stands, the current DCS implementation does not have good diagnostic ability.

4.9.1 Comparisons with Other Neurodegeneration Assessment Tools

We discussed previously other diagnostic tools for assessing neurodegeneration. The Western blot method is used routinely but is a postmortem technique that requires rigorous training. Nonetheless, as seen in Figure 4.8, it is very sensitive to detecting neurodegeneration. Otherwise, MRI scans are the non-invasive gold standard method of diagnosing neurodegeneration. [23] provides a broad list of MRI studies conducted on animal models

Study	Mouse population	Diseased vs healthy % difference
Our study	Prion, tg37	13.05%
Munder et al. [25]	Alzheimer's, APP23	9.66%
Hain et al. [24]	Parkinson's, C57BI/NI	35.96%
Majumdar et al. [26]	Alzheimer's, 5XFAD	1.66%
Palotai et al. [205]	Alzheimer's, J20	22.94%

Table 4.1: **Comparison of neurodegeneration assessment tools.** Comparisons of absolute percentage error of our technique to various MRE studies. The above table has been adapted from [23].

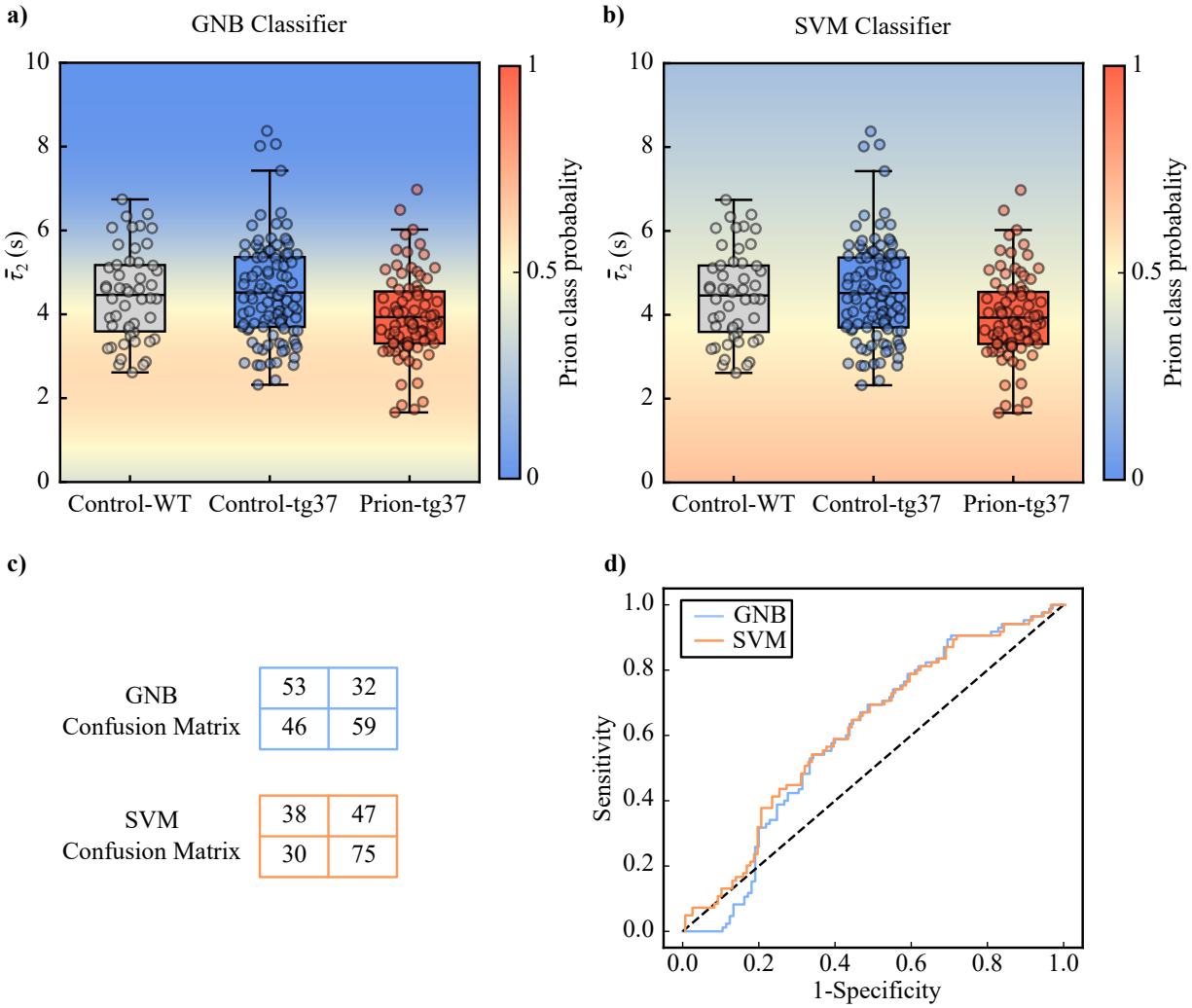

Figure 4.12: **Classification of mouse brain condition.** a) Aforementioned τ_2 box plots now with the GNB classifier's prion class probability displayed as a colour map in the background. b) The equivalent of (a) for the SVM classifier. c) Confusion matrices for the GNB and SVM classifiers. d) ROC curves for the GNB and SVM classifiers with the trace of a random classifier depicted as a dashed black line.

and humans affected by neurodegeneration (Alzheimer's and Parkinson's). For comparison with our own study, I have listed absolute percentage differences between healthy and neurodegenerated measurements on various neurodegenerative mouse models in Table 4.1. All studies in this table showed reduced brain stiffness in the diseased groups. Using the absolute percentage error as a metric, our study shows comparable sensitivity to MRE studies. The efficacy of the studies varies widely, which could be due to the experiment parameters and mouse models used. Hain et al. [24], for example, analysed 14-month-old Alzheimer's mice and were substantially more sensitive to the diseased group compared to the other Alzheimer's studies conducted by Majumdar et al. [26] and Munder et al. [25], who both analysed mice only up to 2 months of age.

4.10 Conclusions

We have implemented DCS in a novel scheme for remote and optical assessment of neurodegeneration ex vivo and report a statistically significant difference in speckle decorrelation times between healthy and prion-diseased mouse brain samples that are otherwise not detected by the OD of the brain samples. Disease progression in the brain samples was confirmed with Western blots. The DCS device was calibrated against hydrogels of tunable stiffness and indicated that neurodegenerated brain samples were statistically softer than healthy samples. For this technique to become medically relevant, however, more work must be done on improving its diagnostic capabilities, as current classification results struggle to differentiate between diseased and non-diseased cases. A broader future outlook for this experiment is discussed in Chapter 7.

CHAPTER 5

Imaging Hidden Stiffness Changes in Tissue with Diffuse Correlation Spectroscopy

5.1 Introduction

The concept of using DCS for imaging was first introduced in Chapter 3 using a lamb brain cerebellum as an example. In this chapter, we instead use DCS to image relative stiffness changes in biological tissue. In Chapter 2, we discussed cases where tumours, although looking like surrounding healthy tissue under white light, exhibit different stiffness to healthy tissue, and in the previous chapter, we saw that DCS is sensitive to stiffness. One case where tumour segmentation is difficult is in the operating room during neurosurgery. In such cases, surgeons are initially guided by preliminary CT or MRI scans but are otherwise unaided during surgery. Therefore, a particularly well-suited application to our DCS imaging technique is perhaps in intraoperative tumour segmentation as a visual guide to aid surgeons in tumour removal.

Another area of interest pertaining to surgery is the imaging of relative bone differences. Imaging relative stiffness differences in bone is also an interesting problem with surgical implications. For example, it is known that defects in bone, such as osteoporosis and osteoarthritis, differ in stiffness from normal bone [206]. In the final section of this chapter, we will also discuss the technique applied to bone imaging.

5.1.1 Tumour Proxies

As discussed in Chapter 2, we saw that tumours differ in stiffness from healthy tissue. Since we did not have access to samples with genuine tumours, we instead devised a method of changing a material's stiffness without drastically changing its appearance. PFA is a good option in this respect and is broadly used on biological samples before staining and

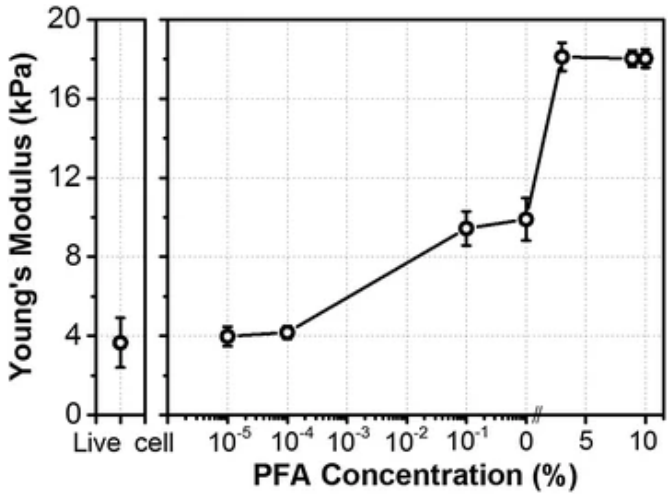

Figure 5.1: **Young's modulus of fibroblast cells vs PFA concentration.** Fixing a sample with PFA can stiffen the sample. Figure taken from [207].

imaging. A consequence of fixing a tissue with PFA is that its stiffness also increases, as was investigated by [207], whose results are shown in Figure 5.1. For PFA concentrations of $< 5\%$, one could achieve a doubling in the sample's Young's modulus. This was observed for fibroblast cells in [207], so we will need to determine the effect of stiffening for our experiments too, which is done later with the same nanoindenter used in Chapter 4 and in comparison with rheology tumour measurements in literature.

5.2 DCS Imaging Setup

The DCS imaging setups used for the following results of this chapter are detailed in Figure 5.2. In (a), a sample imaged by a camera (Basler acA2440-75uc) and objective and illuminated by various light sources is shown. The white light source paired with the camera provides a means of viewing the sample as a surgeon would and will be used as a reference image for comparisons later. Otherwise, an ultraviolet (UV) light source was used for a ground truth image. Here, the PFA fixative was also mixed with a fluorescent dye DAPI (4',6-diamidino-2-phenylindole, dihydrochloride), which was purchased from ThermoFisher Scientific. A OneStep solution of PFA and DAPI [208] (final PFA concentration of 2.8%) was prepared for injection into the samples to create a localised stiff tumour proxy in the proceeding samples. The PFA/DAPI solution is excited by 358 nm wavelength light and therefore, a fluorescent image of the sample will act as a ground truth of the localised tumour proxy region. Lastly, a DCS image can be obtained when the sample is illuminated by the green 532 nm laser (Thorlabs DJ532-40), which had a coherence length quoted at ~ 10 m.

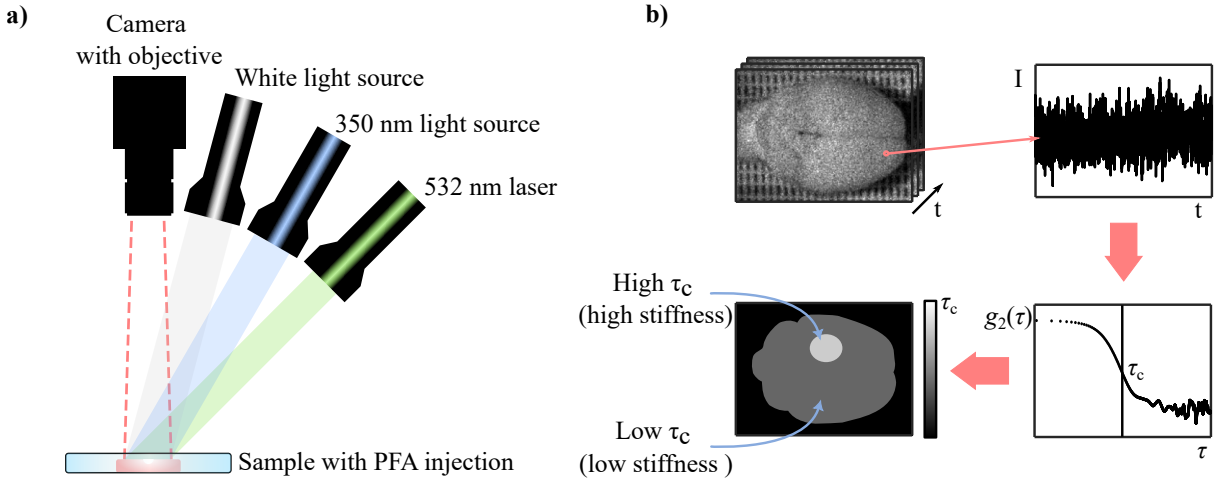

Figure 5.2: **DCS Imaging Setup for Detecting Hidden Stiffness Changes.** a) A diagram of the setup. An sCMOS camera with a camera objective images the surface of a biological sample. A portion of the sample is injected with a mixture of PFA and fluorescent dye, which changes its stiffness with time. There are three light sources: A 532 nm laser flood illuminates the sample and produces a speckle pattern series that is later processed to create the DCS image. A UV light source excites the fluorescent dye and provides a ground truth of where the fixed tissue is. Lastly, a white light source simulates what the sample would look like to the human eye. These light sources are illuminated sequentially for data acquisition; they are not turned on simultaneously. b) A post-processing pipeline of the DCS image computation. A speckle series is first captured, and the τ_c of each pixel is computed by Equation 3.25. Long τ_c correlates with high-stiffness tissue and vice versa. In this example, we show a speckle series of a mouse brain.

The DCS post-processing pipeline is described in (b). First, a speckle pattern series is acquired over a period. Then the τ_c of each pixel is found through Equation 3.25 and a DCS image can be obtained by plotting the colour map of τ_c values.

Since the work in this Chapter is new, I have approached its discussion from the ground up. I used injections of PFA/DAPI to mimic a stiff tumour and tested our method on two different biological media: pork fillet and mouse brains. In the next section, we confirm that the PFA/DAPI injection is a suitable tumour proxy by comparing it to a water injection.

5.3 Water vs PFA Injections

First, the validity of using PFA as a stiffening agent was tested on pork fillet samples. For validation-type experiments, the pork fillet samples were much easier to work with than the brain samples because they were largely homogeneous, easier to obtain, and easier to cut into flat samples. In this section, we work on understanding the fixing mechanism

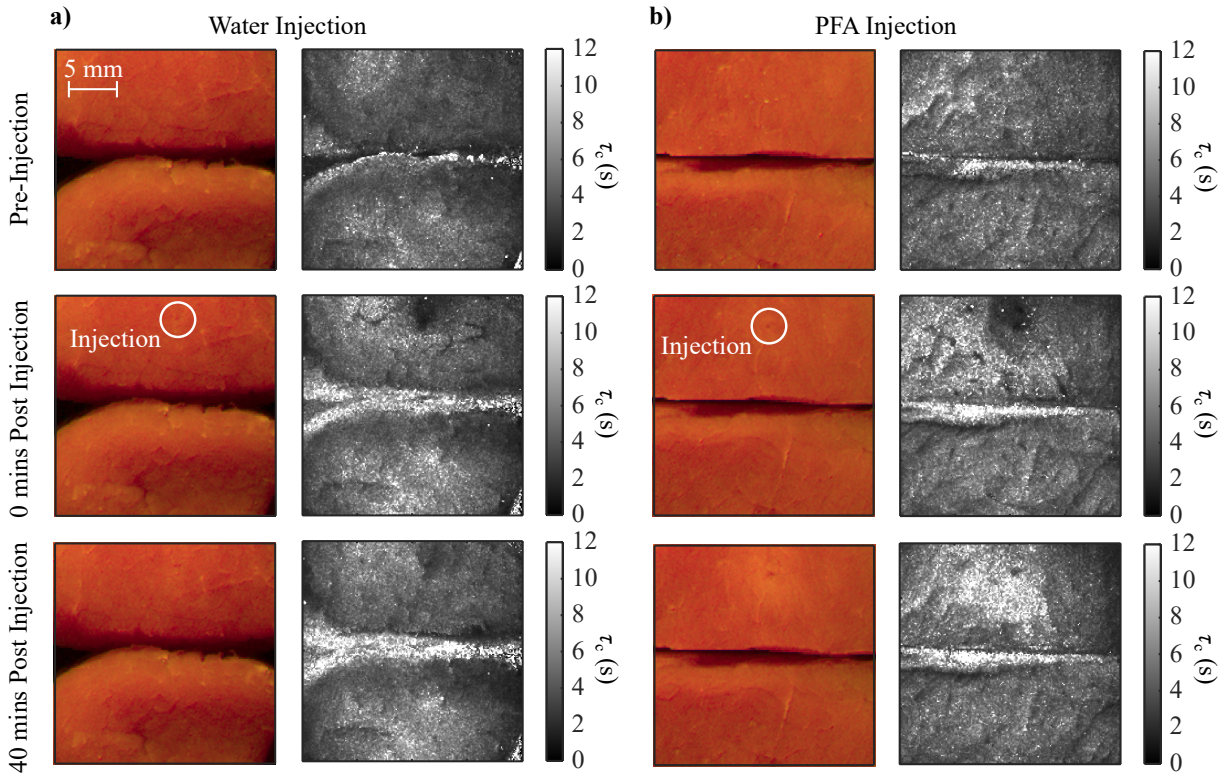

Figure 5.3: **DCS imaging analysis of water and PFA injections on pork samples.** a) Two columns showing intensity colour images and DCS τ_c colour maps of pork samples with water injections. b) The equivalent columns only now for PFA injections, which stiffen the pork sample around the injection site over time. The injection site is circled in white and located in the upper pork samples. Two different signals are present. Fast decorrelation is observed around the water injection site and around the PFA injection site before tissue fixing has developed. Then, at 40 minutes post-injection, a large increase in τ_c is seen around the PFA injection site, indicative of tissue stiffening.

in the context of τ_c. At this stage, the PFA/DAPI solution was not yet incorporated; our injected solutions only consisted of PFA and phosphate buffer solution (PBS). We inject PFA solution into a pork fillet sample, and as a control, we also inject water into another pork fillet sample, which should cause no tissue stiffening. Fillet cuts were used, in particular, due to the orientation of the muscle fibres, which helped the injections localise in a spot around the injection site.

Figure 5.3 shows results for the above scheme. (a) shows columns of intensity and DCS images for the control water injection measurements, and (b) shows the equivalent for the PFA injections. For both PFA and water injection measurements, three acquisitions were made each at different time points: 1) before any injections, 2) just after injections and 3) 40 minutes post-injection, where tissue stiffening is seen for the PFA-injected pork sample. Four samples were used in total. A test and control sample for both water and PFA injections informed us of how the pork sample would naturally change over time

according to τ_c.

The four samples looked alike before the injections and were largely homogeneous in τ_c. At the 0 minutes post-injection time point, a small indent in the pork sample can be seen in the colour images and in the DCS τ_c colour maps, a dark spot in both water and PFA samples. However, at the 40-minute post-injection time, a hot spot is seen in the PFA sample's τ_c colour map, whereas the water sample's colour map still shows a dim dark spot. Thus, DCS has found two signals, one related to a fluid being in the sample and the other due to stiffening. In the 0-mins post-injection case, DCS has picked up water and unfixed PFA solution in the pork samples, which makes the speckle decorrelation faster and τ_c shorter. In the 40-mins post-injection case, the PFA has fixed a portion of the tissue on the pork sample, evident as slower speckle decorrelation and larger τ_c. Regarding the intensity image, a subtle change in colour is seen in the PFA sample's colour image. Lastly, in all analyses, there is an increase in τ_c at the edges of each pork sample that can be explained by sample drying, which would make the tissue stiffer [209].

5.4 PFA and DAPI Injections

Now that we have seen that DCS is sensitive to sample stiffness changes induced by PFA, we work towards creating a reference that will tell us where the PFA injection has localised. As previously described, we experimented with DAPI, a fluorescent dye that, when stimulated by 350 nm UV light, emitted $\sim$ 450 nm visible light. DAPI is a fluorescent dye used conventionally for cell imaging as it binds to DNA. However, for our case, we merely want a solution of PFA and DAPI to inject into a sample to confirm what parts of the tissue have been fixed.

In this experiment, we also investigate the effect of specular reflections on the DCS imaging scheme. A polariser could potentially be used to either select or reduce the light that has been reflected from the surface. therefore, it may be possible to differentiate between the sample's surface and its less superficial layers.

Figure 5.4 shows results for the above experiment in a similar arrangement as the previous experiment's results. Reference intensity colour images (portrayed in (a)) again show a slight discolouration in the pork at the injection site in the upper portion of the pork sample. (b) the reference fluorescent image and a bright fluorescent region around the injection site. (c-d) show respectively the τ_c colourmaps with and without contributions from specular reflections. The DCS images with no specular reflection removal in (c) both suffer from a stark contrast between pixels, with some pixels exhibiting very long τ_c due to specular reflections of light off the sample. Specular reflections, as opposed to diffuse

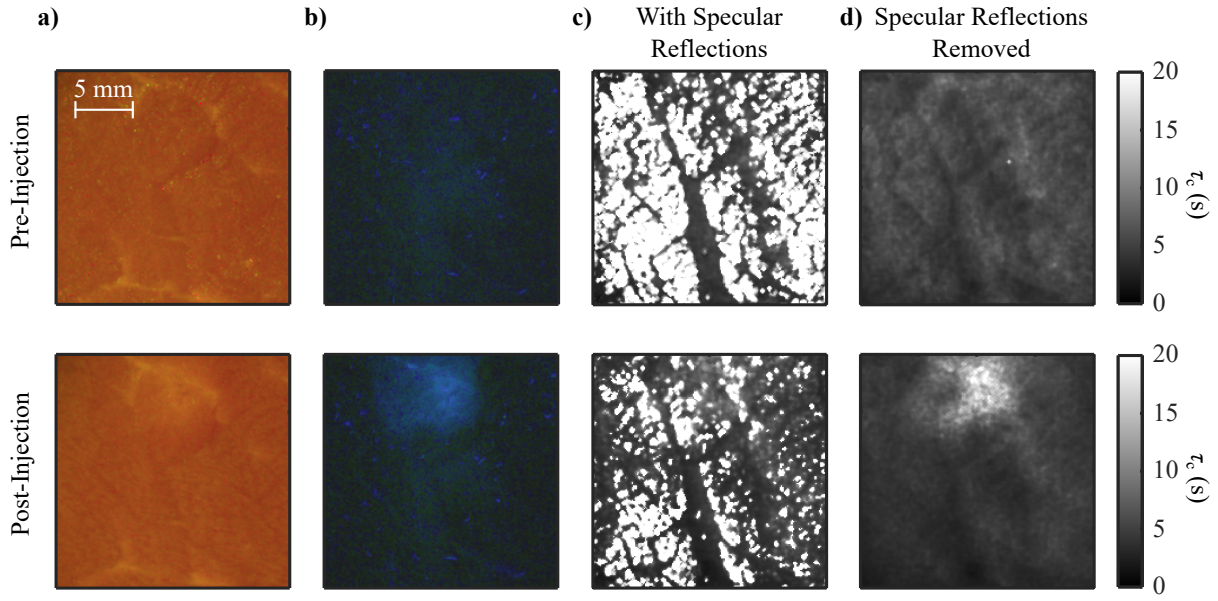

Figure 5.4: **DCS imaging analysis of PFA/DAPI injections on pork samples with and without specular reflections.** a) The colour intensity images of the pork sample before and after PFA/DAPI injection. b) Fluorescent images of the pork samples under UB (350 nm) illumination that shows where the stiffening has localised to. c) τ_c colourmaps obtained by imaging the surface of the pork without a polariser. There are many long τ_c pixels due to specular reflections of light. d) τ_c colour maps obtained with a polariser placed before the camera objective, where the specular reflections are reduced and thus long τ_c pixel artefacts are removed. With the polarised setup, the τ_c colour map image quality is better now and the stiffened tissue signal is more easily seen.

reflections, only incur a single scattering event, have a tight k-vector distribution, and a long τ_c. Despite the specular reflection artefacts, it is possible to make out a faint signal of the fixed tissue in the post-injection τ_c colour map. Converse to the previous results, the DCS image post-injection suffers less specular artefacts than the pre-injection image, which is most likely due to drying of the material and less specular reflections from the sample. A method to inhibit specular reflections is to polarise the collected light. (d) shows τ_c colourmaps of the polarised configuration pre- and post-injection. The fixed tissue signal is much clearer and well correlated with the fluorescence reference image.

The fluorescent DAPI dye provides a good ground truth measurement of the PFA spreading and fixing. The DCS imaging apparatus is subject to specular reflection artefacts, which are simply amended by polarising the collected light. To obtain a depth-resolved measurement, a more thorough approach that utilises illumination wavelengths from blue to near-infrared light could be a better means of depth-sensitive tissue stiffness mapping.

5.5 Imaging a brain tumour proxy

Now, with preliminary measurements done on lamb brain and pork fillet samples and a suitable fixed tissue ground truth made, the next step is to perform a measurement on a brain slice, slowly bringing the measurement constraints closer to those of a real and live brain measurement. We extract a whole mouse brain and measure it pre- and post-injection of the PFA/DAPI solution like with the previous experiment with a polariser to remove specular reflections. This measurement is done immediately after extracting the brain from a live mouse.

Intensity colour images, fluorescent images, and τ_c colourmaps for pre- and post-injection time points are shown respectively in Figure 5.5(a-c). The DCS images in (c) were made from a speckle series with a five-minute duration. There is good agreement between the τ_c colour map and the fluorescent image post-injection. Moreover, there is no clear sign or discolouration of the brain in the intensity colour image, proving that DCS can capture stiffness changes in the brain invisible to the human eye or standard intensity imaging means.

The τ_c colourmap shown in (c) is not uniform. As can be seen in the bottom-right of both the pre-injection and post-injection images, there is a hot region. To prove that this is not a consequence of the PFA/DAPI injection, I show a difference image between the post- and pre-injection τ_c colourmaps in Figure 5.5(d). Specifically, the difference image shows that the only change in the τ_c colourmaps resides in and around the injection site and that the stiffened tissue region exhibits a change of 0.5 s equivalent to a doubling of the fresh and non-fixed τ_c.

5.6 Nearest Neighbour Pixel Stacking to Decrease Acquisition Time

The previous section shows our DCS imaging method working for an ex vivo brain sample, where the injection site had a mean τ_c of 0.902 ± 0.003, indicating that this acquisition could have been done over a two-minute period in reference to our findings shown in Chapter 3.4. Scaling the approach to be operable in real-time would make the technique much more medically relevant. In this case, I experimented with the pixel stacking procedure described in Figure 3.12 to reduce the acquisition time needed to resolve the tumour proxy.

The same speckle series of the brain post-injection is used for this analysis, which cuts the speckle series at 30 and 10 s time points. The DCS image is then built as previously done

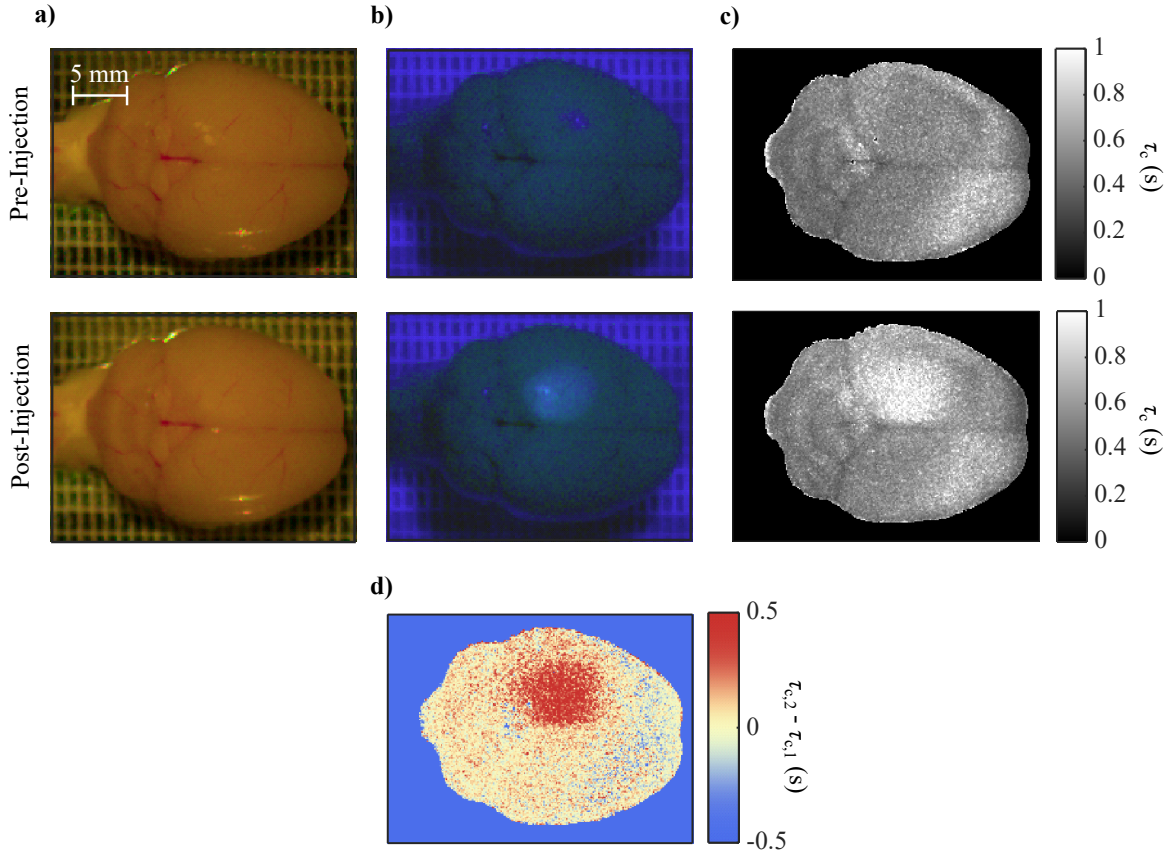

Figure 5.5: **DCS imaging of PFA/DAPI tumour proxy.** a) Colour images of the brain pre-injection of PFA/DAPI solution (top) and post-injection (bottom). Any presence of PFA/DAPI solution in the brain slice is not noticeable. b) Corresponding fluorescence images with UV light stimulation. DAPI fluoresces to show the spread of PFA at the injection site and is used as a ground truth of the tumour proxy's location. c) τ_c colourmaps with a hot spot of long τ_c at the injection site. These images were segmented such that τ_c of pixels outside the brain were set transparent. d) A difference image between the post- and pre-injection τ_c colourmaps plotted with a diverging colour map, showing the brain area modified by PFA fixing.

but for the shorter acquisition times shown in Figure 5.6(a-b). Next, DCS image generation is repeated, this time stacking time series from regions of three-by-three neighbouring pixels before g_2 computation and pixel-wise τ_c finding. The DCS images made using the pixel stacking approach are shown in (c-d).

In this brain example, the pixel-stacking approach has increased the signal from the tumour region compared to the regular and otherwise non-pixel-stacked approach. However, they appear noisy due to stacking time series of differing mean intensities, making it difficult to visually segment the tumour. Capturing a larger and more magnified brain image would provide more pixels per area and make segmenting the tumour proxy by eye easier. However, greater resolution would make the g_2 computation more demanding and thus, a trade-off between image resolution and computer capabilities must be met. In Chapter 6,

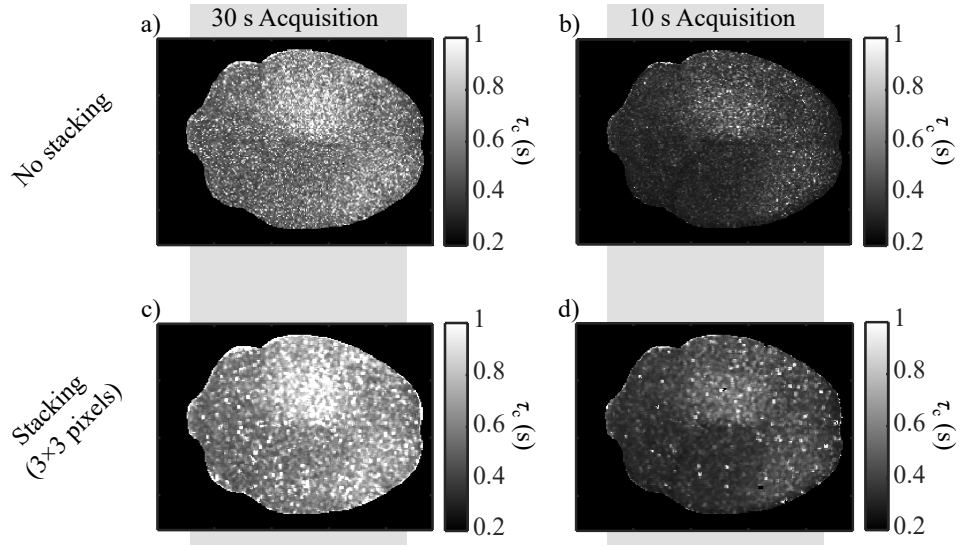

Figure 5.6: **Speeding up the brain DCS acquisition with the pixel stacking approach.** (a-b) DCS images of the brain and tumour proxy acquired over 30 and 10 s short acquisitions. (c-d) The corresponding DCS images with conserved pixel stacking applied over 3×3 pixel neighbourhoods before g_2 computation. The signal of the tumour is visually better for the stacking approaches.

additional techniques other than the stacked DCS method will be discussed, as well as a numerical analysis of the tumour's SNR.

5.7 DCS and Nanoindenter Comparisons

Now that we have shown that our DCS technique works on ex vivo and fresh mouse brains, the next step is to compare DCS measurements with a mechanical rheometer device, such as the nanoindenter used in the previous chapter. In doing this, we may gauge the sensitivity of the DCS device compared to a current mechanical device.

Nanoindenter measurements of effective Young's modulus were performed on fresh and fixed pork fillet and mouse brain slices. For this, the samples had to be prepared flat so that the nanoindenter probe could scan the surface of the slices without damaging the probe. Moreover, samples were submerged in PBS during nanoindentation scans for ease of measurement. Therefore, whole brain samples were not viable for measurement and had to instead be cut into slices like in Chapter 4 with a vibratome. The vibratome was not required for the pork fillet samples, which were cut by hand. Pork fillet samples were very uniform, and a fifty-point matrix scan of E was performed on a pork fillet sample before PFA and twenty minutes after PFA injection. Since mouse brain samples were less homogeneous, scans were only performed on the hippocampus of the mouse brain slices like in Chapter 4.

Samples from the same pork fillet were used in both DCS and nanoindentation measurements, and thus, only one fresh and one fixed sample of pork were analysed. However, the mouse brains were less stable, and due to the long measurement time (multiple hours) of the nanoindenter, the fresh brain slices were no longer viable after measurement. We measured seven fresh brains, two of which were entirely new samples, and the other five were the same control-WT and control-tg37 samples used in the previous chapter. As for fixed brain measurements, we used new brain samples. The fixed brains were much more stable over time, and we found that we needed fewer samples to achieve converging results. Two fixed brains were measured mechanically.

Fresh and fixed pork and mouse brain slice samples were remeasured with the DCS setup whilst submerged in PBS solution to keep DCS measurements consistent with nanoindenter measurements. In the case of the pork, DCS measurements were done as previously, where an acquisition was performed before and after PFA injection. We opted for a more controlled approach for the brains due to their heterogeneity. The mouse brains were first imaged fresh and then bathed in PFA to fix for one day before another measurement round. The DCS measurements were much quicker than the nanoindenter measurements, and since this DCS measurements could be performed longitudinally, we only measured two brain samples. In post-processing, segments of fixed tissue could be made with reference to the fluorescent images of the samples, and τ_c statistics pulled from pixels in those segments. For example, these segments refer to either the injection sites in the pork or the hippocampus of the mouse brains, as shown by Figure 4.5 in the previous chapter.

Figure 5.7 presents box plots of both τ_c and $E_{\text{effective}}$ measurements on the mouse and pork samples. Since we were measuring both pork and mouse brain samples, we used $E_{\text{effective}}$ instead of E, as both materials may have different ν. t-tests showed the large statistical significance of similar values between fresh and fixed samples of both nanoindentation and DCS experiments. In this respect, both measurements protocols have comparable sensitivity to the change in stiffness, however, the DCS-based method is considerably easier and quicker to perform. Moreover, the DCS-based method also offers many more data points to consider, as one performs a snapshot of the material as opposed to needing to scan with the mechanical nanoindenter approach. This, in turn, may give less error in the measurement, as shown in Table 5.1, which is, of course, dependent on the camera resolution and imaging objective.

One interesting difference between the two techniques is seen when comparing the fixed brain and fresh pork measurements. Regarding the nanoindenter, both media are effectively equivalent in E, as shown in Table 5.1. However, τ_c measurements can differentiate between them, where the fixed brain measures longer τ_c than the fresh pork. Thus, current data suggests that DCS is sensitive to more than just the stiffness of the tissue. Of course,

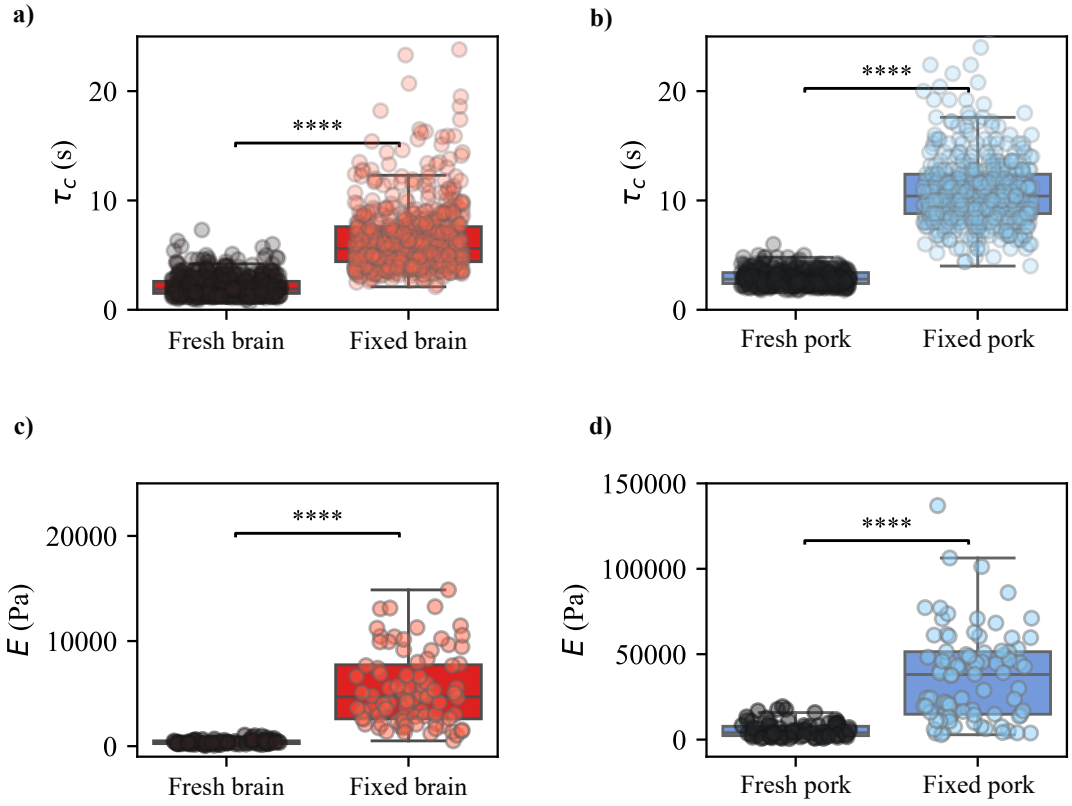

Figure 5.7: **DCS imaging τ_c and nanoindenter E comparisons.** a) Box plots of fresh brain vs fixed brain τ_c. b) Box plots of fresh pork vs fixed pork τ_c. c) Box plots of fresh brain vs fixed brain E. d) Box plots of fresh pork vs fixed pork E. Welch's t-test p-values are annotated on each plot. Individual circles refer to either pixels of the DCS measurement or scan points of the nanoindenter. **** corresponds to a p-value less than 0.0001. The four box plots show that both measurement schemes (DCS and nanoindentation) have similar sensitivities in detecting tissue stiffening.

by eye, pork fillet and mouse brain are noticeably different and have different morphologies. Moreover, we have not considered the viscous component, otherwise known as the loss modulus, of the samples, which would require DMA to be measured. A future DMA experiment that compares the viscous and elastic components of the sample to its τ_c would give more insight into what exactly the optical measurement is probing.

The primary purpose of performing nanoindenter measurements on the brain and pork samples was to determine if the relative differences in fixed and unfixed tissue reflect typical stiffness differences seen in the literature between healthy and tumour tissue. Studies have been undertaken to measure the differences in stiffness between tumour and healthy tissues [41, 44, 210], but each has done so through different tools, for example through MRE, shear rheometers, or nanoindenters, and there is some discrepancy in their stiffness measurements. The discrepancy between different measurement tools has been more formally studied in [211], who compared AFM to MRE measurements. One major differ-

	Fresh brain	Fixed brain	Fresh pork	Fixed pork
μ_{τ_c}	2.18	6.46	2.91	10.70
SE_{τ_c}	0.012	0.38	0.010	0.047
$\%e_{\tau_c}$	0.53	0.60	0.36	0.43
μ_E	390	5400	5600	39,000
SE_E	25	390	480	3500
$\%e_E$	6.3	7.1	8.5	9.0

Table 5.1: **DCS imaging and nanoindenter comparisons.** Mean, standard error, and percentage standard error values for τ_c and E brain and pork measurements (all rounded to 2 significant figures).

ence between the two schemes is that the former is done ex vivo and the latter is done in vivo, where there are factors such as intracranial pressure to consider that may effect tissue stiffess. Since our technique is yet another new technique, it is more beneficial to compare relative differences between tumour and healthy tissue as opposed to raw stiffness measurements, as we did in the previous chapter for neurodegenerated and healthy samples.

Comparing the brain DCS measurements in (a) and the nanoindenter measurements in (c), our DCS technique can differentiate between tissues of respectively 500 Pa from 5000 Pa. There are several articles on real tumours and healthy brain tissue measurements to which we may compare our technique. [41] et al. performed AFM nanoindentations on glioblastomas and meningiomas against normal-appearing white matter and found up to an order of magnitude of difference in their E measurements, which is within the capabilities of our device. However, Huston et al. [210] performed MRE on meningiomas and gliomas, which differed by at least a factor of 4 compared to healthy tissue. In other cases, the distinction between tumour and healthy tissue is more blurred, where E, G measurements overlap [44]. In any case, there is evidence that the method can segment real tumours from healthy tissue, and future work can be dedicated to testing the technique on real tumour tissue. This future work is further discussed in Chapter 7.

5.8 Speckle Size Analysis

As we have discussed previously in Section 3.5, the speckle size is an important experimental parameter for accurately estimating τ_c. Since the pixel-wise g_2 computation approach uses the indexing approach (3.25) to find τ_c, it is not as robust as the fitting approach when there are multiple speckles contained in a single pixel due to the loss of speckle contrast. It is therefore useful to know that the speckle size is at least as large as 1 speckle

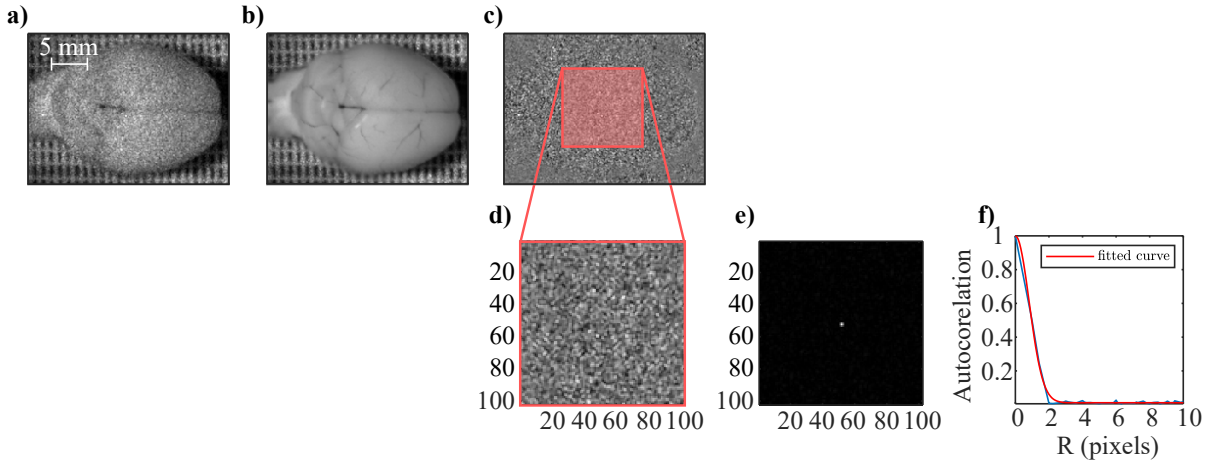

Figure 5.8: **Speckle size analysis of a brain DCS image.** a) A single frame of mouse brain (Figure 5.5 speckle series. b) The mean along the time dimension of the speckle series. c) An underlying speckle of the brain, which is the single frame of (a) minus the mean speckle image from (b). d) A centred ROI of the underlying speckle. e) A 2D spectrum of (d) computed by cross-correlation of the underlying speckle. f) A radial profile of (e) computed by radially averaging its spectrum. A Gaussian fit in red is fitted to the profile to determine the speckle size, which was $\sim$ 2 pixels. The algorithm [203] was used to calculate the speckle size.

per pixel.

The speckle pattern obtained with this new DCS approach comprises an image of the sample and underlying speckle. Measurements for speckle size use a cross-correlation approach [203] that will not work if there is structure to the speckle. For example, in our case, there is a speckle pattern and an image of a brain sample. To separate the image of the brain sample from the speckle series and obtain the underlying speckle, the mean speckle pattern across time is subtracted from each speckle series frame to obtain the underlying speckle. Once the underlying speckle is found, a cross-correlation may be applied to it, and the speckle size can be measured as the $1/e$ value of the resulting spectrum. This process is all shown in Figure 5.8 and resulted in a mean speckle size of 1.9207 ± 0.0011 pixels per speckle.

5.9 Imaging High-Stiffness Tissue

In this final section of this chapter, I would like to now detail a preliminary study, which implements our DCS technique on bone; the problem here is that bone is much stiffer than the previously measured brain and muscle samples and would mean very long acquisition times on the scale of many minutes are needed. A solution to the long acquisition time

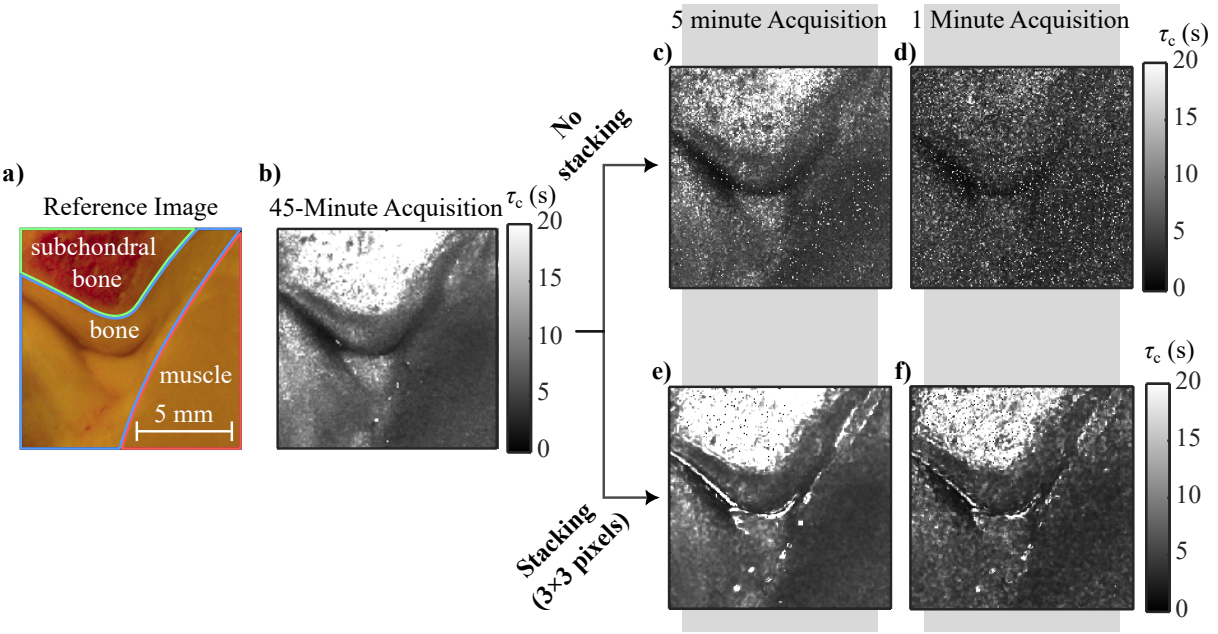

Figure 5.9: **Imaging slow dynamics and bone with DCS.** a) A reference image of a store-bought pork chop sample with distinct tissue types (subchondral bone, bone, muscle). b) A DCS image computed using a speckle pattern forty five minutes long. (c&d) DCS images made with speckle patterns five and one minutes in length. (e&f) corresponding DCS images to (c&d) but made now using the pixel stacking method before g_2 computation.

problem is the pixel stacking method detailed in Chapter 3.8.

This experiment involved the same apparatus used for the previous brain images, but the use of a PFA fixative was, of course, no longer necessary, as the purpose of the experiment was simply to show that bone could be imaged by the DCS technique. A pork chop sample was purchased from a local supermarket, and a section that included muscle and bone was chosen for measurement. The chosen section is shown in Figure 5.9(a), which includes text annotations of the different tissue types. A single long acquisition of forty-five minutes was then carried out, and the DCS image shown in Figure 5.9(b) was calculated. This acquisition time was chosen regarding the slowest decorrelating element, which we identified as high stiffness subchondral bone [119]. In this figure, each distinct tissue type can be segmented by eye, with the subchondral bone measuring the longest τ_c followed by the bone and finally the muscle, which was the softest of the tissues.

However, our DCS imaging approach will not be useful at such long acquisition times, and thus, I experiment below with the pixel stacking approach to speed up the acquisition. The forty-five-minute acquisition was trimmed at both the five-minute and one-minute acquisition time marks to directly compare the DCS image made using the dimensions-conserved pixel stacking method (3×3 nearest neighbour stacks) and the otherwise regular DCS imaging method. The resulting DCS images for both approaches are shown in Fig-

ure 5.9(c-f). (c-d) comprises the five-minute and one-minute acquisition time DCS images, respectively. Looking particularly at the subchondral bone region of the image, smaller τ_c are measured as the acquisition time shortens in line with the previous example shown in Chapter 3, as the τ_c is biased to smaller values for short acquisition times. The different regions may still be made out in the five-minute acquisition (c); however, in the one-minute acquisition (d), they can no longer be segmented. (e-f) comprises the equivalent acquisitions now with the pixel stacking method applied before g_2 processing. For the five-minute acquisition (e), there is now much more contrast between the regions as opposed to in (c), albeit with intensity-mixing artefacts present that were previously detailed in Chapter 3.8. Moreover, for the one-minute acquisition (f), the eye can now differentiate the different bone and muscle regions.

The acquisition time of DCS for bone imaging is substantially decreased when using the pixel stacking approach, meaning our DCS imaging method may be viable for bone stiffness-imaging applications. Further study into this application will require bone samples affected by osteoporosis and osteoarthritis.

5.10 Conclusions

DCS has been previously shown to be linearly correlated with tissue stiffness. Taking advantage of this relationship, we devised that a well-suited application of DCS would be for intraoperative tumour imaging. We made a DCS device that imaged the surface speckle emanating from a sample. The device was sensitive to a tumour proxy that had higher stiffness than its surrounding healthy tissue and was otherwise hidden from the human eye. The device is particularly adept at identifying relative stiffness differences in tissue, making it an intuitive and potential tool for surgeons during tumour removal operations.

Our new technique is, however, not without its drawbacks. In its current form, it requires long acquisition times and that the camera and tissue be kept still during acquisition. Therefore in the next chapter, I would like to explore ways to improve the measurement process of DCS. This next chapter will expand on improvements other than the pixel stacking method that was previously method. In particular, a convolutional neural network (CNN) and other speckle-based measurement schemes that could substitute DCS will be discussed.

CHAPTER 6

Further Improvements to Diffuse Correlation Spectroscopy

6.1 Introduction

The previous chapters show that DCS is useful for assessing two worldwide health conditions. However, DCS is not without its limitations. One particular issue that has repeatedly arisen throughout this thesis is DCS's need for long acquisition times. This issue restricts the medical applicability of our DCS imaging approach. We have found that DCS' need for long acquisition times is remedied slightly when using the pixel stacking method that was introduced in Chapter 3.4, but we have seen that this encounters boundary problems when two pixels of vastly different mean intensities are combined. In this case, it may also be useful to focus on other methods that can improve DCS' acquisition time.

6.1.1 Machine Learning

A CNN could be a potential solution to DCS' long acquisition time requirement. Specifically, a CNN that has sped up optical trap rheology experiments has recently been reported on [148]. The significance of this study is that optical trap rheology measurements study particle displacement time series and are thus very similar to the data obtained in DCS. The CNN is trained to map a viscosity measurement to a short time series. In this respect, the same CNN could be modified to learn an output τ_c to a short intensity time series and thereby decrease the acquisition time of DCS.

6.1.2 LCSI and SCOS

LSCI and SCOS discussed briefly in Chapter 2.3.2 are other computational imaging techniques that by-and-large use data of a similar structure to DCS and have evidence of sensitivity to tissue mechanics. Therefore, with small changes made to the post-processing of our data, speckle contrast imaging techniques could also prove beneficial.

6.2 Machine Learning DCS Model

My colleague Jack Radford initially created the supervised machine learning model I have adopted, described in [148]. In supervised learning, a model is trained to map between input data and an output label. In the above paper, a time series of x-y displacement of a particle suspended in an optical trap was mapped to viscosity measurements. The data structure here is very similar to our 1D intensity time series data, and we have modified the above model to map between intensity time series data and an output τ_c value. Our model consists of two convolutional layers and six dense layers. The convolutional layers aim to extract important features in the data through a series of convolutional filters. Each convolutional layer scans a set of filters, or kernels, over the input data and transforms it into a feature map. A CNN is a good choice for our experiment, as it focuses on local patterns in the data. They can recognise features in the time series data even if they were shifted; they are translationally invariant. This is useful for decorrelation data, as one cares about how quickly a signal changes with time, starting at an arbitrary time point [212]. This means that they can pick out features in the random time series data regardless of their location in the time series. The output feature maps of the convolutional layers were then flattened and passed through dense layers that decreased in size to finally a single layer and neuron, whose output is a τ_c prediction of the input time series.

Our DCS model is illustrated in Figure 6.1. Time series data is fed into the first convolutional layer, which consists of 32 kernels that are 10 frames wide. The second convolutional layer consists of 64 kernels and is 50 frames wide for the 1 s data and 100 frames wide for the 10 s data. It also incorporates stride lengths of 10 frames. This means that each kernel will skip 10 frames between convolution operations, downsampling the input and using multichanneling to minimise information loss [213]. Here, training of the model can be sped up, and its memory requirements are reduced. The following six layers were made heuristically by Jack Radford in the preceding paper [148]. I incorporated dropout regularisation in the dense layers during training. Dropout regularisation omits random neurons in the dense layers. This helps prevent overfitting by ensuring the neurons' weights are more evenly distributed, i.e., the network is less dependent on specific neurons.

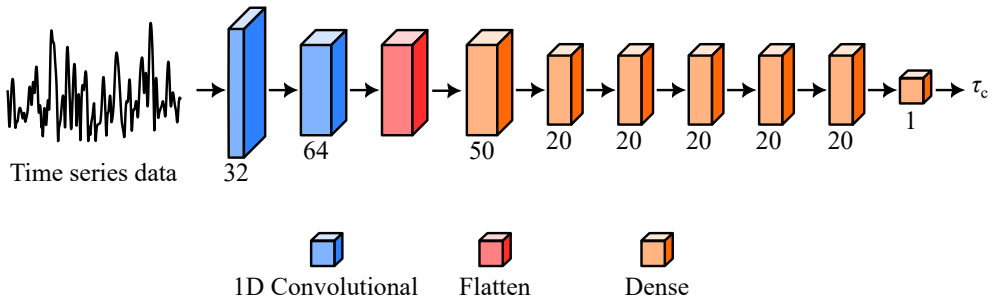

Figure 6.1: **ML model architecture.** An intensity time series is processed over two 1D convolutional layers, flattened, then fed through dense layers to finally a single output node representing τ_c in seconds. All convolutional and dense layers use a Leaky ReLu activation function of slope -0.3, except for the final dense layer, which uses a linear activation function. Kernel sizes and number of neurons are displayed for the convolutional layers and dense layers respectively.

Learning is achieved by minimising a loss function, which measures how far the model's predicted τ_c is to the true τ_c. Our model utilises the mean absolute percentage error as a loss function. Through training, the model will learn what weights in the model's layers best minimise the error between the predicted and true τ_c. Gradient descent is used to obtain the best weights for mapping a time series to the correct τ_c. For each training data batch, the gradient of the loss function with respect to the parameters is calculated, and the weights of each neuron are re-evaluated. This is repeated until a minimum (ideally, a global minimum) in the loss function is found. Aside from the number of epochs, learning rate and batch size are two important hyperparameters. Hyperparameters tune the learning process and are preset by the user. Learning rate refers to the step size that the model takes when performing gradient descent. Our model uses the Adam optimiser, which adjusts weight updates based on past updates (momentum) and adjusts the learning rate of each training parameter as the gradient changes [214]. For example, the learning rate may be decreased as the loss function's gradient approaches zero. Batch size refers to the number of training examples used in a single epoch.

The time series and their τ_c labels are split into training, validation, and testing sets. The purpose of the training set is to map the time series data to the correct τ_c value. The validation set is used to test the generalisability of the model. The data here is not used specifically for the model's learning but rather for checking that it is learning correctly. For example, if the model correctly maps time series data to τ_c for the training data but not for the validation data, this is a sign of overfitting. At this point, learning hyperparameters such as learning rate, batch size, and epochs may be changed. The test comprises completely unseen data and is used to assess the model's performance in an unbiased manner. The model's performance can be assessed by plotting a loss function

versus training iteration, or epoch, plot. Ideally, a small loss is obtained where the training and validation curves align. Our model uses a learning rate of 10^{-5}, a batch size of 256, and 200 training epochs [215]. The training was performed on a desktop with the following characteristics: Intel i9-10900X CPU (3.7 GHz), 256 GB RAM, and an NVIDIA GeForce RTX3090 with 24 GB memory. The Keras and TensorFlow packages were used.

6.3 Generating τ_c and Time Series Data

Simulated data was used to train our ML model. Previously, in Chapter 3.1, the simulation of speckle patterns for dynamic media was discussed. In this chapter, one of my motives is to decrease the acquisition time required to perform DCS measurements to make the technique more medically relevant for tissue with long relaxation times. Here, I perform CDA simulations to generate data for training our ML model. Ilya Starshynov originally made the CDA simulations I have used. I have added to Dr Starshynov's code to simulate how the Brownian motion of scatterers produces a temporally decorrelating speckles series, or more precisely, incorporated Equation. 3.13 into the simulations.

$64 \times 64 \times 200,000$ (x pixels, y pixels, frames) speckle patterns were created for a random scattering medium of $20 \times 20 \times 20$ arbitrary units of mean free path length of 17 and an optical depth of 1.2 were made for a frame rate of 2000 fps through CDA simulations. The initial frame rate here is arbitrary, as any time series could later be sampled to match the model's requirements. The CDA simulations are inefficient for dynamic speckle simulations, so we relied on upsampling the time series data to obtain a suitable range of time series and τ_c for training our ML model. The pipeline for generating data to train the ML model is shown in Figure 6.2. In (a), 200,000 time series and their corresponding τ_c values, measured by g_2, were generated using CDA simulations. The distribution of τ_c is approximately normal, with a mean of 0.11 s, where the variation arises from sampling statistics. Uniform data is required for training to ensure that the ML model's estimations are not biased towards particular τ_c values. To make the τ_c distribution uniform, as shown on the right of (a), and scale the time series and τ_c to timescales more comparable to real data, upsampling was performed on each time series. Here, upsampling simply linearly interpolates points between frames. It was performed with Matlab's resample function, which is contained in Matlab's Signal Processing Toolbox. In (b), I show the output τ_c as found through g_2 calculation, plotted against the upsampling factor u. They have a linear dependence. Therefore, it is viable for us to create new time series data with larger τ_c by upsampling the original CDA simulated time series data. Examples of time series and corresponding upsampling factors are shown in (c). It can be seen by eye that upsampled time series with larger u have a longer time scale decorrelation than smaller u time series,

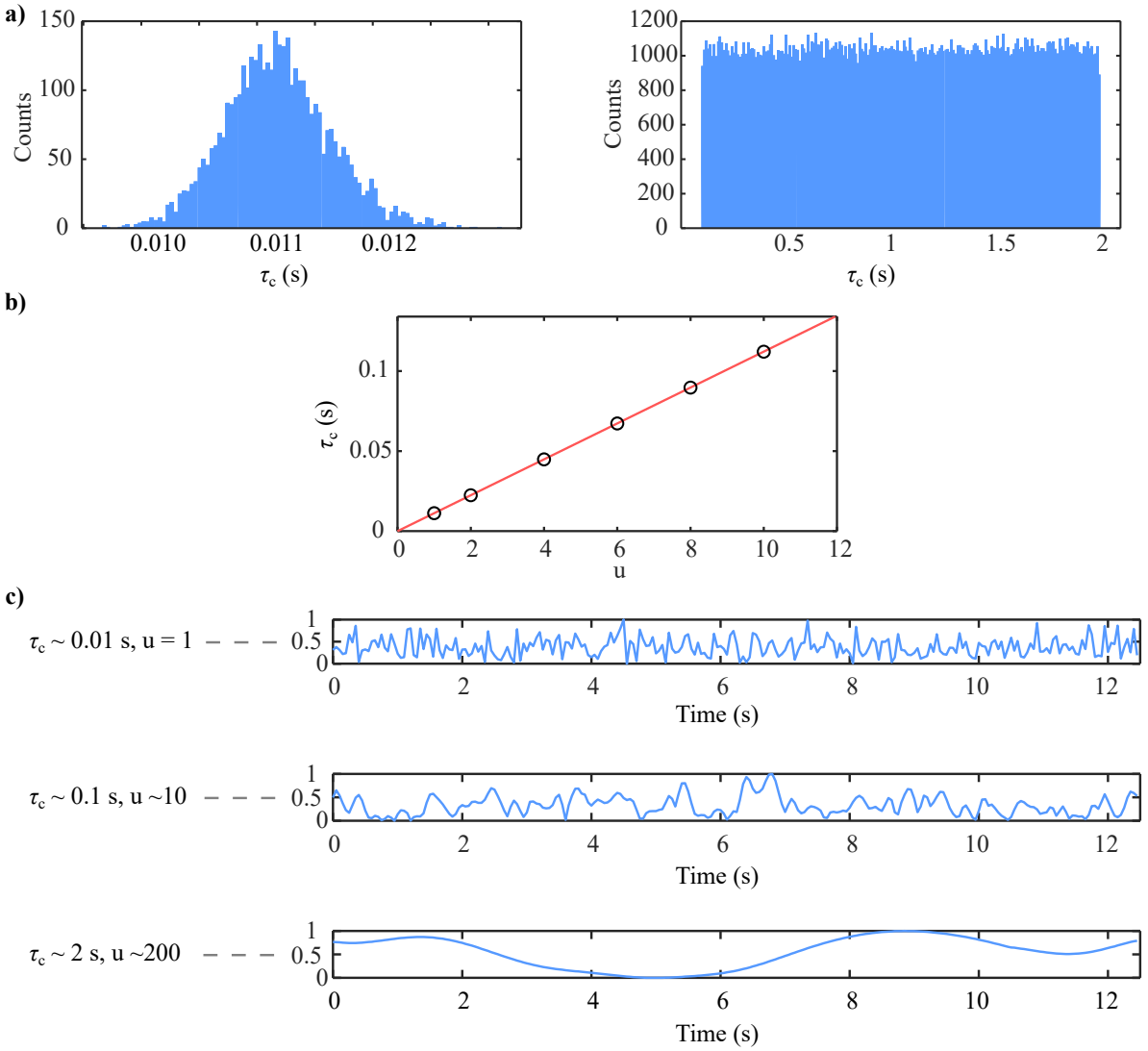

Figure 6.2: **Pipeline for upsampling time series and τ_c data.** a) On the left is a histogram of τ_c values determined by applying the g_2 function to CDA simulated time series (respective time series not shown here). On the right is a histogram of τ_c values made by upsampling the time series and τ_c of the previous histogram. This histogram is cropped between 0.2 and 2 s to make a uniform distribution, which is ideal for training our ML model for the mouse brain tumour proxy data. b) A plot of τ_c determined by g_2 calculation, against upsampling factor u. The linear dependence indicates that one may upsample a time series to obtain another with a longer decorrelation. c) Three examples of intensity time series are shown with corresponding τ_c and upsampling factors, u on the left. A large upsampling factor corresponds to a slowly decorrelating time series.

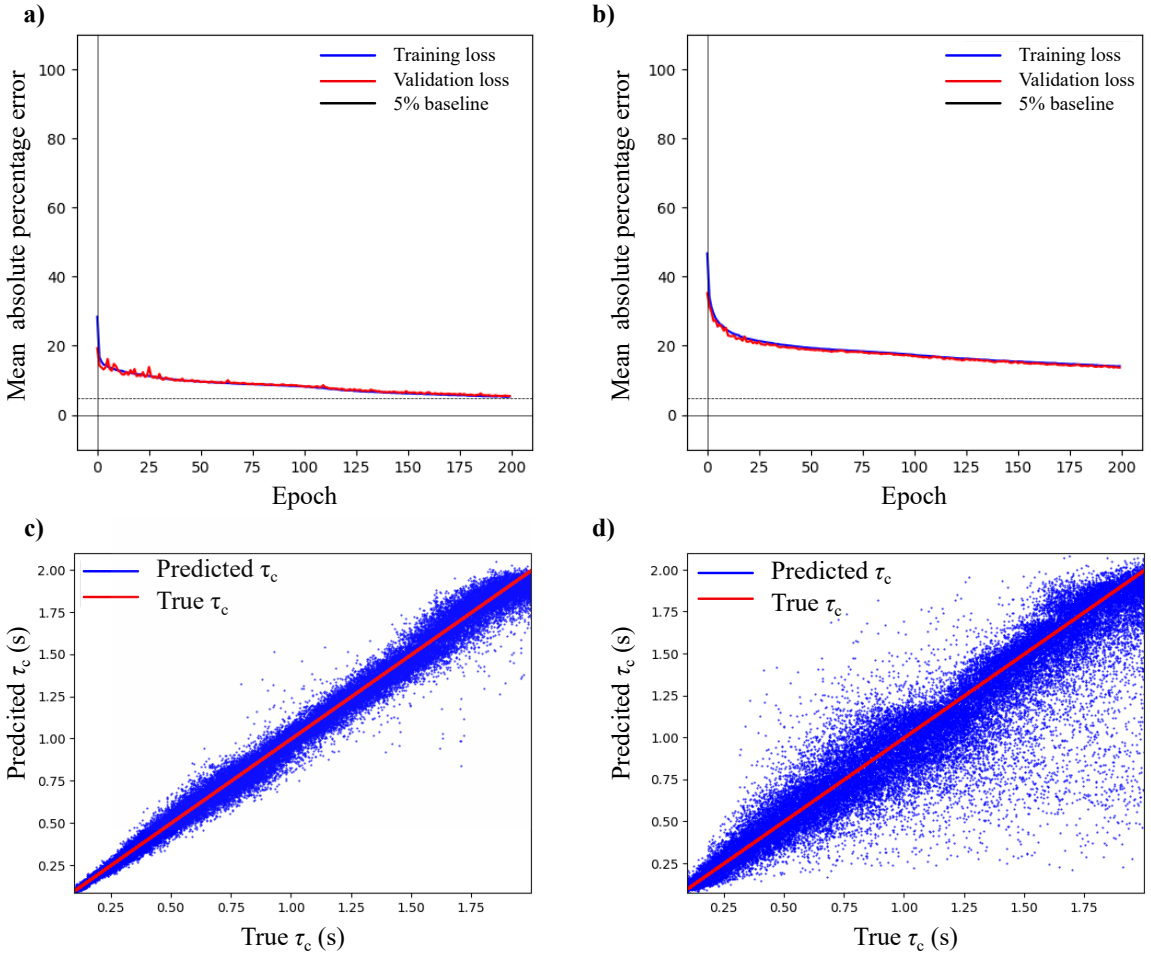

Figure 6.3: **ML model training and testing**. (a & b) Mean absolute percentage error vs training epochs for 10 s data (a) and 1 s data (b). A horizontal dashed line shows a 5% baseline in the loss.(c & d) Predicted τ_c vs true τ_c for unseen 10 s data (c) and 1 s data (d).

but for reference, τ_c and u are also quoted on the left.

6.4 ML Training and Testing on Simulated Data

Two models were trained. One model was trained on 1 s acquisition time series data, and the second was trained on 10 s acquisition time data. Both sets of time series data had a frame rate of 100 fps, similar to the DCS brain with tumour proxy data. Hyper-parameters of both models were the same: the batch size was 256, the number of epochs was 200, and the learning rate was 10^{-5}. The data was split into training, validation, and testing sets. 80% of the data was used for training and validation, and the final 20% was used for testing.

Figure 6.3(a-b) show mean absolute percentage error vs epoch plots for 10 and 1 s acqui-

sition time data. (c-d) show predictions made of the model made on the test set for also the 10 and 1 s acquisition time datasets. The 10 s data converged faster than the 1 s data with considerably less error (5% vs 17% after 200 epochs) in its predictions on the test set.

6.5 Applying the ML-DCS Model to Previous Laboratory Data

Now with the ML-DCS model trained on 10 and 1 s data, it can be applied to predict τ_c of real experimental data. For the model's demonstration, I again use mouse brain data with the PFA stiffened tumour proxy, as this data is the closest form of current data to real tumour data and, thus, the most medically relevant.

Since real experimental data is noisy, it first had to be filtered before being input into the ML-DCS model to match it to the simulated data used for training the model. This was achieved by applying a lowpass Butterworth filter of order 1 and a cutoff frequency of 5 Hz to each 100 fps time series.

Figure 6.4(a) shows again a fluorescent ground truth of our tumour proxy. I attach a 2-minute acquisition DCS image as another form of ground truth, with τ_c at the threshold. Then (c) shows comparisons of all the DCS techniques so far for both 10 and 1 s acquisition times. The three techniques are the standard g_2 calculation approach, conserved nearest neighbour pixel stacking prior to g_2, and lastly, the ML-DCS model, which completely substitutes g_2 calculation altogether. Comparisons of the nearest neighbour stacking versus the standard g_2 approach have previously been discussed, so we turn our attention now towards the new results produced by the ML-DCS model, which for both 10 and 1 s acquisitions is less noisy than the previous g_2 methods. The biggest result from the ML-DCS model, however, is that it is able to image the tumour proxy with only a 1 s acquisition and promotes our DCS technique towards a medically relevant intraoperative imaging device, as long acquisition times may hinder the performance of surgeons during operations.

However, the ML-DCS model is not perfect. Particularly, when comparing both the 10 and 1 s acquisitions of the ML-DCS model, it is clear by eye that its τ_c predictions are underestimated when compared to the 2-minute ground truth DCS image (b). More work is required to understand why this is; however, the most likely culprit is the mismatch between simulated training data and denoised laboratory test data. A solution could be to instead train the ML-DCS model on real data acquired with the same CMOS camera used to produce the previous DCS images. Otherwise, the opposite approach would be to

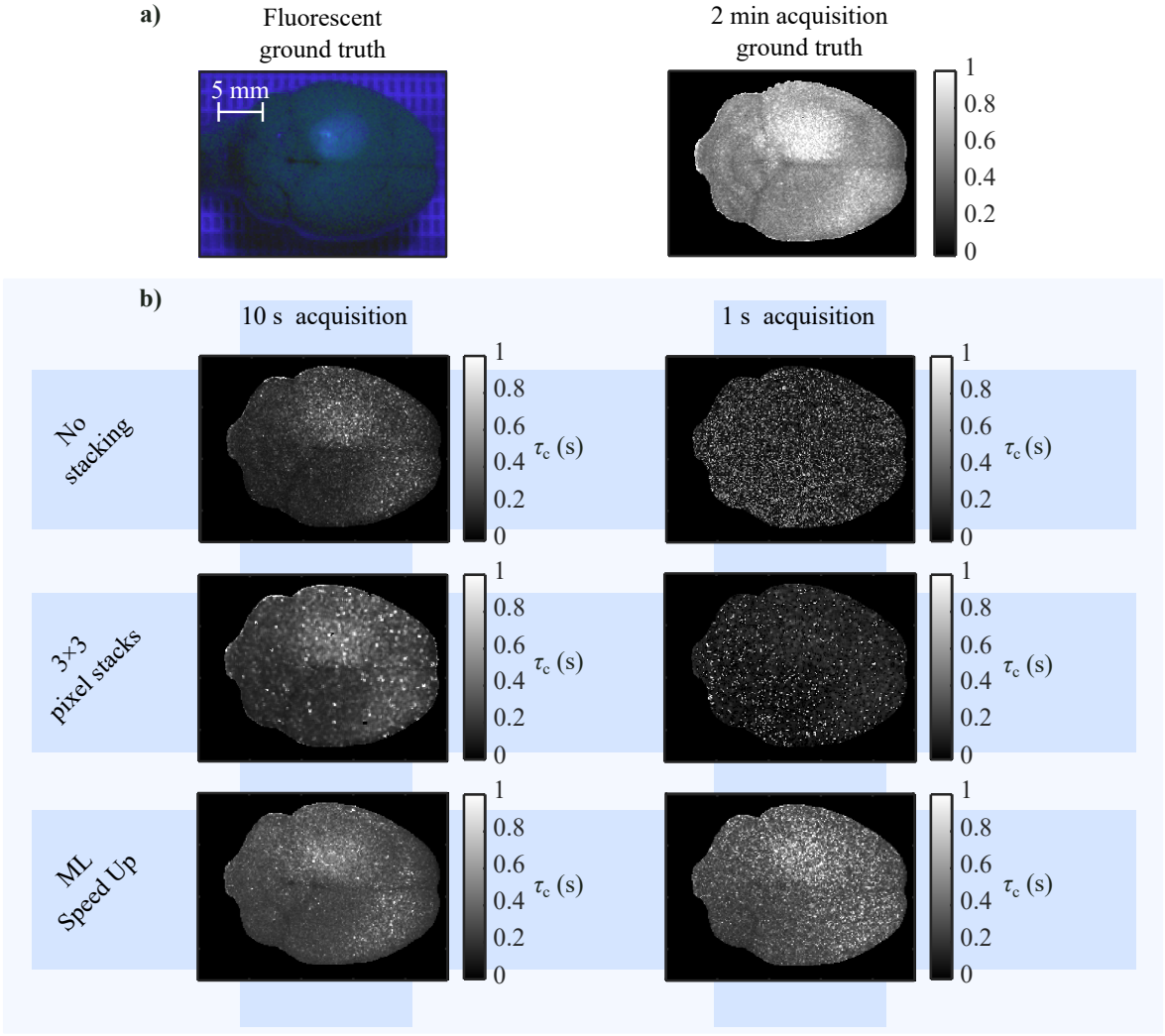

Figure 6.4: **ML results on mouse brain tumour proxy data.** (a) On the left is a fluorescent ground truth of the fixed region tumour proxy of the brain, and on the right is the τ_c colour map of the mouse brain acquired over a two-minute acquisition. Both these images were previously shown in Figure 5.5 and are used for reference here. b) Comparisons of the three approaches: no stacking, 3×3 conserverd nearest neighbourhood stacking prior to g_2, and using our ML model as a substitute for the g_2 processing. The comparisons are made for ten (left) and one-second (right) acquisitions, where our ML approach visually shows clear improvements in SNR and tumour proxy segmentation in the 1 s acquisition time regime. NaN values are set to black.

add noise to the simulated data before training.

Nonetheless, the strength of the technique is for segmentation purposes, which only needs to measure a relative difference between the tumour and healthy tissue. For example, if an MRI image is used prior to operation, a surgeon already knows the location of the tumour, and this DCS imaging tool is simply to aid them during surgery as opposed to characterise or diagnose tumours.

6.6 Speckle Contrast Imaging of Mouse Brain and Tumour Model

6.6.1 Methods

There are broadly two ways to calculate the speckle contrast. For the first approach, the speckle contrast is calculated spatially over a single image through the below equation,

$$K_s = \frac{\sigma_s}{\langle I_s \rangle}. \tag{6.1}$$

Here, the spatial contrast K_s is found for each pixel using a sliding window denoted by s, with a user-defined size typically in the order of a few pixels. The spatial contrast is a function of camera exposure time and has been shown to correlate with the g_2 function used in DCS measurements [96]. When the camera exposure time T_{exp} is greater than τ_c, then K_s essentially measures the blurring of the speckle and thus can be used to measure the dynamics of a scattering medium. For example, a $K_s = 1$ is associated with no blurring of the speckle and, therefore, no motion of the scattering medium, whereas $K_s = 0$ indicates a great degree of blurring of the speckle and a highly dynamic scattering medium. We shall call the above approach the spatial contrast method. The second method is to calculate the temporal contrast, which is written,

$$K_t(x, y) = \frac{\sigma_{x,y}}{\langle I_{x,y} \rangle}. \tag{6.2}$$

This time, K_t is calculated over a temporal window for each x and y pixel, which has been shown to have improvements in spatial resolution over the spatial contrast method since no spatial averaging is performed [97, 216].

Conventional LSCI and SCOS are used for blood flow applications and operate in a regime where camera exposure time T is greater than τ_c. In this regime, K measures the speckle blurring and is linearly related to τ_c. In our situation, however, we are interested in slow tissue mechanics, which occur at timescales on the order of seconds ($T_{\text{exp}} < \tau_c$). In this regime, it is unclear what effect T_{exp} will have on K, as successive speckle frames will be correlated. I will, therefore, investigate both regimes below.

6.6.2 Results

The speckle contrast results are summarised in Figure 6.5. The fixed tumour proxy's fluorescent ground truth image is again shown in (a) for reference. (b) shows results from

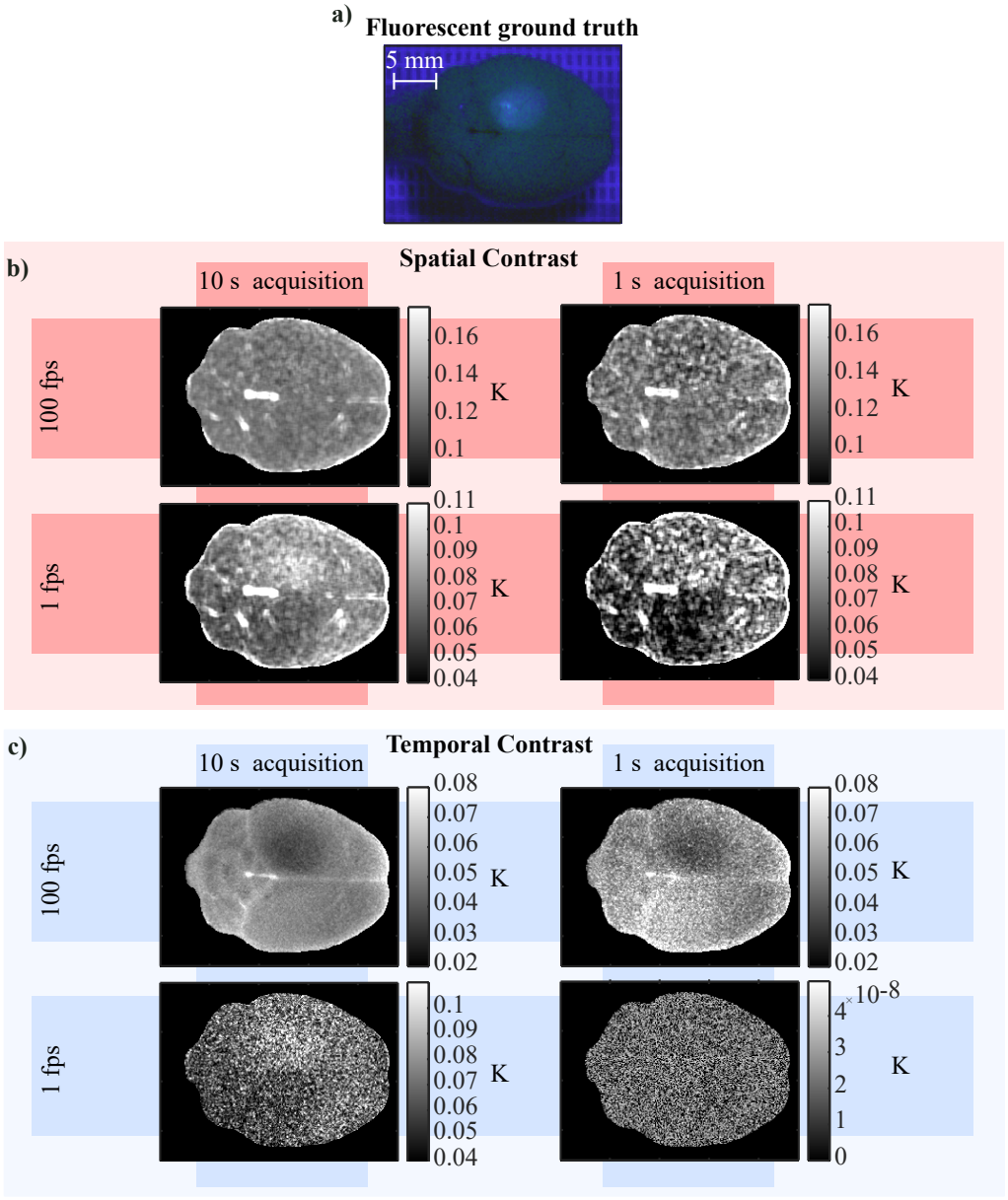

Figure 6.5: **Speckle contrast of mouse brain tumour proxy data.** a) The previously shown fluorescent ground truth of the fixative on the mouse brain. b) Results for 10 and 1 s acquisition times and 100 and 1 fps camera frame rates for the spatial contrast implementation. c) The corresponding images for the temporal contrast implementation. The spatial contrast approach gives a clearer image for low frame rates on the order of τ_c, whereas the temporal contrast approach gives clearer results for frame rates shorter than τ_c. NaN values in all images have been set to black.

the spatial contrast scheme, where rows and columns indicate the frame rate (100 and 10 fps) and the data's acquisition time (10 and 1 s), respectively. (c) shows the same format of results but for the temporal contrast scheme. Specifically, comparing the abilities of both schemes to segment the tumour proxy, it is clear that the spatial contrast scheme performs better at lower frame rates and the temporal scheme at higher frame rates. The temporal scheme appears to perform the best segmentation of the tumour proxy. It

Imaging methods	10 s acquisition			1 s acquisition		
	μ_{sig}	σ_{sig}	|SNR|	μ_{sig}	σ_{sig}	|SNR|
DCS	0.20	0.19	1.03	-0.03	0.31	0.08
Stacked DCS	0.24	0.16	1.56	0.033	0.23	0.14
ML-DCS	0.18	0.15	1.22	0.20	0.32	0.63
Spatial speckle contrast (1 fps)	0.021	0.013	1.56	0.028	0.024	1.18
Temporal speckle contrast (100 fps)	-0.0094	0.0028	3.34	-0.019	0.011	1.66

Table 6.1: **Comparison of tumour imaging methods.** The sig subscript refers to tumour signal (values of the tumour ROI minus the healthy ROI, where the ROIs are defined as previously in Figure 6.6). For each imaging technique, the signal's mean μ_{sig}, standard deviation σ_{sig}, and SNR $= \mu_{sig}/\sigma_{sig}$ are shown. All Mean and standard deviation values are rounded to 2 significant figures and SNR to 2 decimal places.

furthermore seems to be visually better at tumour segmentation than the ML-DCS model at both acquisition times. Therefore, the temporal contrast method is very promising for real tumour segmentation.

Table 6.1 compares the signal and SNR of the five imaging methods discussed. The 100 fps spatial contrast and the 1 fps temporal contrast schemes were not included in analysis here due to their poor visual segmentation of the tumour. For 10 s acquisitions, all techniques except the regular DCS approach have an SNR > 1. For the 1 s acquisitions, the speckle contrast imaging schemes outperform DCS and the ML-DCS model, with SNRs at least a factor of 2 above that of DCS. Although there is a hot spot at the tumour region of interest (ROI) in the 1 s ML-DCS image from Figure 6.4(b), its SNR < 1. Its tumour signal is noisy, which makes it more difficult to visually segment the tumour than the speckle contrast methods. Out of all the techniques, the temporal contrast method performed the best in terms of SNR for both 10 and 1 s acquisition times.

When comparing the temporal contrast to the spatial contrast results, one interesting aspect of the results is that the tumour signal 'flips'. In the spatial contrast scheme for slow frame rates, the contrast signal is as one would intuitively expect when performing LSCI/SCOS, whereby the contrast of the stiffened tissue is increased. However, the stiffened tissue's contrast is reduced in the temporal contrast scheme for fast frame rates.

6.6.3 Analysing the Flipped Speckle Contrast Signal

Since LSCI and SCOS are primarily used on blood flow studies with CMOS cameras, the camera exposure is typically much longer than the sample's τ_c. However, the opposite situation, where the camera exposure is fast compared to the tissue dynamics, has not been studied in depth. To dissect the problem, in Figure 6.6, I have drawn the mean temporal

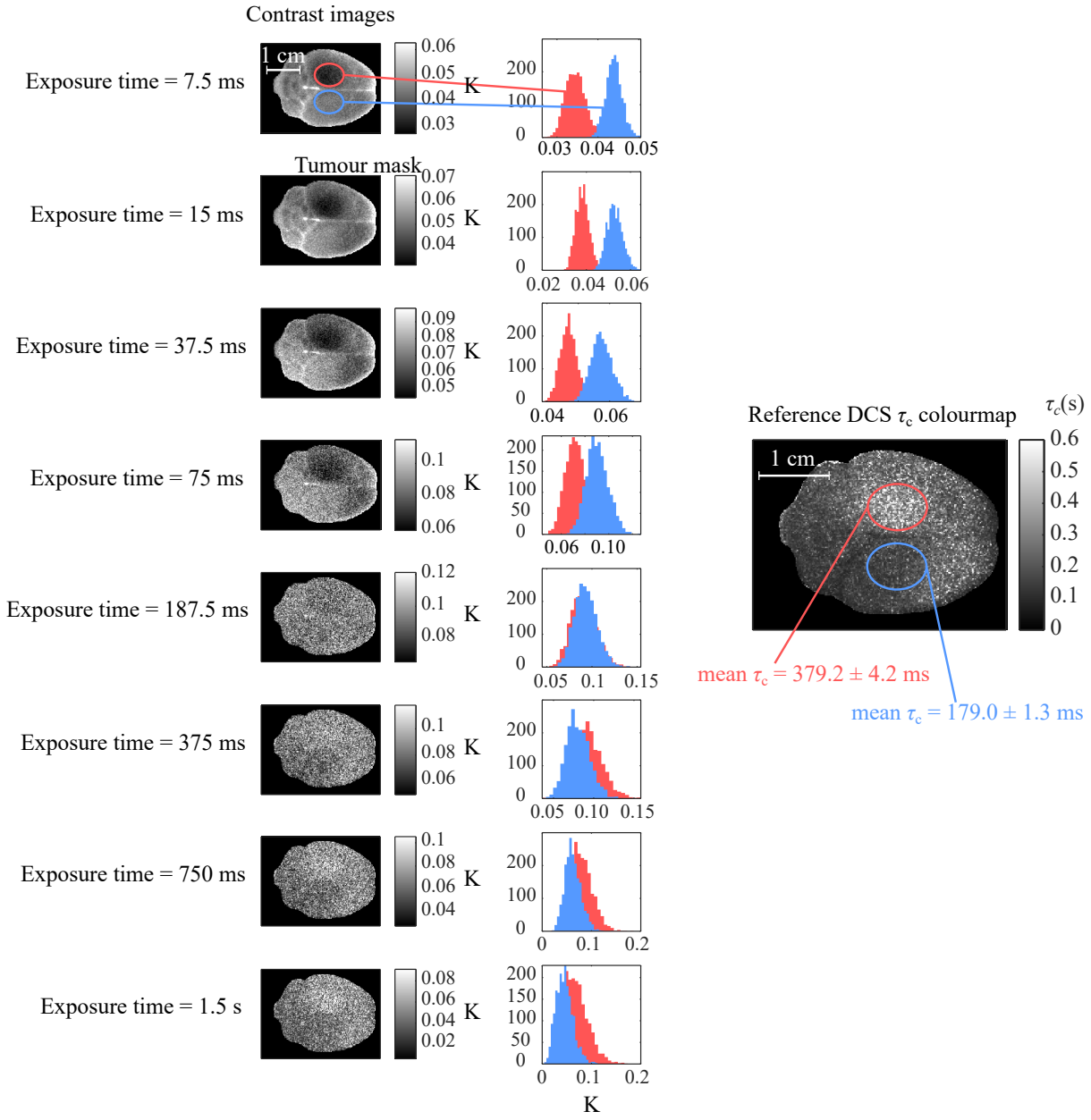

Figure 6.6: **Speckle contrast versus camera exposure time.** A contrast image for various camera exposure times is shown for 10 s speckle series data of the mouse brain and tumour proxy. Contrast histograms for tumour (red) and healthy (blue) ROIs are also shown. Lastly, on the right is a corresponding DCS image for 10 s speckle series data is also shown with annotations of the mean τ_c for healthy and tumoured brain regions. A flipping of the contrast signal is seen at camera exposure times around that of the healthy ROI's τ_c.

contrast images for various camera exposure times along with corresponding histograms from tumour and healthy brain regions. The above was produced using a 10 s acquisition of the mouse brain and tumour proxy data. The exposure times here were changed in post-processing by binning consecutive frames. A corresponding DCS image, made from

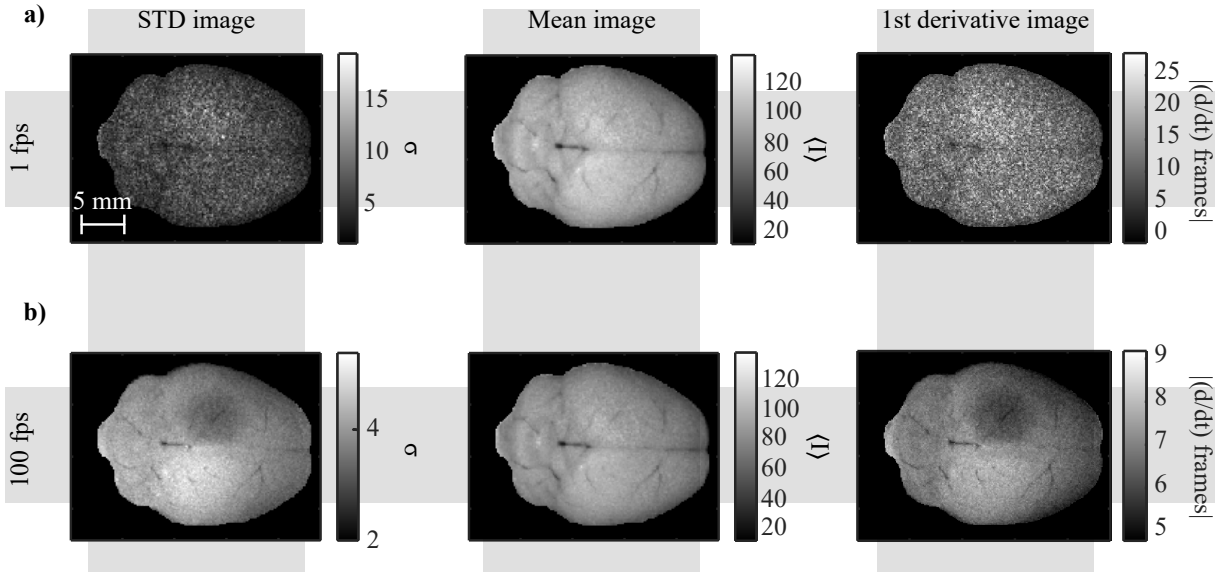

Figure 6.7: **Standard deviation, mean, and first-order derivative image of speckle series.** a) From left to right, colour maps of the standard deviation, mean, and first-order derivative of the speckle series are shown for 1 fps data. Each colour map is a mean value over a 10 s acquisition. The same window size as previous laser speckle contrast analysis is used here. b) shows the above colour maps again but for 100 fps, 10 s data. Comparing the 1 and 100 fps data, the standard deviation and first-order derivative images exhibit a flip in their signals at the tumour proxy site, whereas the mean intensity images do not.

the same 10 s acquisition data, is also shown for reference. It can be seen in these results that the temporal contrast signal in the tumour region flips when $T_{\text{exp}} \sim \tau_c$.

One possible explanation for the lower temporal contrast seen at the tumour site for the 100 fps data is that the pixel time series have a smaller rate of change than the healthy tissue due to less motion in the stiffer areas of the sample. Here, a smaller rate of change in the time series should also translate to a smaller standard deviation and smaller contrast. In Figure 6.7, I have drawn, for both 1 fps data in (a) and 100 fps data in (b), colour maps of standard deviation, mean, and first-order derivative of the speckle series across the time axis. We see in the 1 fps data in (a) that the standard deviation of the brain's speckle pattern is increased at the tumour site. No signal is seen in the mean intensity image of the brain, but like the standard deviation image, there is also a slight increase in the rate of change of the speckle. However, for the 100 fps data, we observe a lower standard deviation and a lower rate of change at the injection site. Again, no tumour signal is seen in the mean intensity image. The lower contrast signal in the high frame rate temporal contrast image is, therefore, likely caused by a smaller standard deviation at the tumour site.

As supporting evidence, I also plot the FFT of the time series for the tumour and healthy regions in Figure 6.8. The ROIs here are as previously defined in Figure 6.6. The amplitude

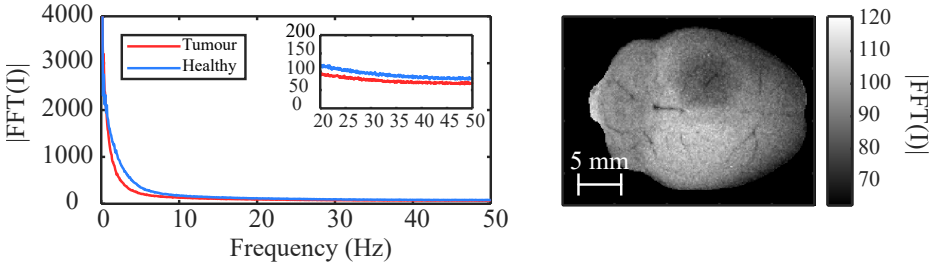

Figure 6.8: **Mouse brain tumour proxy and healthy tissue spectra.** On the left are two spectra for healthy brain tissue (blue) and the tumour proxy tissue (red). The tumour spectrum has slightly higher amplitudes at higher frequencies than the healthy tissue spectra. Data has been constructed from a 10 s acquisition of the brain. On the right is a summed spectral image of the brain, created by summing the frequency amplitudes from 20-50 Hz. A dark spot at the tumour site indicates lower high-frequency amplitudes.

of the FFT here should also give insight into how quickly the time series is changing, with larger high-frequency components indicative of faster changes in the speckle pattern's time series. The healthy tissue time series have more higher frequency content than the tumour tissue. This is also shown in a mean FFT image, which is made by taking the average amplitude for each pixel in the 20-50 Hz frequency range. This image is very similar to the first-order derivative image from Figure 6.7 since both methods effectively represent high-pass filtering of the speckle pattern series.

The above three figures suggest that for the speckle patterns captured, the low contrast signal for high camera frame rates and short camera exposures is due to the speckle pattern's slow-changing dynamics. The above results do not necessarily disagree with past LSCI and SCOS studies, as they point towards a different regime of contrast measurements, where the camera exposure is smaller than the sample's speckle decorrelation time. However, it is uncertain whether this rule, which suggests that the contrast should be small for stiff samples when the camera exposure is short, is general. The rule indeed holds for the data used in this thesis, which I should note is representative of many other speckle series data I have not included here. However, more work is required in the future, for example, to determine whether this rule holds for other types of time series data, such as from in vivo or live samples.

6.7 Conclusions

This chapter outlined different methods for improving the acquisition time of DCS measurements. Namely, we introduced an ML-DCS model that required only a fraction of the acquisition time needed for a standard DCS measurement. For our measurements on a brain tumour proxy, we reduced the acquisition time from 120 s to 1 s when using the

ML approach. Our method could be a medically relevant and real-time imaging device at these measurement timescales. Furthermore, laser speckle contrast imaging, a method that utilised the same data format as DCS, was also tested and could segment the tumour proxy well for 1 s acquisition times with further improvements in SNR to the DCS and ML-DCS imaging formats.

The work done in this and the previous chapter is particularly promising. We have shown that our device can conceptually image tumours and aid surgeons intraoperatively. Now, work towards translating this research to more clinical settings may be carried out. As it stands, our device is untested on either living systems or real tumours. These are two areas that the technique must prove itself in before becoming a clinical tool. I would like to go into more detail on future experiments in my concluding chapter.

CHAPTER 7

Conclusions and Future Outlooks

7.1 Conclusions of Work Carried Out

Optical technologies are powerful tools because they are often cheap, portable, and simple in design. They have helped the fields of biology and medicine in many ways since the advent of the microscope. In this thesis, I took one optical technology, DCS, that I felt could be expanded and made more medically relevant. DCS is a well-known technique often used for blood flow measurements. It is already used in human applications, particularly for sensing brain activation. However, its lesser-known application takes advantage of its sensitivity to tissue mechanics. This thesis shows two novel applications of DCS and improves its speed that is targeted at slow tissue mechanics.

Chapter 4 saw the first application of DCS in its traditional sensing format and was used to assess neurodegeneration in ex vivo healthy and neurodegenerated brain slices. Our results showed a statistically significant difference between the speckle decorrelation of healthy and diseased brain samples. It measured that neurodegenerated brains were statistically softer than healthy brains. However, current classifiers trained on DCS data applied to brains struggle to differentiate between healthy and diseased brains.

Chapter 5 introduced a new DCS imaging format that measured the surface speckle emanating from a brain sample with a high-stiffness tumour proxy. As a proof-of-concept, the chapter showed that DCS could be used to image and segment tumours from healthy brain tissue.

Chapter 6 detailed computational improvements to the DCS technique. One major drawback of the technique is its long acquisition times required to resolve the speckle decorrelation. An ML-DCS model that substituted the DCS g_2 calculation and performed well with a fraction of the acquisition time required improved on the standard DCS approach. A similar speckle-based imaging scheme to DCS, called LSCI, was also studied and was very effective for segmenting tumours at short acquisition times, more so than DCS.

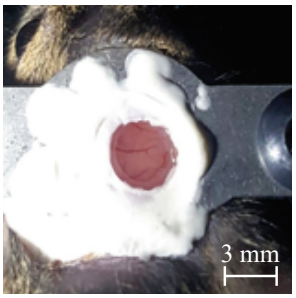

Figure 7.1: **An example optical window into a mouse's brain.** Image taken from [219].

7.2 Outline of Future Work

The work I have discussed is open-ended and can be progressed in many different ways. I want to close this thesis and discuss my future vision of my work.

In terms of the neurodegeneration work outlined in chapter 4, we took a large sample size of different mouse brains to search for differences in speckle decorrelation with respect to neurodegeneration and we observed a large variation amongst the mouse brains. To avoid statistical variation amongst different brain samples, a more useful experiment may be to perform longitudinal measurements, where the signal from a single brain could be compared over the course of the disease. A benefit of this is that this experiment would require fewer mice than our previous experiment. However, this type of experiment is more challenging as it involves in vivo measurements, where the presence of blood flow may affect the DCS measurements. It is unclear if a slow signal related to tissue mechanics can still be found in the presence of blood flow. On one hand, others have performed DCS measurements on blood flow and at time scales that are too short to resolve the speckle decorrelation of tissue mechanics. On the other hand, DCS measurements have otherwise been performed on ex vivo systems to measure slow tissue mechanics devoid of blood flow. However, slow tissue mechanics DCS measurements in the presence of blood flow have not been reported before, and it would be worthwhile to explore this further.

One problem with DCS on live systems is its penetration depth. Typically, DCS is limited to millimetre depths. In this case, surgical techniques can make an optically transparent window into the brain that is stable for a number of weeks [217–220]. Therefore, future experiments could first track neurodegeneration longitudinally on mice with the optical skull window, and if this is successful, move towards fully in vivo, noninvasive, and longitudinal studies. Our current neurodegeneration model is ideal here as it progresses quickly. An example optical skull window in a mouse is shown in Figure 7.1.

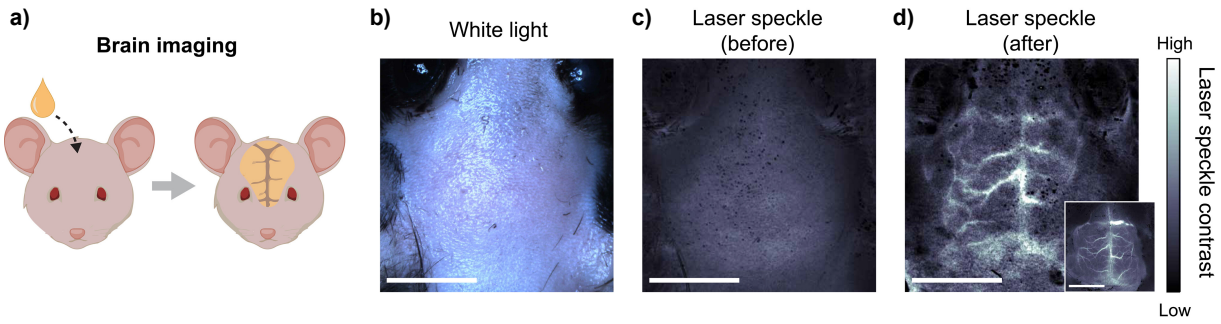

Figure 7.2: **Non-harmful optical clearing for live imaging.** a) an illustration of the dye in action, where an aqueous solution containing the dye is rubbed gently on a mouse's head, making the head more transmitting of the red wavelengths of light over time. b) A white light image of the mouse's head, which has been shaved. c) An LSCI image of the mouse's head before applying the dye solution. d) An LSCI image of the mouse's head after applying the dye solution, where brain vasculature can clearly be made out. As further validation, the scalp was removed, and LSCI was repeated. This is shown in the inset of (d), which closely matches the former LSCI image with the dye solution. Figure taken from [221].

Alternatively, novel work in tissue clearing has recently been published [221], which can temporarily make skin and muscles transparent to near-infrared wavelengths of light. This uses a non-toxic food dye and is applied either by injection or as a topical solution. Tartarzine dye, when in an aqueous solution, is highly absorbing in the UV and blue regions of the spectrum and minimally absorbing in the red ($\geq$600 nm). When applied to a medium, the dye solution may increase the medium's refractive index and reduce scattering for red wavelengths. It has been tested on live mice and could be a more viable and less invasive option than the above skull optical window technique.

Results of the novel optical clearing technique applied on a mouse model with LSCI are outlined in Figure 7.2(a-d). A topical aqueous solution containing the dye is rubbed gently on the mouse's head, increasing its red light transmittance. This is illustrated in (a). For reference, before applying the dye solution, a white light image and LSCI image (with a 785 nm laser) of the mouse's shaved scalp were taken and shown in (b-c). No signal can be obtained beyond the scalp with white light (a) and with LSCI (b). However, after applying the dye solution on the scalp, LSCI can pick up the mouse brain's vasculature (c). This result closely matched a further LSCI image of the mouse brain after removing its scalp and skull, as shown in the inset of (c) [221].

For the work on tumour imaging, our results show that we can segment a tumour model down to acquisition times of 1 s with various DCS and speckle contrast techniques. This suggests that DCS or LSCI can be made into a clinical tool for tumour imaging, Of course, we have only tested on mouse brain tumour proxies. However, work could now be dedicated

to imaging real tumours and in vivo systems. Locally in Glasgow, it is possible to obtain a glioblastoma tumour mouse model with an optical window [217, 220]. Therefore, the next step in our experiment would be to test our device on this model or apply the non-harmful optical window approach detailed in [221].

Again, work will be needed to determine whether a viable DCS or LSCI signal can be obtained in the presence of blood flow. Firstly, we can assess whether our imaging techniques may still capture a signal from slow tissue mechanics when highly dynamic blood flow is also present. Liu et al.'s paper using SCOS [105] offers promising insights here, where they found that speckle decorrelation is more sensitive to slow tissue mechanics than blood flow if the source-detector separation is small. In our DCS and LSCI imaging techniques, we flood illuminate the sample and focus an objective onto its surface, effectively achieving a source-detector separation of 0 mm. Liu et al.'s result, therefore, suggests that we should still have sensitivity to slow tissue dynamics with our imaging methods.

In the meantime however, our past results in Section 3.6 provide a useful sanity check. Here, we saw that the g_2 curve of a slow τ_c signal could still be made out when in the presence of a fast τ_c signal. Furthermore, this was observed in simulated and real data. This outcome is promising for future experiments of our imaging systems on living brain, as using a slow frame rate camera may act as a filter of the fast blood flow component.

7.3 Final Remarks

In conclusion, this thesis has explored novel applications of DCS, a versatile technique that utilises the correlation of multiple scattered light. Through this work, we demonstrated that DCS, along with LSCI, holds the potential to assess two major health conditions. The research on remote neurodegeneration assessment is currently under review, and the novel imaging approach is patent pending, with a journal submission forthcoming. With continued advancements, DCS could soon become a common tool in research laboratories and, potentially, clinical settings. I hope to see a future where affordable, accessible optical techniques like this are more common. Expensive healthcare and research tools should be supplemented with cheaper alternatives that are available to all.

Bibliography

[1] P. Zakharov, F. Cardinaux, and F. Scheffold, "Multispeckle diffusing-wave spectroscopy with a single-mode detection scheme," *Physical Review E*, vol. 73, no. 1, 2006, ISSN: 1539-3755. DOI: 10.1103/physreve.73.011413.

[2] M. Prince, G. Ali, M. Guerchet, W. Yu-Tzu, and M. Prina, "The global prevalence of dementia," *World Alzheimer Report*, vol. 25, p. 45, 2009.

[3] M. Prince, A. Wimo, M. Guerchet, G.-C. Ali, Y.-T. Wu, and M. Prina, "World alzheimer report 2015. the global impact of dementia: an analysis of prevalence, incidence, cost and trends," Thesis, 2015.

[4] O. World Health, *WHO report on cancer: setting priorities, investing wisely and providing care for all*. Geneva: World Health Organization, 2020, ISBN: 9789240001299 9789240001305 (print version). [Online]. Available: https://iris.who.int/handle/10665/330745.

[5] H. Sung *et al.*, "Global cancer statistics 2020: globocan estimates of incidence and mortality worldwide for 36 cancers in 185 countries," *CA: A Cancer Journal for Clinicians*, vol. 71, no. 3, pp. 209–249, 2021, ISSN: 0007-9235. DOI: 10.3322/caac.21660.

[6] P. Piña-Sánchez *et al.*, "Cancer biology, epidemiology, and treatment in the 21st century: current status and future challenges from a biomedical perspective," *Cancer Control*, vol. 28, p. 107 327 482 110 387, 2021, ISSN: 1073-2748. DOI: 10.1177/10732748211038735.

[7] A. J. Mangram, T. C. Horan, M. L. Pearson, L. C. Silver, and W. R. Jarvis, "Guideline for prevention of surgical site infection, 1999," *American Journal of Infection Control*, vol. 27, no. 2, pp. 97–134, 1999, ISSN: 0196-6553. DOI: https://doi.org/10.1016/S0196-6553(99)70088-X. [Online]. Available: https://www.sciencedirect.com/science/article/pii/S019665539970088X.

[8] S. M. Beecher, D. P. O'Leary, R. Mclaughlin, and M. J. Kerin, "The impact of surgical complications on cancer recurrence rates: a literature review," *Oncology Research and Treatment*, vol. 41, no. 7-8, pp. 478–482, 2018, ISSN: 2296-5270. DOI: 10.1159/000487510.

[9] S. J. Bradley *et al.*, "M1 muscarinic allosteric modulators slow prion neurodegeneration and restore memory loss," *J Clin Invest*, vol. 127, no. 2, pp. 487–499, 2017, ISSN: 1558-8238 (Electronic) 0021-9738 (Print) 0021-9738 (Linking). DOI: 10.1172/JCI87526. [Online]. Available: https://www.ncbi.nlm.nih.gov/pubmed/27991860.

[10] M. Scarpa *et al.*, "Biased m1 muscarinic receptor mutant mice show accelerated progression of prion neurodegenerative disease," *Proceedings of the National Academy of Sciences*, vol. 118, no. 50, e2107389118, 2021, ISSN: 0027-8424. DOI: 10.1073/pnas.2107389118.

[11] A. I. Bush *et al.*, "The amyloid precursor protein of alzheimer's disease is released by human platelets," *Journal of Biological Chemistry*, vol. 265, no. 26, pp. 15 977–15 983, 1990, ISSN: 0021-9258. DOI: https://doi.org/10.1016/S0021-9258(18)55493-4. [Online]. Available: https://www.sciencedirect.com/science/article/pii/S0021925818554934.

[12] R. Shigemoto, S. Nomura, H. Ohishi, H. Sugihara, S. Nakanishi, and N. Mizuno, "Immunohistochemical localization of a metabotropic glutamate receptor, mglur5, in the rat brain," *Neuroscience Letters*, vol. 163, no. 1, pp. 53–57, 1993, ISSN: 0304-3940. DOI: https://doi.org/10.1016/0304-3940(93)90227-C. [Online]. Available: https://www.sciencedirect.com/science/article/pii/030439409390227C.

[13] C. Scheckel and A. Aguzzi, "Prions, prionoids and protein misfolding disorders," *Nature Reviews Genetics*, vol. 19, no. 7, pp. 405–418, 2018, ISSN: 1471-0056. DOI: 10.1038/s41576-018-0011-4. [Online]. Available: https://www.zora.uzh.ch/id/eprint/151651/8/ScheckelAguzzi_151651.pdf.

[14] E. Aronica, M. V. Catania, J. Geurts, B. Yankaya, and D. Troost, "Immunohistochemical localization of group i and ii metabotropic glutamate receptors in control and amyotrophic lateral sclerosis human spinal cord: upregulation in reactive astrocytes," *Neuroscience*, vol. 105, no. 2, pp. 509–520, 2001, ISSN: 0306-4522. DOI: https://doi.org/10.1016/S0306-4522(01)00181-6. [Online]. Available: https://www.sciencedirect.com/science/article/pii/S0306452201001816.

[15] M. C. Murphy *et al.*, "Magnetic resonance elastography of the brain in a mouse model of alzheimer's disease: initial results," *Magnetic Resonance Imaging*, vol. 30, no. 4, pp. 535–539, 2012, ISSN: 0730-725X. DOI: 10.1016/j.mri.2011.12.019. [Online]. Available: https://www.ncbi.nlm.nih.gov/pmc/articles/PMC3433281.

[16] G. R. Mallucci, "Prion neurodegeneration," *Prion*, vol. 3, no. 4, pp. 195–201, 2009, ISSN: 1933-6896. DOI: 10.4161/pri.3.4.9981.

[17] S. J. Webster, A. D. Bachstetter, P. T. Nelson, F. A. Schmitt, and L. J. Van Eldik, "Using mice to model alzheimer's dementia: an overview of the clinical disease and the preclinical behavioral changes in 10 mouse models," *Frontiers in Genetics*, vol. 5, 2014, ISSN: 1664-8021. DOI: 10.3389/fgene.2014.00088. [Online]. Available: https://www.frontiersin.org/articles/10.3389/fgene.2014.00088/pdf.

[18] T. Nakai, K. Yamada, and H. Mizoguchi, "Alzheimer's disease animal models: elucidation of biomarkers and therapeutic approaches for cognitive impairment," *International Journal of Molecular Sciences*, vol. 22, no. 11, p. 5549, 2021, ISSN: 1422-0067. DOI: 10.3390/ijms22115549.

[19] J. Pantel *et al.*, "In vivo quantification of brain volumes in subcortical vascular dementia and alzheimer's disease," *Dementia and Geriatric Cognitive Disorders*, vol. 9, no. 6, pp. 309–316, 1998, ISSN: 1420-8008. DOI: 10.1159/000017082.

[20] J. C. Baron *et al.*, "In vivo mapping of gray matter loss with voxel-based morphometry in mild alzheimer's disease," *NeuroImage*, vol. 14, no. 2, pp. 298–309, 2001, ISSN: 1053-8119. DOI: https://doi.org/10.1006/nimg.2001.0848. [Online]. Available: https://www.sciencedirect.com/science/article/pii/S1053811901908481.

[21] S. J. Teipel, T. Meindl, L. Grinberg, H. Heinsen, and H. Hampel, "Novel mri techniques in the assessment of dementia," *European Journal of Nuclear Medicine and Molecular Imaging*, vol. 35, no. S1, pp. 58–69, 2008, ISSN: 1619-7070. DOI: 10.1007/s00259-007-0703-z.

[22] G. Mallucci, A. Dickinson, J. Linehan, P.-C. Klöhn, S. Brandner, and J. Collinge, "Depleting neuronal prp in prion infection prevents disease and reverses spongiosis," *Science*, vol. 302, no. 5646, pp. 871–874, 2003. DOI: 10.1126/science.1090187. [Online]. Available: https://doi.org/10.1126/science.1090187.

[23] Y. Feng, M. C. Murphy, E. Hojo, F. Li, and N. Roberts, "Magnetic resonance elastography in the study of neurodegenerative diseases," *Journal of Magnetic Resonance Imaging*, vol. 59, no. 1, pp. 82–96, 2024, ISSN: 1053-1807. DOI: 10.1002/jmri.28747.

[24] E. G. Hain *et al.*, "Dopaminergic neurodegeneration in the mouse is associated with decrease of viscoelasticity of substantia nigra tissue," *PLOS ONE*, vol. 11, no. 8, e0161179, 2016, ISSN: 1932-6203. DOI: 10.1371/journal.pone.0161179. [Online]. Available: http://europepmc.org/articles/pmc4985068?pdf=render.

[25] T. Munder *et al.*, "Mr elastography detection of early viscoelastic response of the murine hippocampus to amyloid β accumulation and neuronal cell loss due to alzheimer's disease," *Journal of Magnetic Resonance Imaging*, vol. 47, no. 1, pp. 105–114, 2018, ISSN: 1053-1807. DOI: 10.1002/jmri.25741. [Online]. Available: https://onlinelibrary.wiley.com/doi/pdf/10.1002/jmri.25741.

[26] S. Majumdar and D. Klatt, "Longitudinal study of sub-regional cerebral viscoelastic properties of 5xfad alzheimer's disease mice using multifrequency mr elastography," *Magnetic Resonance in Medicine*, vol. 86, no. 1, pp. 405–414, 2021, ISSN: 0740-3194. DOI: 10.1002/mrm.28709.

[27] K. Pavuluri *et al.*, "Differential effect of dementia etiology on cortical stiffness as assessed by mr elastography," *NeuroImage: Clinical*, vol. 37, p. 103 328, 2023, ISSN: 2213-1582. DOI: https://doi.org/10.1016/j.nicl.2023.103328. [Online]. Available: https://www.sciencedirect.com/science/article/pii/S2213158223000177.

[28] M. C. Murphy *et al.*, "Decreased brain stiffness in alzheimer's disease determined by magnetic resonance elastography," *Journal of Magnetic Resonance Imaging*, vol. 34, no. 3, pp. 494–498, 2011, ISSN: 1053-1807. DOI: 10.1002/jmri.22707. [Online]. Available: http://europepmc.org/articles/pmc3217096?pdf=render.

[29] A. Romano *et al.*, "In vivo waveguide elastography: effects of neurodegeneration in patients with amyotrophic lateral sclerosis," *Magnetic Resonance in Medicine*, vol. 72, no. 6, pp. 1755–1761, 2014, ISSN: 0740-3194. DOI: 10.1002/mrm.25067.

[30] J. Huston *et al.*, "Magnetic resonance elastography of frontotemporal dementia," *Journal of Magnetic Resonance Imaging*, vol. 43, no. 2, pp. 474–478, 2016, ISSN: 1053-1807. DOI: 10.1002/jmri.24977. [Online]. Available: https://www.ncbi.nlm.nih.gov/pmc/articles/PMC4696917.

[31] M. C. Murphy *et al.*, "Regional brain stiffness changes across the alzheimer's disease spectrum," *NeuroImage: Clinical*, vol. 10, pp. 283–290, 2016, ISSN: 2213-1582. DOI: https://doi.org/10.1016/j.nicl.2015.12.007. [Online]. Available: https://www.sciencedirect.com/science/article/pii/S2213158215300462.

[32] M. Elsheikh *et al.*, "Mr elastography demonstrates unique regional brain stiffness patterns in dementias," *American Journal of Roentgenology*, vol. 209, no. 2, pp. 403–408, 2017, ISSN: 0361-803X. DOI: 10.2214/ajr.16.17455.

[33] L. M. Gerischer *et al.*, "Combining viscoelasticity, diffusivity and volume of the hippocampus for the diagnosis of alzheimer's disease based on magnetic resonance imaging," *Neuroimage Clin*, vol. 18, pp. 485–493, 2018, ISSN: 2213-1582 (Electronic) 2213-1582 (Linking). DOI: 10.1016/j.nicl.2017.12.023. [Online]. Available: https://www.ncbi.nlm.nih.gov/pubmed/29527504.

[34] A. Lipp, C. Skowronek, A. Fehlner, K.-J. Streitberger, J. Braun, and I. Sack, "Progressive supranuclear palsy and idiopathic parkinson's disease are associated with local reduction of in vivo brain viscoelasticity," *European Radiology*, vol. 28, no. 8, pp. 3347–3354, 2018, ISSN: 0938-7994. DOI: 10.1007/s00330-017-5269-y.

[35] L. V. Hiscox *et al.*, "Mechanical property alterations across the cerebral cortex due to alzheimer's disease," *Brain Communications*, vol. 2, no. 1, fcz049, 2020, ISSN: 2632-1297. DOI: 10.1093/braincomms/fcz049. [Online]. Available: https://doi.org/10.1093/braincomms/fcz049.

[36] L. V. Hiscox, H. Schwarb, M. D. J. McGarry, and C. L. Johnson, "Aging brain mechanics: progress and promise of magnetic resonance elastography," *Neuroimage*, vol. 232, p. 117 889, 2021, ISSN: 1095-9572 (Electronic) 1053-8119 (Print) 1053-8119 (Linking). DOI: 10.1016/j.neuroimage.2021.117889. [Online]. Available: https://www.ncbi.nlm.nih.gov/pubmed/33617995.

[37] C. M. Hall, E. Moeendarbary, and G. K. Sheridan, "Mechanobiology of the brain in ageing and alzheimer's disease," *Eur J Neurosci*, vol. 53, no. 12, pp. 3851–3878, 2021, ISSN: 1460-9568 (Electronic) 0953-816X (Linking). DOI: 10.1111/ejn.14766. [Online]. Available: https://www.ncbi.nlm.nih.gov/pubmed/32356339.

[38] Y. Blinkouskaya, A. Cacoilo, T. Gollamudi, S. Jalalian, and J. Weickenmeier, "Brain aging mechanisms with mechanical manifestations," *Mech Ageing Dev*, vol. 200, p. 111 575, 2021, ISSN: 1872-6216 (Electronic) 0047-6374 (Print) 0047-6374 (Linking). DOI: 10.1016/j.mad.2021.111575. [Online]. Available: https://www.ncbi.nlm.nih.gov/pubmed/34600936.

[39] K. Hoyt *et al.*, "Tissue elasticity properties as biomarkers for prostate cancer," *Cancer Biomarkers*, vol. 4, no. 4-5, pp. 213–225, 2008, ISSN: 1875-8592. DOI: 10.3233/cbm-2008-44-505.

[40] B. H. Duhon *et al.*, "Tumor biomechanical stiffness by magnetic resonance elastography predicts surgical outcomes and identifies biomarkers in vestibular schwannoma and meningioma," *Scientific Reports*, vol. 14, no. 1, 2024, ISSN: 2045-2322. DOI: 10.1038/s41598-024-64597-1.

[41] G. Ciasca *et al.*, "Nano-mechanical signature of brain tumours," *Nanoscale*, vol. 8, no. 47, pp. 19 629–19 643, 2016, ISSN: 2040-3364. DOI: 10.1039/c6nr06840e.

[42] D. C. Stewart, A. Rubiano, K. Dyson, and C. S. Simmons, "Mechanical characterization of human brain tumors from patients and comparison to potential surgical phantoms," *PLOS ONE*, vol. 12, no. 6, e0177561, 2017, ISSN: 1932-6203. DOI: 10.1371/journal.pone.0177561. [Online]. Available: https://journals.plos.org/plosone/article/file?id=10.1371/journal.pone.0177561&type=printable.

[43] H. Mohammadi and E. Sahai, "Mechanisms and impact of altered tumour mechanics," *Nature Cell Biology*, vol. 20, no. 7, pp. 766–774, 2018, ISSN: 1465-7392. DOI: 10.1038/s41556-018-0131-2.

[44] A. Bunevicius, K. Schregel, R. Sinkus, A. Golby, and S. Patz, "Review: mr elastography of brain tumors," *NeuroImage: Clinical*, vol. 25, p. 102 109, 2020, ISSN: 2213-1582. DOI: https://doi.org/10.1016/j.nicl.2019.102109. [Online]. Available: https://www.sciencedirect.com/science/article/pii/S2213158219304565.

[45] K.-J. Streitberger *et al.*, "How tissue fluidity influences brain tumor progression," *Proceedings of the National Academy of Sciences*, vol. 117, no. 1, pp. 128–134, 2020, ISSN: 0027-8424. DOI: 10.1073/pnas.1913511116.

[46] K. Schregel *et al.*, "Magnetic resonance elastography reveals effects of anti-angiogenic glioblastoma treatment on tumor stiffness and captures progression in an orthotopic mouse model," *Cancer Imaging*, vol. 20, no. 1, 2020, ISSN: 1470-7330. DOI: 10.1186/s40644-020-00314-1.

[47] C. Alibert *et al.*, "Multiscale rheology of glioma cells," *Biomaterials*, vol. 275, p. 120 903, 2021, ISSN: 0142-9612. DOI: https://doi.org/10.1016/j.biomaterials.2021.120903. [Online]. Available: https://www.sciencedirect.com/science/article/pii/S0142961221002593.

[48] A. Massey *et al.*, "Mechanical properties of human tumour tissues and their implications for cancer development," *Nature Reviews Physics*, vol. 6, no. 4, pp. 269–282, 2024, ISSN: 2522-5820. DOI: 10.1038/s42254-024-00707-2.

[49] A. Nagelkerke, J. Bussink, A. E. Rowan, and P. N. Span, "The mechanical microenvironment in cancer: how physics affects tumours," *Seminars in Cancer Biology*, vol. 35, pp. 62–70, 2015, ISSN: 1044-579X. DOI: https://doi.org/10.1016/j.semcancer.2015.09.001. [Online]. Available: https://www.sciencedirect.com/science/article/pii/S1044579X15000747.

[50] D. C. Singleton, A. Macann, and W. R. Wilson, "Therapeutic targeting of the hypoxic tumour microenvironment," *Nature Reviews Clinical Oncology*, vol. 18, no. 12, pp. 751–772, 2021, ISSN: 1759-4782. DOI: 10.1038/s41571-021-00539-4. [Online]. Available: https://doi.org/10.1038/s41571-021-00539-4.

[51] S. Prasad *et al.*, "Optical and magnetic resonance imaging approaches for investigating the tumour microenvironment: state-of-the-art review and future trends," *Nanotechnology*, vol. 32, no. 6, p. 062 001, 2021, ISSN: 0957-4484. DOI: 10.1088/1361-6528/abc208.

[52] I. Martínez-Reyes and N. S. Chandel, "Cancer metabolism: looking forward," *Nature Reviews Cancer*, vol. 21, no. 10, pp. 669–680, 2021, ISSN: 1474-175X. DOI: 10.1038/s41568-021-00378-6.

[53] Z. He *et al.*, "A review on methods for diagnosis of breast cancer cells and tissues," *Cell Proliferation*, vol. 53, no. 7, 2020, ISSN: 0960-7722. DOI: 10.1111/cpr.12822.

[54] J. Yang, R. Xu, C. Wang, J. Qiu, B. Ren, and L. You, "Early screening and diagnosis strategies of pancreatic cancer: a comprehensive review," *Cancer Communications*, vol. 41, no. 12, pp. 1257–1274, 2021, ISSN: 2523-3548. DOI: 10.1002/cac2.12204.

[55] A. W. Brenner and A. J. Patel, "Review of current principles of the diagnosis and management of brain metastases," *Frontiers in Oncology*, vol. 12, 2022, ISSN: 2234-943X. DOI: 10.3389/fonc.2022.857622.

[56] M. Arabahmadi, R. Farahbakhsh, and J. Rezazadeh, "Deep learning for smart healthcare—a survey on brain tumor detection from medical imaging," *Sensors*, vol. 22, no. 5, p. 1960, 2022, ISSN: 1424-8220. DOI: 10.3390/s22051960.

[57] M. Jermyn *et al.*, "Intraoperative brain cancer detection with raman spectroscopy in humans," *Science Translational Medicine*, vol. 7, no. 274, 274ra19–274ra19, 2015. DOI: 10.1126/scitranslmed.aaa2384. [Online]. Available: https://doi.org/10.1126/scitranslmed.aaa2384.

[58] J. Desroches *et al.*, "A new method using raman spectroscopy for in vivo targeted brain cancer tissue biopsy," *Scientific Reports*, vol. 8, no. 1, 2018, ISSN: 2045-2322. DOI: 10.1038/s41598-018-20233-3. [Online]. Available: https://www.ncbi.nlm.nih.gov/pmc/articles/PMC5788981.

[59] J. Desroches *et al.*, "Development and first in-human use of a raman spectroscopy guidance system integrated with a brain biopsy needle," *Journal of Biophotonics*, vol. 12, no. 3, e201800396, 2019, ISSN: 1864-063X. DOI: https://doi.org/10.1002/jbio.201800396. [Online]. Available: https://doi.org/10.1002/jbio.201800396.

[60] L. J. Lauwerends *et al.*, "Real-time fluorescence imaging in intraoperative decision making for cancer surgery," *The Lancet Oncology*, vol. 22, no. 5, e186–e195, 2021, ISSN: 1470-2045. DOI: 10.1016/s1470-2045(20)30600-8.

[61] A. Alfonso-Garcia *et al.*, "Real-time augmented reality for delineation of surgical margins during neurosurgery using autofluorescence lifetime contrast," *Journal of Biophotonics*, vol. 13, no. 1, e201900108, 2020, ISSN: 1864-063X. DOI: https://doi.org/10.1002/jbio.201900108. [Online]. Available: https://doi.org/10.1002/jbio.201900108.

[62] A. Alfonso-Garcia *et al.*, "In vivo characterization of the human glioblastoma infiltrative edge with label-free intraoperative fluorescence lifetime imaging," *Biomedical Optics Express*, vol. 14, no. 5, pp. 2196–2208, 2023. DOI: 10.1364/BOE.481304. [Online]. Available: https://opg.optica.org/boe/abstract.cfm?URI=boe-14-5-2196.

[63] P. A. Janmey, P. C. Georges, and S. Hvidt, "Basic rheology for biologists," in *Methods in Cell Biology*. Academic Press, 2007, vol. 83, pp. 1–27, ISBN: 0091-679X. DOI: https://doi.org/10.1016/S0091-679X(07)83001-9. [Online]. Available: https://www.sciencedirect.com/science/article/pii/S0091679X07830019.

[64] D. A. Weitz, J. X. Zhu, D. J. Durian, G. Hu, and D. J. Pine, "Diffusing-wave spectroscopy: the technique and some applications," *Physica Scripta*, vol. 1993, no. T49B, p. 610, 1993, ISSN: 1402-4896 0031-8949. DOI: 10.1088/0031-8949/1993/T49B/040. [Online]. Available: https://dx.doi.org/10.1088/0031-8949/1993/T49B/040.

[65] G. Maret, "Diffusing-wave spectroscopy," *Current Opinion in Colloid & Interface Science*, vol. 2, no. 3, pp. 251–257, 1997, ISSN: 1359-0294. DOI: 10.1016/s1359-0294(97)80032-5.

[66] D. J. Pine, D. A. Weitz, P. M. Chaikin, and E. Herbolzheimer, "Diffusing wave spectroscopy," *Physical Review Letters*, vol. 60, no. 12, pp. 1134–1137, 1988, ISSN: 0031-9007. DOI: 10.1103/physrevlett.60.1134.

[67] C. Cheung, J. P. Culver, K. Takahashi, J. H. Greenberg, and A. G. Yodh, "In vivo cerebrovascular measurement combining diffuse near-infrared absorption and correlation spectroscopies," *Physics in Medicine and Biology*, vol. 46, no. 8, pp. 2053–2065, 2001, ISSN: 0031-9155. DOI: 10.1088/0031-9155/46/8/302.

[68] A. C. Stefan, B. R. Mitchell, and A. F. Maria, "Diffuse correlation spectroscopy: current status and future outlook," *Neurophotonics*, vol. 10, no. 1, p. 013 509, 2023. DOI: 10.1117/1.NPh.10.1.013509. [Online]. Available: https://doi.org/10.1117/1.NPh.10.1.013509.

[69] T. Durduran and A. G. Yodh, "Diffuse correlation spectroscopy for non-invasive, micro-vascular cerebral blood flow measurement," *NeuroImage*, vol. 85, pp. 51–63, 2014, ISSN: 1053-8119. DOI: 10.1016/j.neuroimage.2013.06.017. [Online]. Available: http://europepmc.org/articles/pmc3991554?pdf=render.

[70] B. Berne and R. Pecora, *Dynamic Light Scattering: With Applications to Chemistry, Biology, and Physics*. Dover Publications, 2000, ISBN: 9780486411552. [Online]. Available: https://books.google.co.uk/books?id=pNOikJBH8qMC.

[71] G. Maret and P. E. Wolf, "Multiple light scattering from disordered media. the effect of brownian motion of scatterers," *Zeitschrift fr Physik B Condensed Matter*, vol. 65, no. 4, pp. 409–413, 1987, ISSN: 0722-3277. DOI: 10.1007/bf01303762.

[72] R. C. Mesquita *et al.*, "Hemodynamic and metabolic diffuse optical monitoring in a mouse model of hindlimb ischemia," *Biomedical Optics Express*, vol. 1, no. 4, p. 1173, 2010, ISSN: 2156-7085. DOI: 10.1364/boe.1.001173.

[73] R. C. Mesquita *et al.*, "Direct measurement of tissue blood flow and metabolism with diffuse optics," *Philosophical Transactions of the Royal Society A: Mathematical, Physical and Engineering Sciences*, vol. 369, no. 1955, pp. 4390–4406, 2011, ISSN: 1364-503X. DOI: 10.1098/rsta.2011.0232. [Online]. Available: http://europepmc.org/articles/pmc3263785?pdf=render.

[74] A. B. David, S. Sava, J. S. Juliette, F. Parisa, F. Maria Angela, and A. C. Stefan, "Establishing the diffuse correlation spectroscopy signal relationship with blood flow," *Neurophotonics*, vol. 3, no. 3, p. 031 412, 2016. DOI: 10.1117/1.NPh.3.3.031412. [Online]. Available: https://doi.org/10.1117/1.NPh.3.3.031412.

[75] J. Sutin *et al.*, "Time-domain diffuse correlation spectroscopy," *Optica*, vol. 3, no. 9, pp. 1006–1013, 2016. DOI: 10.1364/OPTICA.3.001006. [Online]. Available: https://opg.optica.org/optica/abstract.cfm?URI=optica-3-9-1006.

[76] A. C. Stefan *et al.*, "Diffuse correlation spectroscopy measurements of blood flow using 1064 nm light," *Journal of Biomedical Optics*, vol. 25, no. 9, p. 097 003, 2020. DOI: 10.1117/1.JBO.25.9.097003. [Online]. Available: https://doi.org/10.1117/1.JBO.25.9.097003.

[77] C. G. Favilla *et al.*, "Dynamic cerebral autoregulation measured by diffuse correlation spectroscopy," *Journal of Cerebral Blood Flow & Metabolism*, vol. 43, no. 8, pp. 1317–1327, 2023, ISSN: 0271-678X. DOI: 10.1177/0271678x231153728.

[78] W. Liu *et al.*, "Fast and sensitive diffuse correlation spectroscopy with highly parallelized single photon detection," *APL Photonics*, vol. 6, no. 2, p. 026 106, 2021, ISSN: 2378-0967. DOI: 10.1063/5.0031225.

[79] S. Xu *et al.*, "Imaging dynamics beneath turbid media via parallelized single-photon detection," *Advanced Science*, vol. 9, no. 24, p. 2 201 885, 2022, ISSN: 2198-3844. DOI: 10.1002/advs.202201885.

[80] E. J. Sie *et al.*, "High-sensitivity multispeckle diffuse correlation spectroscopy," *Neurophotonics*, vol. 7, no. 3, pp. 035 010–035 010, 2020, ISSN: 2329-423X.

[81] M. A. Wayne *et al.*, "Massively parallel, real-time multispeckle diffuse correlation spectroscopy using a 500×500 SPAD camera," EN, *Biomedical Optics Express*, vol. 14, no. 2, pp. 703–713, Feb. 2023, ISSN: 2156-7085. DOI: 10.1364/BOE.473992. [Online]. Available: https://opg.optica.org/boe/abstract.cfm?uri=boe-14-2-703 (visited on 01/17/2023).

[82] D. A. Boas, "Diffuse photon probes of structural and dynamical properties of turbid media: theory and biomedical applications," Ph.D. dissertation, University of Pennsylvania, 1996.

[83] W. I. Goldburg, "Dynamic light scattering," *American Journal of Physics*, vol. 67, no. 12, pp. 1152–1160, 1999, ISSN: 0002-9505. DOI: 10.1119/1.19101. [Online]. Available: https://doi.org/10.1119/1.19101.

[84] P. Zakharov, F. Cardinaux, and F. Scheffold, "Multispeckle diffusing-wave spectroscopy with a single-mode detection scheme," *Physical Review E*, vol. 73, no. 1, 2006, ISSN: 1539-3755. DOI: 10.1103/physreve.73.011413.

[85] C. U. Devi, R. S. B. Chandran, M. V. Ram, and K. S. Ajay, "Measurement of visco-elastic properties of breast-tissue mimicking materials using diffusing wave spectroscopy," *Journal of Biomedical Optics*, vol. 12, no. 3, p. 034 035, 2007. DOI: 10.1117/1.2743081. [Online]. Available: https://doi.org/10.1117/1.2743081.

[86] Z. Hajjarian and S. K. Nadkarni, "Evaluating the viscoelastic properties of tissue from laser speckle fluctuations," *Scientific Reports*, vol. 2, no. 1, 2012, ISSN: 2045-2322. DOI: 10.1038/srep00316. [Online]. Available: https://doi.org/10.1038/srep00316.

[87] Z. Hajjarian and S. K. Nadkarni, "Evaluation and correction for optical scattering variations in laser speckle rheology of biological fluids," *PLoS ONE*, vol. 8, no. 5, e65014, 2013, ISSN: 1932-6203. DOI: 10.1371/journal.pone.0065014. [Online]. Available: http://europepmc.org/articles/pmc3660338?pdf=render.

[88] Z. H. Nadkarni and S. K., "Correction of optical absorption and scattering variations in laser speckle rheology measurements," *Optics Express*, vol. 22, no. 6, pp. 66 349–6361, 2014. DOI: 10.1364/OE.22.006349.

[89] Z. Hajjarian and S. K. Nadkarni, "Estimation of particle size variations for laser speckle rheology of materials," *Optics Letters*, vol. 40, no. 5, p. 764, 2015, ISSN: 0146-9592. DOI: 10.1364/ol.40.000764.

[90] Z. Hajjarian, H. T. Nia, S. Ahn, A. J. Grodzinsky, R. K. Jain, and S. K. Nadkarni, "Laser speckle rheology for evaluating the viscoelastic properties of hydrogel scaffolds," *Scientific Reports*, vol. 6, no. 1, p. 37 949, 2016, ISSN: 2045-2322. DOI: 10.1038/srep37949. [Online]. Available: https://dspace.mit.edu/bitstream/1721.1/109340/1/Laser%20speckle.pdf.

[91] Z. Hajjarian, E. F. Brachtel, D. M. Tshikudi, and S. K. Nadkarni, "Mapping mechanical properties of the tumor microenvironment by laser speckle rheological microscopy," *Cancer Research*, vol. 81, no. 18, pp. 4874–4885, 2021, ISSN: 0008-5472. DOI: 10.1158/0008-5472.can-20-3898.

[92] N. Leartprapun, Z. Zeng, Z. Hajjarian, V. Bossuyt, and S. K. Nadkarni, "Laser speckle rheological microscopy reveals wideband viscoelastic spectra of biological tissues," *Science Advances*, vol. 10, no. 19, eadl1586, 2024. DOI: doi:10.1126/sciadv.adl1586. [Online]. Available: https://www.science.org/doi/abs/10.1126/sciadv.adl1586.

[93] T. G. Mason, H. Gang, and D. A. Weitz, "Diffusing-wave-spectroscopy measurements of viscoelasticity of complex fluids," *Journal of the Optical Society of America A*, vol. 14, no. 1, pp. 139–149, 1997. DOI: 10.1364/JOSAA.14.000139. [Online]. Available: https://opg.optica.org/josaa/abstract.cfm?URI=josaa-14-1-139.

[94] B. R. Dasgupta, S.-Y. Tee, J. C. Crocker, B. J. Frisken, and D. A. Weitz, "Microrheology of polyethylene oxide using diffusing wave spectroscopy and single scattering," *Physical Review E*, vol. 65, no. 5, 2002, ISSN: 1063-651X. DOI: 10.1103/physreve.65.051505.

[95] A. F. Fercher and J. D. Briers, "Flow visualization by means of single-exposure speckle photography," *Optics Communications*, vol. 37, no. 5, pp. 326–330, 1981, ISSN: 0030-4018. DOI: https://doi.org/10.1016/0030-4018(81)90428-4. [Online]. Available: https://www.sciencedirect.com/science/article/pii/0030401881904284.

[96] A. B. David and K. D. Andrew, "Laser speckle contrast imaging in biomedical optics," *Journal of Biomedical Optics*, vol. 15, no. 1, p. 011 109, 2010. DOI: 10.1117/1.3285504. [Online]. Available: https://doi.org/10.1117/1.3285504.

[97] J. Senarathna, A. Rege, N. Li, and N. V. Thakor, "Laser speckle contrast imaging: theory, instrumentation and applications," *IEEE Reviews in Biomedical Engineering*, vol. 6, pp. 99–110, 2013, ISSN: 1937-3333. DOI: 10.1109/rbme.2013.2243140.

[98] S. S. Kazmi, L. M. Richards, C. J. Schrandt, M. A. Davis, and A. K. Dunn, "Expanding applications, accuracy, and interpretation of laser speckle contrast imaging of cerebral blood flow," *Journal of Cerebral Blood Flow & Metabolism*, vol. 35, no. 7, pp. 1076–1084, 2015, ISSN: 0271-678X. DOI: 10.1038/jcbfm.2015.84. [Online]. Available: http://europepmc.org/articles/pmc4640282?pdf=render.

[99] H. Wido, S. Wiendelt, M. v. D. Gooitzen, and E. C. Boerma, "Clinical applications of laser speckle contrast imaging: a review," *Journal of Biomedical Optics*, vol. 24, no. 8, p. 080 901, 2019. DOI: 10.1117/1.JBO.24.8.080901. [Online]. Available: https://doi.org/10.1117/1.JBO.24.8.080901.

[100] S. Zheng and J. Mertz, "Direct characterization of tissue dynamics with laser speckle contrast imaging," *Biomedical Optics Express*, vol. 13, no. 8, pp. 4118–4133, 2022, ISSN: 2156-7085. DOI: 10.1364/BOE.462913. [Online]. Available: https://opg.optica.org/boe/abstract.cfm?uri=boe-13-8-4118%20https://opg.optica.org/viewmedia.cfm?uri=boe-13-8-4118&seq=0.

[101] A. Konovalov *et al.*, "Laser speckle contrast imaging in neurosurgery: a systematic review," *World Neurosurgery*, vol. 171, pp. 35–40, 2023, ISSN: 1878-8750. DOI: https://doi.org/10.1016/j.wneu.2022.12.048. [Online]. Available: https://www.sciencedirect.com/science/article/pii/S1878875022017521.

[102] C. P. Valdes, H. M. Varma, A. K. Kristoffersen, T. Dragojevic, J. P. Culver, and T. Durduran, "Speckle contrast optical spectroscopy, a non-invasive, diffuse optical method for measuring microvascular blood flow in tissue," *Biomedical Optics Express*, vol. 5, no. 8, p. 2769, 2014, ISSN: 2156-7085. DOI: 10.1364/boe.5.002769.

[103] B. Kim *et al.*, "Measuring human cerebral blood flow and brain function with fiber-based speckle contrast optical spectroscopy system," *Communications Biology*, vol. 6, no. 1, 2023, ISSN: 2399-3642. DOI: 10.1038/s42003-023-05211-4.

[104] C.-H. P. Lin *et al.*, "Multi-mode fiber-based speckle contrast optical spectroscopy: analysis of speckle statistics," *Optics Letters*, vol. 48, no. 6, pp. 1427–1430, 2023. DOI: 10.1364/OL.478956. [Online]. Available: https://opg.optica.org/ol/abstract.cfm?URI=ol-48-6-1427.

[105] B. Liu, S. Shah, G. Küreli, A. Devor, D. A. Boas, and X. Cheng, "Measurements of slow tissue dynamics with short-separation speckle contrast optical spectroscopy," *Biomedical Optics Express*, vol. 14, no. 9, pp. 4790–4799, 2023, ISSN: 2156-7085. DOI: 10.1364/BOE.497604. [Online]. Available: https://opg.optica.org/boe/abstract.cfm?uri=boe-14-9-4790%20https://opg.optica.org/viewmedia.cfm?uri=boe-14-9-4790&seq=0.

[106] X. Chen, Y. Wang, J. Lu, and P. Li, "Simultaneous viscosity and elasticity measurement using laser speckle contrast imaging," *Optics Letters*, vol. 43, no. 7, pp. 1582–1585, 2018. DOI: 10.1364/OL.43.001582. [Online]. Available: https://opg.optica.org/ol/abstract.cfm?URI=ol-43-7-1582.

[107] X. Chen, J. Lu, and P. Li, "Elastography with low-frame-rate laser speckle contrast imaging using the aliasing effect," *Optics Letters*, vol. 43, no. 12, pp. 2811–2814, 2018. DOI: 10.1364/OL.43.002811. [Online]. Available: https://opg.optica.org/ol/abstract.cfm?URI=ol-43-12-2811.

[108] M. Damzen, V. Vlad, A. Mocofanescu, and V. Babin, *Stimulated Brillouin Scattering: Fundamentals and Applications*, 1st. CRC Press, 2003. DOI: https://doi.org/10.1201/9781420033465.

[109] R. R. Jones, D. C. Hooper, L. Zhang, D. Wolverson, and V. K. Valev, "Raman techniques: fundamentals and frontiers," *Nanoscale Research Letters*, vol. 14, no. 1, 2019, ISSN: 1931-7573. DOI: 10.1186/s11671-019-3039-2. [Online]. Available: https://doaj.org/article/881b702ce83f4144853c9f00fb81639e.

[110] R. Prevedel, A. Diz-Muñoz, G. Ruocco, and G. Antonacci, "Brillouin microscopy: an emerging tool for mechanobiology," *Nature Methods*, vol. 16, no. 10, pp. 969–977, 2019, ISSN: 1548-7091. DOI: 10.1038/s41592-019-0543-3.

[111] I. Kabakova *et al.*, "Brillouin microscopy," *Nature Reviews Methods Primers*, vol. 4, no. 1, p. 8, 2024, ISSN: 2662-8449. DOI: 10.1038/s43586-023-00286-z. [Online]. Available: https://doi.org/10.1038/s43586-023-00286-z.

[112] J. Zhang, M. Nikolic, K. Tanner, and G. Scarcelli, "Rapid biomechanical imaging at low irradiation level via dual line-scanning brillouin microscopy," *Nature Methods*, vol. 20, no. 5, pp. 677–681, 2023, ISSN: 1548-7091. DOI: 10.1038/s41592-023-01816-z.

[113] K. V. Berghaus, S. H. Yun, and G. Scarcelli, "High speed sub-ghz spectrometer for brillouin scattering analysis," *J Vis Exp*, no. 106, e53468, 2015, ISSN: 1940-087x. DOI: 10.3791/53468.

[114] G. Antonacci *et al.*, "Recent progress and current opinions in brillouin microscopy for life science applications," *Biophysical Reviews*, vol. 12, no. 3, pp. 615–624, 2020, ISSN: 1867-2450. DOI: 10.1007/s12551-020-00701-9.

[115] C. W. Ballmann, J. V. Thompson, A. J. Traverso, Z. Meng, M. O. Scully, and V. V. Yakovlev, "Stimulated brillouin scattering microscopic imaging," *Scientific Reports*, vol. 5, no. 1, p. 18 139, 2015, ISSN: 2045-2322. DOI: 10.1038/srep18139. [Online]. Available: https://www.ncbi.nlm.nih.gov/pmc/articles/PMC4686920.

[116] F. Yang *et al.*, "Pulsed stimulated brillouin microscopy enables high-sensitivity mechanical imaging of live and fragile biological specimens," *Nature Methods*, vol. 20, no. 12, pp. 1971–1979, 2023, ISSN: 1548-7091. DOI: 10.1038/s41592-023-02054-z.

[117] K. J. Koski and J. L. Yarger, "Brillouin imaging," *Applied Physics Letters*, vol. 87, no. 6, p. 061 903, 2005, ISSN: 0003-6951. DOI: 10.1063/1.1999857.

[118] J. G. Dil, "Brillouin scattering in condensed matter," *Reports on Progress in Physics*, vol. 45, no. 3, pp. 285–334, 1982, ISSN: 0034-4885. DOI: 10.1088/0034-4885/45/3/002.

[119] M. A. Cardinali *et al.*, "Brillouin micro-spectroscopy of subchondral, trabecular bone and articular cartilage of the human femoral head," *Biomedical Optics Express*, vol. 10, no. 5, p. 2606, 2019, ISSN: 2156-7085. DOI: 10.1364/boe.10.002606.

[120] M. Alunni Cardinali *et al.*, "Brillouin–raman microspectroscopy for the morpho-mechanical imaging of human lamellar bone," *Journal of The Royal Society Interface*, vol. 19, no. 187, 2022, ISSN: 1742-5662. DOI: 10.1098/rsif.2021.0642.

[121] P.-J. Wu *et al.*, "Detection of proteoglycan loss from articular cartilage using brillouin microscopy, with applications to osteoarthritis," *Biomedical Optics Express*, vol. 10, no. 5, p. 2457, 2019, ISSN: 2156-7085. DOI: 10.1364/boe.10.002457.

[122] C. Riquelme-Guzmán *et al.*, "in vivoassessment of mechanical properties during axolotl development and regeneration using confocal brillouin microscopy," *Open Biology*, vol. 12, no. 6, 2022, ISSN: 2046-2441. DOI: 10.1098/rsob.220078.

[123] G. Antonacci *et al.*, "Birefringence-induced phase delay enables brillouin mechanical imaging in turbid media," *Nature Communications*, vol. 15, no. 1, 2024, ISSN: 2041-1723. DOI: 10.1038/s41467-024-49419-2.

[124] G. Antonacci *et al.*, "Quantification of plaque stiffness by brillouin microscopy in experimental thin cap fibroatheroma," *Journal of The Royal Society Interface*, vol. 12, no. 112, p. 20 150 843, 2015, ISSN: 1742-5689. DOI: 10.1098/rsif.2015.0843. [Online]. Available: https://digitalcommons.unl.edu/cgi/viewcontent.cgi?article=1297&context=mechengfacpub.

[125] J. Margueritat *et al.*, "High-frequency mechanical properties of tumors measured by brillouin light scattering," *Physical Review Letters*, vol. 122, no. 1, 2019, ISSN: 0031-9007. DOI: 10.1103/physrevlett.122.018101.

[126] V. Mahajan *et al.*, "Mapping tumor spheroid mechanics in dependence of 3d microenvironment stiffness and degradability by brillouin microscopy," *Cancers*, vol. 13, no. 21, p. 5549, 2021, ISSN: 2072-6694. DOI: 10.3390/cancers13215549.

[127] C. Conrad, K. Moore, W. Polacheck, I. Rizvi, and G. Scarcelli, "Mechanical modulation of ovarian cancer tumor nodules under flow," *IEEE Transactions on Biomedical Engineering*, vol. 69, no. 1, pp. 294–301, 2022, ISSN: 0018-9294. DOI: 10.1109/tbme.2021.3092641.

[128] S. Mattana, S. Caponi, F. Tamagnini, D. Fioretto, and F. Palombo, "Viscoelasticity of amyloid plaques in transgenic mouse brain studied by brillouin microspectroscopy and correlative raman analysis," *Journal of Innovative Optical Health Sciences*, vol. 10, no. 06, p. 1 742 001, 2017, ISSN: 1793-5458. DOI: 10.1142/s1793545817420019.

[129] F. Palombo *et al.*, "Hyperspectral analysis applied to micro-brillouin maps of amyloid-beta plaques in alzheimer's disease brains," *The Analyst*, vol. 143, no. 24, pp. 6095–6102, 2018, ISSN: 0003-2654. DOI: 10.1039/c8an01291a. [Online]. Available: https://pubs.rsc.org/en/content/articlepdf/2018/an/c8an01291a.

[130] J. M. Schmitt, "Oct elastography: imaging microscopic deformation and strain of tissue," *Optics Express*, vol. 3, no. 6, pp. 199–211, 1998. DOI: 10.1364/OE.3.000199. [Online]. Available: https://opg.optica.org/oe/abstract.cfm?URI=oe-3-6-199.

[131] R. C. Chan *et al.*, "Oct-based arterial elastography: robust estimation exploiting tissue biomechanics," *Optics Express*, vol. 12, no. 19, pp. 4558–4572, 2004. DOI: 10.1364/OPEX.12.004558. [Online]. Available: https://opg.optica.org/oe/abstract.cfm?URI=oe-12-19-4558.

[132] B. F. Kennedy, K. M. Kennedy, and D. D. Sampson, "A review of optical coherence elastography: fundamentals, techniques and prospects," *IEEE Journal of Selected Topics in Quantum Electronics*, vol. 20, no. 2, pp. 272–288, 2014, ISSN: 1077-260X. DOI: 10.1109/jstqe.2013.2291445.

[133] B. F. Kennedy, K. M. Kennedy, A. L. Oldenburg, S. G. Adie, S. A. Boppart, and D. D. Sampson, *Optical coherence elastography*. Springer, to be published, 2015, pp. 1007–1054.

[134] B. F. Kennedy, P. Wijesinghe, and D. D. Sampson, "The emergence of optical elastography in biomedicine," *Nature Photonics*, vol. 11, no. 4, pp. 215–221, 2017, ISSN: 1749-4885. DOI: 10.1038/nphoton.2017.6.

[135] D. P. Popescu *et al.*, "Optical coherence tomography: fundamental principles, instrumental designs and biomedical applications," *Biophysical Reviews*, vol. 3, no. 3, pp. 155–169, 2011, ISSN: 1867-2450. DOI: 10.1007/s12551-011-0054-7. [Online]. Available: https://nrc-publications.canada.ca/eng/view/accepted/?id=70f8baef-21c8-459f-b465-d0e07e28e713.

[136] X. Liang, V. Crecea, and S. A. Boppart, "Dynamic optical coherence elastography: a review," *Journal of Innovative Optical Health Sciences*, vol. 03, no. 04, pp. 221–233, 2010, ISSN: 1793-5458. DOI: 10.1142/s1793545810001180.

[137] M. Villiger *et al.*, "Deep tissue volume imaging of birefringence through fibre-optic needle probes for the delineation of breast tumour," *Scientific Reports*, vol. 6, no. 1, p. 28 771, 2016, ISSN: 2045-2322. DOI: 10.1038/srep28771. [Online]. Available: https://www.ncbi.nlm.nih.gov/pmc/articles/PMC4929466.

[138] G. R. Ge, W. Song, M. J. Giannetto, J. P. Rolland, M. Nedergaard, and K. J. Parker, "Mouse brain elastography changes with sleep/wake cycles, aging, and alzheimer's disease," *NeuroImage*, vol. 295, p. 120 662, 2024, ISSN: 1053-8119. DOI: https://doi.org/10.1016/j.neuroimage.2024.120662. [Online]. Available: https://www.sciencedirect.com/science/article/pii/S1053811924001575.

[139] R. G. Gary *et al.*, "A preliminary study on using reverberant shear wave fields in optical coherence elastography to examine mice brain ex vivo," in *Proc.SPIE*, vol. 10880, 2019, p. 108801D. DOI: 10.1117/12.2516039. [Online]. Available: https://doi.org/10.1117/12.2516039.

[140] K. M. Kennedy, B. F. Kennedy, R. A. McLaughlin, and D. D. Sampson, "Needle optical coherence elastography for tissue boundary detection," *Optics Letters*, vol. 37, no. 12, pp. 2310–2312, 2012. DOI: 10.1364/OL.37.002310. [Online]. Available: https://opg.optica.org/ol/abstract.cfm?URI=ol-37-12-2310.

[141] M. K. Kelsey *et al.*, "Needle optical coherence elastography for the measurement of microscale mechanical contrast deep within human breast tissues," *Journal of Biomedical Optics*, vol. 18, no. 12, p. 121 510, 2013. DOI: 10.1117/1.JBO.18.12.121510. [Online]. Available: https://doi.org/10.1117/1.JBO.18.12.121510.

[142] A. Ashkin, J. M. Dziedzic, J. E. Bjorkholm, and S. Chu, "Observation of a single-beam gradient force optical trap for dielectric particles," *Optics Letters*, vol. 11, no. 5, pp. 288–290, 1986. DOI: 10.1364/OL.11.000288. [Online]. Available: https://opg.optica.org/ol/abstract.cfm?URI=ol-11-5-288.

[143] H. Wang *et al.*, "Recent advances of optical tweezers–based dynamic force spectroscopy and mechanical measurement assays for live-cell mechanobiology," *Frontiers in Physics*, vol. 10, 2022, ISSN: 2296-424X. DOI: 10.3389/fphy.2022.771111.

[144] D. Preece *et al.*, "Optical tweezers: wideband microrheology," *Journal of Optics*, vol. 13, no. 4, p. 044 022, 2011, ISSN: 2040-8986 2040-8978. DOI: 10.1088/2040-8978/13/4/044022. [Online]. Available: https://dx.doi.org/10.1088/2040-8978/13/4/044022.

[145] M. Tassieri, R. M. L. Evans, R. L. Warren, N. J. Bailey, and J. M. Cooper, "Microrheology with optical tweezers: data analysis," *New Journal of Physics*, vol. 14, no. 11, p. 115 032, 2012, ISSN: 1367-2630. DOI: 10.1088/1367-2630/14/11/115032. [Online]. Available: https://dx.doi.org/10.1088/1367-2630/14/11/115032.

[146] M. Tassieri, "Microrheology with optical tweezers: peaks & troughs," *Current Opinion in Colloid & Interface Science*, vol. 43, pp. 39–51, 2019, ISSN: 1359-0294. DOI: 10.1016/j.cocis.2019.02.006.

[147] A. B. Matheson *et al.*, "Microrheology with an anisotropic optical trap," *Frontiers in Physics*, vol. 9, 2021, ISSN: 2296-424X. DOI: 10.3389/fphy.2021.621512.

[148] M. G. Smith *et al.*, "Machine learning opens a doorway for microrheology with optical tweezers in living systems," *AIP Advances*, vol. 13, no. 7, 2023, ISSN: 2158-3226. DOI: 10.1063/5.0161014.

[149] J. Goodman, *Introduction to Fourier Optics*. W. H. Freeman, 2005, ISBN: 9780974707723. [Online]. Available: https://books.google.co.uk/books?id=ow5xs_Rtt9AC.

[150] J. Goodman, *Speckle Phenomena in Optics: Theory and Applications*. Roberts & Company, 2007, ISBN: 9780974707792. [Online]. Available: https://books.google.co.uk/books?id=TynXEcS0DncC.

[151] G. Fowles, *Introduction to Modern Optics*. Dover Publications, 1989, ISBN: 9780486659572. [Online]. Available: https://books.google.co.uk/books?id=SL1n9TuJ5YMC.

[152] M. Lax, "Multiple scattering of waves," *Reviews of Modern Physics*, vol. 23, no. 4, pp. 287–310, 1951. DOI: 10.1103/RevModPhys.23.287. [Online]. Available: https://link.aps.org/doi/10.1103/RevModPhys.23.287.

[153] M. Lax, "Multiple scattering of waves. ii. the effective field in dense systems," *Physical Review*, vol. 85, no. 4, pp. 621–629, 1952. DOI: 10.1103/PhysRev.85.621. [Online]. Available: https://link.aps.org/doi/10.1103/PhysRev.85.621.

[154] N. Fayard, A. Cazé, R. Pierrat, and R. Carminati, "Intensity correlations between reflected and transmitted speckle patterns," *Physical Review A*, vol. 92, no. 3, 2015, ISSN: 1050-2947 1094-1622. DOI: 10.1103/PhysRevA.92.033827.

[155] I. Starshynov, "Quantum and classical correlations of multiply scattered light," Thesis, 2018.

[156] G. Volpe and G. Volpe, "Simulation of a brownian particle in an optical trap," *American Journal of Physics*, vol. 81, no. 3, pp. 224–230, 2013, ISSN: 0002-9505. DOI: 10.1119/1.4772632. [Online]. Available: https://doi.org/10.1119/1.4772632.

[157] T. Vettenburg, S. A. R. Horsley, and J. Bertolotti, "Calculating coherent light-wave propagation in large heterogeneous media," *Opt Express*, vol. 27, no. 9, pp. 11 946–11 967, 2019, ISSN: 1094-4087 (Electronic) 1094-4087 (Linking). DOI: 10.1364/OE.27.011946. [Online]. Available: https://www.ncbi.nlm.nih.gov/pubmed/31052742.

[158] L. Valantinas and T. Vettenburg, "Scaling up wave calculations with a scattering network," *Intelligent Computing*, vol. 3, p. 0098, 2024. DOI: 10.34133/icomputing.0098. [Online]. Available: https://doi.org/10.34133/icomputing.0098.

[159] A. Lyons *et al.*, "Attosecond-resolution hong-ou-mandel interferometry," *Science Advances*, vol. 4, no. 5, eaap9416, 2018. DOI: 10.1126/sciadv.aap9416. [Online]. Available: https://doi.org/10.1126/sciadv.aap9416.

[160] B. Ndagano *et al.*, "Quantum microscopy based on hong–ou–mandel interference," *Nature Photonics*, vol. 16, no. 5, pp. 384–389, 2022, ISSN: 1749-4885. DOI: 10.1038/s41566-022-00980-6.

[161] A. Lyons *et al.*, "Fluorescence lifetime hong-ou-mandel sensing," *Nature Communications*, vol. 14, no. 1, 2023, ISSN: 2041-1723. DOI: 10.1038/s41467-023-43868-x.

[162] E. W. Weisstein, *Wiener-khinchin theorem.* https://mathworld.wolfram.com/Wiener-KhinchinTheorem.html.

[163] J. W. Goodman, *Statistical optics*. John Wiley & Sons, 2015, ISBN: 1119009456.

[164] N. Uribe-Patarroyo, A. L. Post, S. Ruiz-Lopera, D. J. Faber, and B. E. Bouma, "Noise and bias in optical coherence tomography intensity signal decorrelation," *OSA Continuum*, vol. 3, no. 4, pp. 709–741, 2020. DOI: 10.1364/OSAC.385431. [Online]. Available: https://opg.optica.org/osac/abstract.cfm?URI=osac-3-4-709.

[165] V. Viasnoff, F. Lequeux, and D. J. Pine, "Multispeckle diffusing-wave spectroscopy: a tool to study slow relaxation and time-dependent dynamics," *Review of Scientific Instruments*, vol. 73, no. 6, pp. 2336–2344, 2002, ISSN: 0034-6748. DOI: 10.1063/1.1476699. [Online]. Available: http://arxiv.org/pdf/cond-mat/0203396.

[166] F. Velardi, F. Fraternali, and M. Angelillo, "Anisotropic constitutive equations and experimental tensile behavior of brain tissue," *Biomechanics and Modeling in Mechanobiology*, vol. 5, no. 1, pp. 53–61, 2006, ISSN: 1617-7959. DOI: 10.1007/s10237-005-0007-9.

[167] Y. M. Efremov, W.-H. Wang, S. D. Hardy, R. L. Geahlen, and A. Raman, "Measuring nanoscale viscoelastic parameters of cells directly from afm force-displacement curves," *Scientific Reports*, vol. 7, no. 1, 2017, ISSN: 2045-2322. DOI: 10.1038/s41598-017-01784-3. [Online]. Available: https://www.ncbi.nlm.nih.gov/pmc/articles/PMC5431511.

[168] G. Singh and A. Chanda, "Mechanical properties of whole-body soft human tissues: a review," *Biomedical Materials*, vol. 16, no. 6, p. 062 004, 2021, ISSN: 1748-605X.

[169] G. Ciccone, M. Azevedo Gonzalez Oliva, N. Antonovaite, I. Lüchtefeld, M. Salmeron-Sanchez, and M. Vassalli, "Experimental and data analysis workflow for soft matter nanoindentation," *Journal of Visualized Experiments*, no. 179, 2022, ISSN: 1940-087X. DOI: 10.3791/63401.

[170] H. Van Hoorn, N. A. Kurniawan, G. H. Koenderink, and D. Iannuzzi, "Local dynamic mechanical analysis for heterogeneous soft matter using ferrule-top indentation," *Soft Matter*, vol. 12, no. 12, pp. 3066–3073, 2016, ISSN: 1744-683X. DOI: 10.1039/c6sm00300a. [Online]. Available: https://pure.tue.nl/ws/files/16973293/HoornLocaldynamic2016.pdf.

[171] F. Baldini *et al.*, "Biomechanics of cultured hepatic cells during different steatogenic hits," *Journal of the Mechanical Behavior of Biomedical Materials*, vol. 97, pp. 296–305, 2019, ISSN: 1751-6161. DOI: https://doi.org/10.1016/j.jmbbm.2019.05.036. [Online]. Available: https://www.sciencedirect.com/science/article/pii/S1751616118317260.

[172] N. Antonovaite, S. V. Beekmans, E. M. Hol, W. J. Wadman, and D. Iannuzzi, "Regional variations in stiffness in live mouse brain tissue determined by depth-controlled indentation mapping," *Scientific Reports*, vol. 8, no. 1, 2018, ISSN: 2045-2322. DOI: 10.1038/s41598-018-31035-y. [Online]. Available: https://doi.org/10.1038/s41598-018-31035-y.

[173] G. Ciccone *et al.*, "What caging force cells feel in 3d hydrogels: a rheological perspective," *Advanced Healthcare Materials*, vol. 9, no. 17, p. 2 000 517, 2020, ISSN: 2192-2640. DOI: 10.1002/adhm.202000517.

[174] R. Emig *et al.*, "Piezo1 channels contribute to the regulation of human atrial fibroblast mechanical properties and matrix stiffness sensing," *Cells*, vol. 10, no. 3, p. 663, 2021, ISSN: 2073-4409. DOI: 10.3390/cells10030663.

[175] O. Dobre *et al.*, "A hydrogel platform that incorporates laminin isoforms for efficient presentation of growth factors – neural growth and osteogenesis," *Advanced Functional Materials*, vol. 31, no. 21, p. 2 010 225, 2021, ISSN: 1616-301X. DOI: 10.1002/adfm.202010225.

[176] G. Wu, M. Gotthardt, and M. Gollasch, "Assessment of nanoindentation in stiffness measurement of soft biomaterials: kidney, liver, spleen and uterus," *Scientific Reports*, vol. 10, no. 1, 2020, ISSN: 2045-2322. DOI: 10.1038/s41598-020-75738-7.

[177] M. Krieg *et al.*, "Atomic force microscopy-based mechanobiology," *Nature Reviews Physics*, vol. 1, no. 1, pp. 41–57, 2018, ISSN: 2522-5820. DOI: 10.1038/s42254-018-0001-7.

[178] Z. D. Jastrzebski and R. Komanduri, "The nature and properties of engineering materials," *J. Eng. Mater. Technol.*, 1988, ISSN: 0094-4289.

[179] L. Su *et al.*, "Distinguishing poroelasticity and viscoelasticity of brain tissue with time scale," *Acta Biomaterialia*, vol. 155, pp. 423–435, 2023, ISSN: 1742-7061. DOI: https://doi.org/10.1016/j.actbio.2022.11.009. [Online]. Available: https://www.sciencedirect.com/science/article/pii/S174270612200736X.

[180] K. P. Menard and N. R. Menard, "Dynamic mechanical analysis," 2020. DOI: 10.1201/9780429190308.

[181] V. Gradauskas, J. Radford, K. J. Mitchell, S. Nerenberg, I. Starshynov, and D. Faccio, "Photon transport through the adult human head," in *Optica Imaging Congress 2024 (3D, AOMS, COSI, ISA, pcAOP)*, ser. Technical Digest Series, Optica Publishing Group, CM1B.2. [Online]. Available: https://opg.optica.org/abstract.cfm?URI=COSI-2024-CM1B.2.

[182] K. J. Mitchell *et al.*, "Energy transport in diffusive waveguides," *arXiv preprint arXiv:2402.03064*, 2024.

[183] L. Dwomoh, G. S. Tejeda, and A. B. Tobin, "Targeting the m1 muscarinic acetylcholine receptor in alzheimer's disease," *Neuronal Signaling*, vol. 6, no. 1, 2022, ISSN: 2059-6553. DOI: 10.1042/ns20210004. [Online]. Available: https://doi.org/10.1042/NS20210004.

[184] M. F. Tuite and T. R. Serio, "The prion hypothesis: from biological anomaly to basic regulatory mechanism," *Nature Reviews Molecular Cell Biology*, vol. 11, no. 12, pp. 823–833, 2010, ISSN: 1471-0072. DOI: 10.1038/nrm3007. [Online]. Available: http://europepmc.org/articles/pmc3003427?pdf=render.

[185] C. Soto, "Prion hypothesis: the end of the controversy?" *Trends in Biochemical Sciences*, vol. 36, no. 3, pp. 151–158, 2011, ISSN: 0968-0004. DOI: 10.1016/j.tibs.2010.11.001. [Online]. Available: http://europepmc.org/articles/pmc3056934?pdf=render.

[186] G. Mallucci, "Spreading proteins in neurodegeneration: where do they take us?" *Brain*, vol. 136, no. 4, pp. 994–995, 2013, ISSN: 0006-8950. DOI: 10.1093/brain/awt072. [Online]. Available: https://doi.org/10.1093/brain/awt072.

[187] B. N. Dugger and D. W. Dickson, "Pathology of neurodegenerative diseases," *Cold Spring Harbor Perspectives in Biology*, vol. 9, no. 7, a028035, 2017, ISSN: 1943-0264. DOI: 10.1101/cshperspect.a028035. [Online]. Available: http://cshperspectives.cshlp.org/content/9/7/a028035.full.pdf.

[188] Z. Jaunmuktane and S. Brandner, "Invited review: the role of prion-like mechanisms in neurodegenerative diseases," *Neuropathology and Applied Neurobiology*, vol. 46, no. 6, pp. 522–545, 2020, ISSN: 0305-1846. DOI: 10.1111/nan.12592.

[189] J. R. Tse and A. J. Engler, "Preparation of hydrogel substrates with tunable mechanical properties," *Current Protocols in Cell Biology*, vol. 47, no. 1, pp. 10.16.1–10.16.16, 2010, ISSN: 1934-2500. DOI: https://doi.org/10.1002/0471143030.cb1016s47. [Online]. Available: https://doi.org/10.1002/0471143030.cb1016s47.

[190] B. L. Welch, "The generalization of 'student's'problem when several different population varlances are involved," *Biometrika*, vol. 34, no. 1-2, pp. 28–35, 1947, ISSN: 1464-3510.

[191] R. V. Hogg, J. W. McKean, and A. T. Craig, *Introduction to mathematical statistics*. Pearson Education India, 2013, ISBN: 817758930X.

[192] L. Stahle and S. Wold, "Analysis of variance (anova)," *Chemometrics and Intelligent Laboratory Systems*, vol. 6, no. 4, pp. 259–272, 1989, ISSN: 0169-7439. DOI: https://doi.org/10.1016/0169-7439(89)80095-4. [Online]. Available: https://www.sciencedirect.com/science/article/pii/0169743989800954.

[193] H. L. Harter and N. Balakrishnan, *Tables for the use of range and studentized range in tests of hypotheses*. CRC Press, 1997, ISBN: 0849331145.

[194] T. Haslwanter, *An Introduction to Statistics with Python*, 1st ed. Springer Cham, 2016, ISBN: 978-3-319-80323-4. DOI: https://doi.org/10.1007/978-3-319-28316-6.

[195] E. Aarts, M. Verhage, J. V. Veenvliet, C. V. Dolan, and S. Van Der Sluis, "A solution to dependency: using multilevel analysis to accommodate nested data," *Nature Neuroscience*, vol. 17, no. 4, pp. 491–496, 2014, ISSN: 1097-6256. DOI: 10.1038/nn.3648. [Online]. Available: https://www.nature.com/articles/nn.3648.pdf.

[196] H. Begum, P. Murugesan, and A. D. Tangutur, "Western blotting: a powerful staple in scientific and biomedical research," *BioTechniques*, vol. 73, no. 1, pp. 58–69, 2022, ISSN: 0736-6205. DOI: 10.2144/btn-2022-0003.

[197] S. C. Taylor and A. Posch, "The design of a quantitative western blot experiment," *BioMed Research International*, vol. 2014, pp. 1–8, 2014, ISSN: 2314-6133. DOI: 10.1155/2014/361590. [Online]. Available: https://doi.org/10.1155/2014/361590.

[198] H. S. Kwon and S.-H. Koh, "Neuroinflammation in neurodegenerative disorders: the roles of microglia and astrocytes," *Translational Neurodegeneration*, vol. 9, no. 1, 2020, ISSN: 2047-9158. DOI: 10.1186/s40035-020-00221-2.

[199] F. Pedregosa *et al.*, "Scikit-learn: machine learning in Python," *Journal of Machine Learning Research*, vol. 12, pp. 2825–2830, 2011.

[200] H. Zhang, "Exploring conditions for the optimality of naïve bayes," *International Journal of Pattern Recognition and Artificial Intelligence*, vol. 19, no. 02, pp. 183–198, 2005, ISSN: 0218-0014. DOI: 10.1142/S0218001405003983. [Online]. Available: https://doi.org/10.1142/S0218001405003983.

[201] B. E. Boser, I. M. Guyon, and V. N. Vapnik, "A training algorithm for optimal margin classifiers," in *Proceedings of the fifth annual workshop on Computational learning theory*, ACM, 1992. DOI: 10.1145/130385.130401.

[202] H. Yu and S. Kim, "Svm tutorial-classification, regression and ranking," *Handbook of Natural computing*, vol. 1, pp. 479–506, 2012.

[203] M. Leonetti, *Speckle autocorrelation*, https://www.mathworks.com/matlabcentral/fileexchange/94765-speckle-autocorrelation, 2021.

[204] M. J. Lindstrom and D. M. Bates, "Newton—raphson and em algorithms for linear mixed-effects models for repeated-measures data," *Journal of the American Statistical Association*, vol. 83, no. 404, pp. 1014–1022, 1988. DOI: https://doi.org/10.1080/01621459.1988.10478693. [Online]. Available: https://doi.org/10.1080/01621459.1988.10478693.

[205] M. Palotai *et al.*, "Magnetic resonance elastography to study the effect of amyloid plaque accumulation in a mouse model," *Journal of Neuroimaging*, vol. 32, no. 4, pp. 617–628, 2022, ISSN: 1051-2284. DOI: 10.1111/jon.12996.

[206] B. Li and R. M. Dr. Aspden, "Composition and mechanical properties of cancellous bone from the femoral head of patients with osteoporosis or osteoarthritis," *Journal of Bone and Mineral Research*, vol. 12, no. 4, pp. 641–651, 1997, ISSN: 0884-0431. DOI: 10.1359/jbmr.1997.12.4.641.

[207] S.-O. Kim, J. Kim, T. Okajima, and N.-J. Cho, "Mechanical properties of paraformaldehyde-treated individual cells investigated by atomic force microscopy and scanning ion conductance microscopy," *Nano Convergence*, vol. 4, no. 1, 2017, ISSN: 2196-5404. DOI: 10.1186/s40580-017-0099-9. [Online]. Available: http://europepmc.org/articles/pmc5359366?pdf=render.

[208] K. B. Velle, C. Fermino Do Rosário, P. Wadsworth, and L. K. Fritz-Laylin, "A onestep solution to fix and stain cells for correlative live and fixed microscopy," *Current Protocols*, vol. 1, no. 11, 2021, ISSN: 2691-1299. DOI: 10.1002/cpz1.308.

[209] M. I. H. Khan, N. Patel, M. Mahiuddin, and M. A. Karim, "Characterisation of mechanical properties of food materials during drying using nanoindentation," *Journal of Food Engineering*, vol. 291, p. 110 306, 2021, ISSN: 0260-8774. DOI: https://doi.org/10.1016/j.jfoodeng.2020.110306. [Online]. Available: https://www.sciencedirect.com/science/article/pii/S0260877420303940.

[210] J. Huston, "Magnetic resonance elastography of the brain," in *Magnetic Resonance Elastography*. Springer New York, 2014, pp. 89–98. DOI: 10.1007/978-1-4939-1575-0_8.

[211] A. S. Morr *et al.*, "Mechanical properties of murine hippocampal subregions investigated by atomic force microscopy and in vivo magnetic resonance elastography," *Scientific Reports*, vol. 12, no. 1, 2022, ISSN: 2045-2322. DOI: 10.1038/s41598-022-21105-7.

[212] K. Han *et al.*, "A survey on vision transformer," *IEEE Transactions on Pattern Analysis and Machine Intelligence*, vol. 45, no. 1, pp. 87–110, 2023, ISSN: 1939-3539. DOI: 10.1109/TPAMI.2022.3152247.

[213] Z. Wang and L. Wu, "Theoretical analysis of the inductive biases in deep convolutional networks," *Advances in Neural Information Processing Systems*, vol. 36, 2024.

[214] D. P. Kingma and J. Ba, "Adam: a method for stochastic optimization," *CoRR*, vol. abs/1412.6980, 2014.

[215] A. Géron, *Hands-on machine learning with Scikit-Learn, Keras, and TensorFlow*. " O'Reilly Media, Inc.", 2022, ISBN: 1098122461.

[216] P. Li, S. Ni, L. Zhang, S. Zeng, and Q. Luo, "Imaging cerebral blood flow through the intact rat skull with temporal laser speckle imaging," *Optics Letters*, vol. 31, no. 12, pp. 1824–1826, 2006. DOI: 10.1364/OL.31.001824. [Online]. Available: https://opg.optica.org/ol/abstract.cfm?URI=ol-31-12-1824.

[217] F. Winkler *et al.*, "Kinetics of vascular normalization by vegfr2 blockade governs brain tumor response to radiation," *Cancer Cell*, vol. 6, no. 6, pp. 553–563, 2004, ISSN: 1535-6108. DOI: 10.1016/j.ccr.2004.10.011.

[218] C. Xu, "Optical clearing of the mouse skull," *Light: Science & Applications*, vol. 11, no. 1, 2022, ISSN: 2047-7538. DOI: 10.1038/s41377-022-00989-0.

[219] M. Panniello, S. A. C. Limal, and M. M. Kohl, "Imaging somatosensory cortex in rodents," in *Neuromethods*. Springer US, 2023, pp. 373–396, ISBN: 0893-2336. DOI: 10.1007/978-1-0716-3068-6_17.

[220] S. J. Derby *et al.*, "Inhibition of atr opposes glioblastoma invasion through disruption of cytoskeletal networks and integrin internalization via macropinocytosis," *Neuro-Oncology*, vol. 26, no. 4, pp. 625–639, 2024, ISSN: 1522-8517. DOI: 10.1093/neuonc/noad210.

[221] Z. Ou *et al.*, "Achieving optical transparency in live animals with absorbing molecules," *Science*, vol. 385, no. 6713, eadm6869, 2024. DOI: doi:10.1126/science.adm6869. [Online]. Available: https://www.science.org/doi/abs/10.1126/science.adm6869.